

Attosecond Metrology
and
Application of High Harmonics

Jann Eike Kruse

December 22, 2010

Submitted as doctoral thesis to the
Faculty of Physics of the University of Crete.

Supervisor

Καθ. Δημήτρης Χαραλαμπίδης
(Prof. Dimitris Charalambidis)

Adviser

Δρ. Πάρης Τζάλλας
(Dr. Paris Tzallas)

List of publications in the course of this thesis

1. Álvaro Peralta Conde, Jann Eike Kruse, Olivier Faucher, Paris Tzallas, Emmanouil P. Benis, and Dimitris Charalambidis. “Realization of time-resolved two-vacuum-ultraviolet-photon ionization.” *Physical Review A* **79**,6 061405 (2009)
2. Olivier Faucher, Paris Tzallas, Emmanouil P. Benis, Jann Eike Kruse, Álvaro Peralta Conde, Costas Kalpouzos, and Dimitris Charalambidis. “Four-dimensional investigation of the 2nd order volume autocorrelation technique.” *Applied Physics B* **97**,2 505–510 (2009)
3. Emmanouil Skantzakis, Paris Tzallas, Jann Eike Kruse, Costas Kalpouzos, and Dimitris Charalambidis. “Coherent continuum extreme ultraviolet radiation in the sub-100-nJ range generated by a high-power many-cycle laser field.” *Optics Letters* **34**,11 1732–1734 (2009)
4. Emmanouil Skantzakis, Paris Tzallas, Jann Eike Kruse, Costas Kalpouzos, Olivier Faucher, George D. Tsakiris, and Dimitris Charalambidis. “Tracking Autoionizing-Wave-Packet Dynamics at the 1-fs Temporal Scale.” *Physical Review Letters* **105**,4 043902 (2010)
5. Paris Tzallas, Emmanouil Skantzakis, Jann Eike Kruse, and Dimitris Charalambidis. “On the generation of intense isolated attosecond pulses by many-cycle laser fields.” in *Progress in Ultrafast Intense Laser Science VII*, volume 100 of *Springer Series in Chemical Physics*, (in press)
6. Jann Eike Kruse, Paris Tzallas, Emmanouil Skantzakis, Costas Kalpouzos, George D. Tsakiris, and Dimitris Charalambidis. “Inconsistencies between two attosecond pulse metrology methods: A comparative study.” *Physical Review A* **82**,2 021402 (2010)
7. Jann Eike Kruse, Paris Tzallas, Emmanouil Skantzakis, and Dimitris Charalambidis. “Persistent quantum interfering electron trajectories.” *Physical Review A* **82**,3 033438 (2010)

Abstract

Real-time studies of ultra-fast evolving quantum systems require even faster probe mechanisms. For electronic systems on the atomic scale sub-femtosecond laser pulses are suitable. High-order harmonic generation can produce the necessary broad spectrum to support such short pulses. Under certain phase-matching conditions a subset of the emitted radiation can be well phase-locked resulting in attosecond laser pulses. To extract sound information from the experiments' results, accurate and reliable temporal and structural assessment of these pulses is indispensable. Various attosecond metrology methods have been proposed and some applied. Most of these rely either on a two-color photo-ionization of an atomic system by both the extreme-ultraviolet attosecond pulses and the fundamental infrared radiation together or they rely on a second-order autocorrelation based on a two-photon ionization by the mere attosecond pulses alone.

Two techniques underlying most of the attosecond metrology methods were compared and evaluated. These are the *reconstruction of attosecond beating by interference of two-photon transitions* (RABITT) and the *second-order intensity volume-autocorrelation* (2IVAC). Despite considerable controversy on the applicability and reliability of these two methods, a direct comparison between them has been missing. This thesis fills that gap and examines the strengths and limitations of these and other metrology methods based on them. In this context a dispersionless second-order autocorrelator was set up and tested by measuring the interferometric autocorrelation of the 1.87PHz fifth harmonic pulse. Both metrology methods were applied and compared leading to the conclusion, that RABITT may underestimate the pulse duration. The participation of different quantum-paths to the high harmonic generation process in gases, shown here for several phase-matching conditions, has ramifications on applying cross-correlation methods for attosecond metrology as well as on atomic-molecular tomography and precision measurements with extreme ultraviolet (XUV) frequency combs. Additionally, studying the photo-dissociation dynamics of ethylene and oxygen, utilizing the same apparatus as used for the metrology, revealed their decay times of a few femtoseconds.

Contents

Abstract	1
Contents	3
List of Figures	5
List of Symbols	7
Preface	12
1 Overview	13
1.1 Generation of broad-bandwidth radiation	13
1.1.1 High harmonic generation in gases	14
1.1.2 High harmonic generation from surfaces	16
1.2 Synthesis of attosecond pulses	19
1.3 Characterization methods of attosecond pulses	23
2 Experimental setup	35
2.1 Ti:sapphire laser system	35
2.2 Generation of harmonic radiation	36
2.2.1 Glass target	36
2.2.2 Xenon gas jet	39
2.3 Characterization and application system	41
2.3.1 Wave front splitting device	43
2.3.2 Time-of-flight spectrometer	48
3 Results	51
3.1 Comparison of attosecond metrology methods	52
3.1.1 Second-order intensity volume-autocorrelation	53
3.1.2 Reconstruction of attosecond beating by interference of two-photon transitions	56
3.2 Quantum-interfering electron trajectories	64
3.3 Molecular dissociation dynamics	70
3.3.1 Ethylene	72
3.3.2 Oxygen	75
4 Conclusions	77
4.1 Summary	77
4.2 Outlook	80

A Appendix	83
A.1 Technical details	83
A.1.1 Control and data acquisition software	83
A.1.2 Electronics	84
A.1.3 Piezoelectric pulsed gas-jet valves	84
A.2 Acknowledgments	89
A.2.1 Marie Curie Fellowship	89
A.2.2 Special thanks	89
A.3 Glossary	93
A.4 Index	97
A.5 Bibliography	99

List of Figures

1.1	Calculated spectrum from HHGG	15
1.2	Phases of the harmonics from HHGG	21
1.3	Transition diagram for RABITT	27
1.4	Transition diagram for a second-order volume-autocorrelation . . .	31
1.5	Electric field at the focus of a split mirror	32
2.1	Setup for harmonic generation from surfaces	37
2.2	Spectrum from surface plasma	38
2.3	Intensity trace of the driving laser	39
2.4	Setup for harmonic generation in gas targets	40
2.5	Diameter of the harmonic radiation	41
2.6	Harmonic generation at different focus positions	42
2.7	Schematic of the characterization and application system	43
2.8	Simulation of the 2nd-order volume-autocorrelation	45
2.9	High-order autocorrelation of the infrared	46
2.10	Interferometric autocorrelation of the fifth harmonic	47
2.11	Time-of-flight spectra	49
3.1	Setup for attosecond metrology	52
3.2	Helium ion-mass spectrum	54
3.3	Measured 2IVAC traces	55
3.4	Measured time-of-flight photoelectron spectra with <i>side bands</i> . . .	57
3.5	Measured RABITT traces and reconstructed pulses	58
3.6	Phases measured with RABITT	59
3.7	Calculated RABITT traces	61
3.8	Comparing a RABITT reconstruction to an averaged pulse train . .	63
3.9	Setup for measuring quantum-interfering electron trajectories . . .	64
3.10	Calculated phase difference between the two electron trajectories .	65
3.11	Interference between the two electron trajectories	66
3.12	XUV \pm IR interference between the two electron trajectories	67
3.13	Calculated <i>side band</i> signal in dependence on the laser intensity .	69
3.14	Setup to study molecular dynamics	70
3.15	Ethylene molecular structure and photo-reaction path	72
3.16	TOF ion signals of krypton, ethylene and its fragments	74

3.17 TOF ion signals of krypton and oxygen	75
A.1 Control and data acquisition program code and user interface . .	85
A.2 High-voltage switch and valve driver electronic circuits	86
A.3 Piezoelectric pulsed gas-jet valve	87

List of Symbols

γ_q	Photon of the q^{th} harmonic, page 28
$\Delta\nu$	Spacing between two consecutive harmonics, page 16
$\Delta\nu_P$	Spectral bandwidth of an electromagnetic pulse, page 13
Δt	Temporal delay of one light pulse with respect to another, page 29
Θ_L	Total angular spread of the laser beam, page 15
Θ_q	Total angular spread of the q^{th} harmonic, page 15
η	Efficiency of conversion of fundamental radiation into high harmonics, page 16
ν_{co}	Frequency of the <i>cut-off</i> (i.e. end of the <i>plateau</i>) where the intensities of the higher harmonics drop rapidly, page 15
ν_L	Frequency of the laser, page 14
ν_q	Frequency of the q^{th} harmonic, page 14
τ_L	Duration of the infrared laser pulse, page 9
τ_{FTL}	Fourier-transform limited minimum pulse duration of an electromagnetic pulses supported by a given spectrum, page 19
τ_ℓ	Traveling time of the <i>long</i> trajectory, page 20
τ_P	Pulse duration, page 13
τ_q	Duration of the emission of the q^{th} harmonic, page 15

τ_s	Traveling time of the <i>short</i> trajectory, page 20
ϕ_q	Phase of the q^{th} harmonic relative to the phase ϕ_L of the laser, page 19
φ_{q+1}	Phase of the oscillation of the <i>side band</i> from harmonics q and $q + 2$, page 28
ϕ_q^ℓ	Phase of the q^{th} harmonic produced by the <i>long</i> trajectory, page 20
ϕ_q^s	Phase of the q^{th} harmonic produced by the <i>short</i> trajectory, page 20
\mathcal{E}	Electric field, page 19
E^γ	Photon energy, page 72
E_L	Energy of the driving laser pulse, page 39
f	Focal length of an optical element, page 32
I_L^{max}	Laser intensity at which the conversion into high harmonics is maximum, page 16
P_{HHGG}	Pressure in the HHGG vacuum chamber, page 39
q	Ordinal number of the spectral component of the harmonic radiation, page 14
\mathcal{S}	Quasi-classical action, page 20
S	Measured signal, page 25
t_e	Time of recollision of the quasi-free electron with the parent ion and emission of the harmonic radiation, page 15
T_L	Period of the laser, page 16
t_r	Time of recollision/return of the quasi-free electron with/to the parent ion and emission of the harmonic radiation (see t_e), page 15
t_t	Time of tunneling separation of the quasi-free electron from the parent ion, page 15
w_0	Diameter of the beam waist of a Gaussian beam, page 44
z_A	Position of the focus when focusing after the production gas, page 42
z_B	Position of the focus when focusing before the production gas, page 42

-
- z_f Position of the focus relative to the xenon jet, page 41
- z_I Position of the focus when focusing inside the production gas, page 42

Preface

Producing strong light pulses of short duration has been an indispensable tool for many technical and scientific disciplines for centuries, including not only photography, stroboscopy, chemistry, medicine and physics. Shortening the duration and increasing the intensity opens the doors to new applications in many disciplines like fluorescence or optical-gating spectroscopy and microscopy, as well as time-resolved measurements of molecular and electronic dynamics down to the atomic or sub-atomic scale. Many of these applications require coherent light. The shortest coherent light sources commercially available from Ti:sapphire laser systems have a pulse duration of $\tau_L \approx 5$ fs, which corresponds to only about two optical cycles. In the case of infrared or visible light, the pulses can not be much shorter than that. In order to shorten the pulses it is necessary to extend the electromagnetic spectrum to the ultraviolet (UV) or even x-ray. This can be achieved¹ utilizing high harmonic generation in gases (HHGG) from an intense coherent light source. Specific experimental conditions² have proven to provide the phase-locking of the emitted harmonics necessary to form attosecond pulses. High harmonic generation from surfaces³ (HHGS) was also successfully shown⁴ to be a viable alternative for attosecond pulse generation.

Since the proposals⁵ to generate attosecond pulses more than eighteen years ago, *attoscience* has left its infant cradle and matured to become a full grown field of science. These attosecond light pulses produced⁶ today have already found a number of interesting applications in all states of matter.

¹Farkas and Tóth (1992)

²Antoine *et al.* (1996); Gaarde and Schafer (2002)

³Rykovanov *et al.* (2008)

⁴Nomura *et al.* (2009)

⁵Hänsch (1990); Farkas and Tóth (1992)

⁶Tzallas *et al.* (2003); Kienberger *et al.* (2004)

They could be used to directly measure femtosecond light fields,⁷ to track the dynamics of autoionizing wave packets,⁸ to observe electron tunneling in atoms,⁹ and for attosecond spectroscopy¹⁰ revealing sub-femtosecond timing characteristics of photoelectron emission.

An ever growing number of scientific groups around the world is setting up or expanding their laboratories in order to generate, study, and apply attosecond laser pulses. The substantial discourse on the generation and characterization of attosecond pulses has led to a number of publications,¹¹ which could either not be verified or came to erroneous conclusions, and the precise and reliable characterization of the produced ultra-short broad-spectrum pulses is still one of the major difficulties, that *attoscience* faces. For this purpose various metrology methods have been applied and others envisioned. Most of these derive either from an autocorrelation (AC) of the attosecond pulses only, or they derive from a cross-correlation of the fundamental infrared (IR) laser with the attosecond extreme ultraviolet (XUV) radiation generated by HHGG.

Two techniques, which most metrology methods are based on, are assessed in the course of this thesis. Despite considerable dissent on their capabilities and the limitations of their applicability, there had so far been no direct comparison between these two methods. Here both methods are applied, compared and analyzed concluding that *reconstruction of attosecond beating by interference of two-photon transitions* (RABITT) may result in an underestimation of the reconstructed pulse duration, due to the fact that it measures average phases. For these measurements a dispersionless XUV autocorrelator, utilizing helium photo-ionization as non-linear process, was set up. The attosecond precision was tested by measuring the interferometric AC of the fifth harmonic generated in xenon by a Ti:sapphire IR laser.

Further, the investigation of the two most dominant quantum-paths,

⁷Goulielmakis *et al.* (2004)

⁸Skantzakis *et al.* (2010)

⁹Uiberacker *et al.* (2007)

¹⁰Cavalieri *et al.* (2007)

¹¹Papadogiannis *et al.* (1999); Drescher *et al.* (2001); Paul *et al.* (2001); Hentschel *et al.* (2001)

which lead to the HHGG process, called the *long* and the *short* electron trajectory, showed that both contribute to the emission of the XUV frequency comb at all three phase matching conditions applied. This has substantial impact on the cross-correlation-based metrology methods and on atomic-molecular tomography and precision measurements applying such XUV frequency combs.

Finally, an example is presented using the ultra-short coherent light pulses generated with HHGG for time-resolved studies of the molecular dynamics in the photo-dissociation process of ethylene and oxygen. All the characteristic times in the femtosecond scale of the evolution of the excited ethylene molecule could be extracted from the measured ionic products utilizing the same apparatus applied for the XUV AC measurements.

Chapter 1 gives a short review on what has been achieved so far in the field of attosecond generation and characterization. Techniques to generate attosecond pulses from a superposition of high harmonics are explained and their differences examined. Different metrology methods are introduced, most of them based on autocorrelation and cross-correlation concepts. The two techniques, which most methods are based on are explained in more detail. This is firstly the *second-order intensity volume-autocorrelation*¹² (2IVAC), which can determine to a good degree of accuracy the duration of the attosecond pulses but requires high intensities of the XUV radiation to be examined and secondly the *reconstruction of attosecond beating by interference of two-photon transitions*¹³ (RABITT), which relies on a cross-correlation of the attosecond pulse train with the driving laser that generated the harmonic radiation. The latter requires less intense attosecond pulses and could theoretically reveal the temporal structure of the individual pulses in the pulse train.

Chapter 2 describes the experimental setup for the generation of high harmonic radiation in gas media and from surfaces. Also the arrangements for the autocorrelation and cross-correlation measurements are explained there

¹²Tzallas *et al.* (2003); Faucher *et al.* (2009)

¹³Paul *et al.* (2001); Muller (2002)

as well as the time-of-flight spectrometer used for the detection of the ions and the electrons used in all of the following experiments.

In Chapter 3 the results are analyzed and discussed. Most interestingly the comparison between the results from the two metrology methods is presented there. But also a study of the interference between different quantum paths relevant to high harmonic generation (HHG) in gas media shows the pitfalls, that attosecond metrology methods have to circumvent. Using the same apparatus, a time-resolved ion-mass spectroscopy reveals the characteristic times involved in the dynamics of molecular oxygen and ethylene excited by an ultra-short vacuum ultraviolet (VUV) laser pulse.

Finally Chapter 4 concludes by summarizing and reviewing the experimental and theoretical findings and discussing their impact on *attoscience* and other fields of study. It also gives an outlook toward which direction to go with future investigations.

Chapter 1

Overview

To get familiar with the basic techniques used in *attoscience*, this chapter gives a short review on the state of the art of attosecond light pulse generation and characterization. Ways to provide the spectral bandwidth necessary for attosecond pulses are introduced first in Section 1.1, with focus on the two methods to produce high-order harmonic radiation, either from noble gases or from surface plasma. The next Section 1.2 shows how the phase relations of the harmonics determine, if the emitted radiation forms bursts of attosecond duration. Section 1.3 on characterization informs about the wide range of attosecond metrology methods both proposed and already applied. Also the two methods underlying most of these techniques, which will both be analyzed thoroughly in Chapter 3, are introduced here.

1.1 Generation of broad-bandwidth radiation

Heisenberg's uncertainty principle of quantum mechanics is also reflected in a basic principle of wave mechanics: The generation of a very short electromagnetic pulse with duration τ_P requires a very broad spectral bandwidth $\Delta\nu_P$.

$$\tau_P \cdot \Delta\nu_P \geq C \gtrsim 1 \quad (C \text{ is constant}) \quad (1.1)$$

The minimum pulse duration $\tau_P^{\min} \approx 1/\Delta\nu_P$ can only be reduced, if the spectral bandwidth $\Delta\nu_P$ increases, so that the product $\tau_P \cdot \Delta\nu_P$ stays larger than the critical constant C , which is greater or similar to one, depending on the exact pulse shape and the exact definitions of the pulse duration and bandwidth. Although a bandwidth of $\Delta\nu_L \approx 50$ THz, measuring the full width over half the maximum (FWHM), distributed in a Gaussian around the central laser frequency of $\nu_L \approx 375$ THz, is sufficient for infrared Gaussian laser pulses of $\tau_L \approx 50$ fs duration (measuring FWHM of the intensity), the generation of attosecond pulses with orders of magnitude shorter pulse duration requires a much broader spectrum.

It is known for more than 20 years now, that high harmonic generation (HHG) can provide a broad frequency comb of equally spaced emission lines.¹ For an extended region of the spectrum, the emitted frequency components have similar intensities. This region is called the *plateau* and it is followed by a *cut-off*, after which the intensities of the next higher frequency components drop much more rapidly. The recent advances in table-top laser systems have made it possible, that the long known method of high harmonic generation in gases (HHGG) may soon be superseded by the high harmonic generation from surfaces (HHGS), which proved to have a number of significant advantages over the former. Both are discussed in the following sections.

1.1.1 High harmonic generation in gases

A common way to produce harmonics of higher orders is to focus ultra-short high-intensity laser pulses inside an noble gas, which is usually either confined in a gas cell separated from the surrounding vacuum by differential pumping, or the gas is directly ejected into the vacuum chamber as a jet by a pulsed nozzle. This way exclusively odd harmonics are produced with frequencies $\nu_q = q \nu_L$ that are odd multiples $q \in \{3, 5, 7, \dots\}$ of the fundamental laser frequency ν_L . Figure 1.1 shows a calculated emission spectrum from HHGG using a $\tau_L = 40$ fs laser pulse with $\lambda_L = 800$ nm wavelength. The *plateau* region in that spectrum ends with the 41st harmonic at the *cut-off* frequency of

¹McPherson *et al.* (1987); Ferray *et al.* (1988)

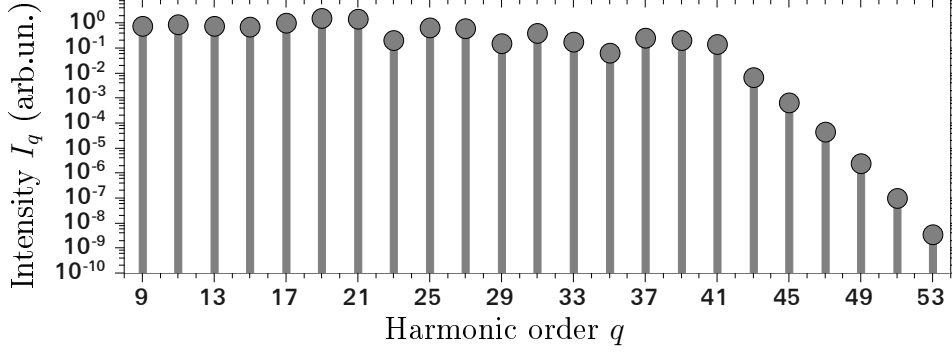


Figure 1.1: Calculated spectrum from high harmonic generation in gases

The graph shows calculated intensities I_q of harmonics produced in a gas medium using a $\tau_L = 40$ fs laser pulse with $\lambda_L = 800$ nm wavelength at an intensity of $I_L = 2.5 \times 10^{14}$ W/cm² according to the model described by Lewenstein *et al.* (1994).

$\nu_{co} \approx 15.4$ PHz. The harmonics are emitted in the direction of the driving laser beam with a total angular spread smaller than that of the initial beam: $\Theta_q \approx \frac{1}{\sqrt{p}}\Theta_L$. The parameter p depends on the order of non-linearity and is about $4 \lesssim p \lesssim 7$ for the harmonics in the *plateau*. Also the temporal profile of the emitted harmonics does not exactly follow that of the driving laser. As shown in Sections 2.3.1 and 3.3.2 the duration τ_q of the emission of a harmonic q is considerably shorter² than the duration of the driving laser pulse: $\tau_q \approx \frac{1}{\sqrt{p}}\tau_L$

The *three-step model*³ describes the basic underlying mechanism semi-classically: In the first step at time t_t the laser field causes the electron to tunnel away from the atom, in the second step it acquires kinetic energy from the electromagnetic field, and eventually in the third step, after the direction of the electric field has changed, the electron recollides with the parent ion at time t_e resulting in the emission of the gained energy E^γ as a burst of radiation. The photon energy is less than $E^\gamma \lesssim E_I + 3.2E_p$ for the harmonics in the *plateau* region. E_I and E_p are the ionization energy of the parent atom and ponderomotive energy of the driving laser, respectively. This process happens twice per laser period T_L , once per each maximum of the laser's

²Protopapas *et al.* (1997) pages 434–435; Agostini and DiMauro (2004) pages 826–827

³Kulander *et al.* (1993); Corkum (1993); Schafer *et al.* (1993)

electric field, if the laser has linear or almost linear polarization. The principles of Fourier analysis postulate, that any series of radiation bursts, which is periodic with the laser's optical half cycle $\frac{T_L}{2}$, consists of frequencies spaced apart by twice the laser frequency $\Delta\nu = \frac{2}{T_L} = 2\nu_L$. Due to the linear polarization of the laser and the symmetry of the gas atoms, which lead to the symmetry of the emitted bursts, the harmonic orders are odd multiples.

The emission of harmonics with photon energy $E^\gamma < E_I$ less than the ionization energy of the gas atoms can apparently not be described by the *three-step model*. This process can be understood in terms of lowest-order perturbation theory. Thus their yield drops exponentially with harmonic order.

The efficiency $\eta = \frac{E_{XUV}}{E_L}$ of conversion from fundamental laser radiation into extreme ultraviolet (XUV) harmonic radiation is rather low. Using a loose focusing and a xenon gas jet, a conversion efficiency of $\eta \approx 10^{-5}$ has been reported⁴ resulting in $E_{XUV} \approx 1 \mu\text{J}$ for the energy of the harmonics from a driving laser with $E_L = 100 \text{ mJ}$. But after the ionization saturation limit I_L^{max} is reached, the generation of XUV radiation saturates. For HHGG in xenon by an infrared laser pulse with $\tau_L = 50 \text{ fs}$ the saturation intensity is approximately $I_L^{\text{max}} \approx 8 \times 10^{13} \text{ W/cm}^2$. Further increasing the laser intensity eventually reduces the harmonic yield due to the ionization of the gas medium, which causes a break-down of the phase-matching. In order to increase the number of photons per harmonic, a work-around for this problem is to keep the driving laser intensity I_L constant and to increase the laser power together with the spot size by using an even longer focal length. This on the other hand can place severe technical challenges to the optical setup and the vacuum system.

1.1.2 High harmonic generation from surfaces

Another promising technique to generate harmonic radiation, and consequently attosecond pulses, is the high harmonic generation from surfaces.

⁴Takahashi *et al.* (2002); Hergott *et al.* (2002)

It has been experimentally observed⁵ for the first time in 1977. Two qualitatively very different models seek to describe the generation process:

Relativistic oscillating mirror (ROM) One approach is to understand the plasma, which the driving laser generates on the surface of the target, as a reflecting mirror⁶ that oscillates with the driving laser field and reaches velocities close to the speed of light c . The relativistic Doppler effect then gives rise to the emission of higher frequencies. Since the speed of the electrons that constitute the plasma is relativistic, the dipole approximation is no longer valid. Their movement as seen from the observer deviates from the sinusoidal form but remains periodic with T_L . So the Fourier-series expansion of the electrons' movement in the observer's inertial frame of reference shows components with additional frequencies $\nu_q = q \nu_L$. This results in emission of harmonic radiation of the orders $q \in \{2, 3, 4, \dots\}$. The intensities I_q of the emitted harmonics q follow a power law for frequencies ν_q below the *cut-off* and drop exponentially for higher frequencies. The model has later been analytically refined and compared with particle-in-cell simulations,⁷ which predict a power law with $I_q \propto q^{-8/3}$ for monochromatic irradiation and a different *cut-off* frequency ν_{co} compared to the plain relativistic oscillating mirror (ROM) model.

Coherent wake emission (CWE) Another model describes the harmonic emission as a consequence of a wake⁸ in the plasma on the target's surface. Electrons leave the plasma, accelerate in the laser field and reenter back into the surface, in a way somewhat similar as in the *3-step model* for gas harmonics. As the electrons periodically sweep through the plasma, they give rise to a series of wakes, which emit radiation with frequencies that are harmonics of the driving laser. The electrons must be accelerated perpendicular to the target's surface and therefore no s-polarized light causes a coherent wake emission (CWE). The highest frequency ν_{co} produced by this method

⁵Burnett *et al.* (1977); Carman *et al.* (1981)

⁶Plaja *et al.* (1998)

⁷Baeva *et al.* (2006)

⁸Teubner *et al.* (2004); Quéré *et al.* (2006)

is the electron plasma frequency ν_p of the bulk target material.⁹ This is lower than the ν_{co} reachable with the ROM.

Which model describes the interaction better depends on the intensity and the wavelength of the driving laser field. For infrared (IR) lasers at moderate intensities of $I_L \lesssim 1.4 \times 10^{18} \frac{\text{W/cm}^2}{\lambda_L^2/\mu\text{m}^2}$ the ROM does not play a significant role and the CWE model alone can describe the emission. For higher IR laser intensities the ROM comes into play and eventually dominates the emission process. The CWE process can be efficient even down to laser intensities of $I_L \gtrsim 4 \times 10^{15} \frac{\text{W/cm}^2}{\lambda_L^2/\mu\text{m}^2}$.

The HHG from solids has some important qualitative differences compared to the HHG in gas media:

The spectrum When generating harmonics from surfaces, both odd and also even harmonics are emitted, because the process is periodic with the optical cycle of the driving laser.

The conversion efficiency Compared to the generation of harmonics from gas media, the efficiency of ROM harmonics can be orders of magnitude higher. The conversion of radiation from a laser with $\lambda_L = 1055 \text{ nm}$ into harmonics with photon energies of $E_\gamma > 20 \text{ eV}$ with an efficiency of $\eta \approx 10^{-2}$ has been reported.¹⁰

The incident intensity When generating harmonics in gas media, the ionization of the target medium is an important limiting factor for the driving laser intensity and thus limiting the energy output of harmonic radiation. This is not a problem for harmonics generated from surfaces. For HHGS the incident intensity can be orders of magnitude higher than for HHGG.

Both of the above mechanisms for HHGS rely on a clean plasma surface on the target and a steep plasma density gradient for the interaction. A prepulse or pedestal of $I_{pre} \gtrsim 10^{12} \text{ W/cm}^2$ at a time earlier than $t \lesssim -1 \text{ ps}$ before the

⁹Tarasevitch *et al.* (2007)

¹⁰Dromey *et al.* (2007)

main pulse, creates a plasma on the target's surface which expands enough to diminish the harmonic emission process by more than 99%.¹¹

1.2 Synthesis of attosecond pulses

The idea of generating attosecond pulses from the high-order harmonics¹² generated as described above, comes from the principle of Fourier synthesis:

$$f(x) = \sum_{n=-\infty}^{\infty} c_n e^{inx} \quad (c_n \in \mathbb{C}) \quad (1.2)$$

The infinite Fourier series $f(x)$ of equally spaced phase-locked frequencies n converges to an infinite series of Dirac δ pulses in the time domain. Correspondingly, the electric field \mathcal{E} resulting from the superposition of a set Q of quasi phase-locked harmonics q with circular frequencies $\omega_q = q\omega_L$ forms a train of attosecond pulses.

$$\mathcal{E}(t) \propto \sum_{q \in Q} A_q \cos(\omega_q t - \phi_q) \quad (1.3)$$

When using the set Q of harmonics with their relative amplitudes A_q then the minimal achievable duration τ_{FTL} of the pulses in the train is called the Fourier-transform limit (FTL). This theoretically ideal case could only be reached, if the phases of the harmonics ϕ_q were locked perfectly:

$$\tau_{\text{XUV}} = \tau_{\text{FTL}} \quad \Leftrightarrow \quad \phi_q = aq + b \quad (a, b \in \mathbb{R}) \quad (1.4)$$

High harmonic generation in gases The phases ϕ_q of the harmonics are different for each harmonic q due to the response of the atoms to the IR driving laser. They can be inferred from the quantum mechanical description of the interaction, using a single-active-electron strong-field approximation and the saddle-point-solution method to find the stationary action in the

¹¹Tarasevitch *et al.* (2000)

¹²Farkas and Tóth (1992)

spirit of Feynman's path integral formalism.¹³ The theoretical models predict a fundamental intrinsic characteristic of the HHG in gases: For any point in the spectrum of the emitted radiation, there exist two relevant trajectories of the quasi-free electron, which both lead to the same recollision energy and therefore to the same emitted frequency ν . The two electron trajectories are called *long* and *short* according to the different traveling times τ_ℓ and τ_s during which the electron is separated from the parent ion. As a consequence, there are two sets of phases of the emitted harmonics: ϕ_q^s for the *short* and ϕ_q^ℓ for the *long* trajectory.

For each of these two trajectories the phase of the emitted harmonic q is proportional to the action \mathcal{S} that the electron acquires during the interaction. The total action can be separated into the three components corresponding to the steps of the *three-step model*: $\mathcal{S} = \mathcal{S}_1 + \mathcal{S}_2 + \mathcal{S}_3$. The first and the third part depend on the binding potential E_0 of the electron and the third part also on the emitted photon energy $\hbar\omega_q$. The second part \mathcal{S}_2 of the action, accumulated by the quasi-free electron wave-packet during its excursion into the continuum while it is separated from the parent ion, can be approximated by the product of the traveling time $\tau = t_e - t_t$ multiplied with the ponderomotive energy E_p of the driving laser field.

$$\begin{aligned} \text{Step 1: tunneling separation:} & \quad \mathcal{S}_1 = -E_0 t_t \\ \text{Step 2: quasi-free wave packet:} & \quad \mathcal{S}_2 \approx -E_p \tau \\ \text{Step 3: recombination and emission:} & \quad \mathcal{S}_3 = (E_0 + \hbar\omega_q) t_e \end{aligned} \tag{1.5}$$

$$\Rightarrow \text{ total action: } \mathcal{S} \approx E_0 \tau - E_p \tau + \hbar\omega_q t_e$$

Since the ponderomotive energy $E_p = \frac{A}{\omega_q^2} I_L(t, r, z)$ is proportional to the laser intensity, which itself varies with time t , with distance from the focus r , and along the focus z , the emission at different position and time has a different phase. This leads to a situation, where favorable phase-matching conditions must be chosen to ensure effective harmonic emission. Harmonics emitted at different time t during the driving pulse at different laser intensity I_L have

¹³Lewenstein *et al.* (1994); Salières *et al.* (2001)

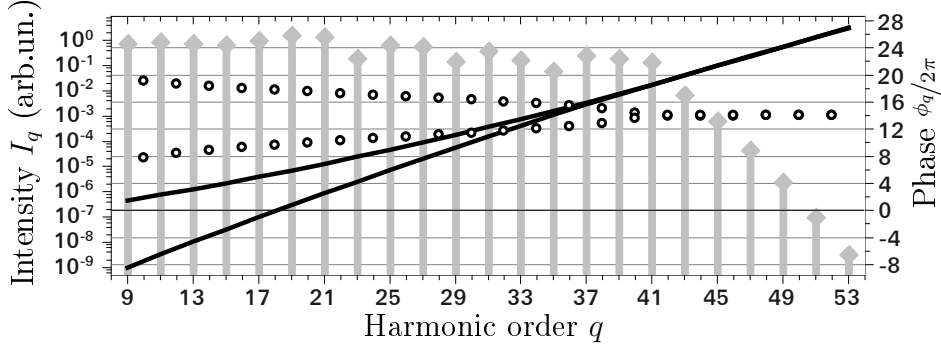


Figure 1.2: Phases of the harmonics generated in gas media

The solid lines are the phases ϕ_q^s of the harmonics emitted from electrons traveling along the *short* trajectory and the phases ϕ_q^ℓ from electrons traveling along the *long* trajectory, calculated according to the quantum mechanical model for a driving laser pulse with $\tau_L = 40$ fs duration, $\lambda_L = 800$ nm wavelength, and an intensity of $I_L = 2.5 \times 10^{14}$ W/cm². The vertical gray bars in the background depict the calculated intensity spectrum I_q . The circles between the odd harmonics show the phase difference $\Delta\phi_{q+1} = \phi_{q+2} - \phi_q \propto t_e$ between the two neighboring harmonics. The phases are in units of full cycles (2π rad). The phase differences are scaled by a factor 10.

a different phase $\phi_q(t)$, which leads to the harmonic chirp¹⁴ $\frac{\partial}{\partial t}\omega = \ddot{\phi}$. Since the *long* electron trajectory has a larger traveling time τ_ℓ , Equation 1.5 shows that its phase $\phi_q^\ell(t)$ is more sensitive to the variations \dot{I}_L of the laser intensity and emission from that trajectory may bear a larger chirp. The consequence of this harmonic chirp is that the pulses inside the attosecond pulse train are not equidistant throughout the entire train. This has important implications on the metrology methods discussed later.

The degree of phase-locking of a sequence Q of odd harmonics and thus the degree of light bunching into attosecond pulses with high contrast and short duration is reduced by the "inter-harmonic chirp"¹⁵ $\Delta^2\phi_q = (\phi_{q+2} - \phi_q) - (\phi_q - \phi_{q-2})$. Figure 1.2 shows the calculated phases for different harmonics produced by HHGG, from electrons following either the *short* or the *long* trajectory, according to the saddle-point-solution method. The graphs of ϕ_q^s and ϕ_q^ℓ show, that the harmonics are initially not phase-locked, since

¹⁴Varjú *et al.* (2005)

¹⁵Kazamias and Balcou (2004)

the phases are not a purely linear function of the harmonic order q . The non-linear component causes the *inter-harmonic chirp* which broadens the pulses in the train. The circles in the Figure 1.2 show the phase differences $\Delta\phi_{q+1} = \phi_{q+2} - \phi_q$ between two consecutive harmonics, which are proportional to the emission times t_e . Since the emission time changes with harmonic order q a phase-mismatch between the emitted harmonics occurs. For the *plateau* harmonics the phase difference can be approximated by a line which corresponds to a constant *inter-harmonic chirp* in that spectral region. In order for the emitted harmonics to be well phase-locked, that *inter-harmonic chirp* must be compensated for.

On the macroscopic scale numerous effects complicate the situation: The dispersion due to the propagation in the partially ionized gas medium, the geometrical Gouy phase shift along the focus, and the variation of the laser intensity along the focus in the interaction volume (temporal chirp) as well as the intensity distribution across the focal spot (spatial chirp) must be taken into account. To achieve optimal phase-matching in the gas medium, the condition for the wavevectors of the harmonics (k_q) and the driving laser (k_L) as well as the mismatch caused by the dispersion (Δk_d), the Gouy-phase shift (Δk_G), and the intensity-dependent harmonic phase ($\vec{\nabla}\phi_q$) is:

$$k_q - q \cdot k_L = \Delta k_G + \Delta k_d + \vec{\nabla}\phi_q \quad (1.6)$$

Fortunately, some of these effects can partially compensate for each other and according to theory,¹⁶ focusing the laser beam almost a Rayleigh range z_R before the generation gas provides for "good" phase-matching conditions for the *short* trajectory and phase-locking between the harmonics to a degree of more than 50%. This applies to a pulse with a Gaussian intensity distribution both in time and in cross-section.

Due to the longer flight time τ_ℓ of the *long* trajectory, the phases ϕ_q^ℓ of the harmonics emitted from electrons following that trajectory are more sensitive to variations of the laser intensity as can be understood from Equation 1.5. Thus the *inter-harmonic chirp* of the *long* trajectory emission can not be

¹⁶Antoine *et al.* (1996); Gaarde and Schafer (2002)

compensated for in such a way and emission from that trajectory can not be phase-locked, so emission from that trajectory must be suppressed for the generation of attosecond pulses.

High harmonic generation from surfaces The harmonics from solid targets follow a different phase relation depending on the underlying mechanism responsible for their generation. The ROM model, which applies if the incident intensity exceeds the critical value to reach the relativistic regime, predicts that the phases of the harmonics are almost perfectly phase-locked.¹⁷

This becomes apparent in the picture of the relativistic γ -spikes,¹⁸ which occur at very confined moments when the speed of the plasma surface reaches values close to the speed of light. During these short times the highest harmonic orders are generated most efficiently, coherently and phase-locked. This has led to the conclusion, that the ROM method might be able to produce even shorter electromagnetic pulses in the zeptosecond¹⁹ regime.

At lower intensities or shorter wavelength of the driving laser the CWE model predicts a different phase dependence of the harmonics. In the simplified model²⁰ assuming the speed of the electrons reentering the plasma to be approximately the speed of light $v_e \approx c$, a linear density profile of the plasma, and an angle of incidence of 45° , the phase ϕ_q of the harmonics scales with the third power of the harmonic order: $\phi_q \propto q^3$

1.3 Characterization methods of attosecond pulses

One of the biggest challenges, that *attoscience* faces is the development of accurate and reliable temporal and structural analysis tools of the generated attosecond pulses. The duration τ_{XUV} of these electromagnetic pulses is orders of magnitude too short to be assessed directly with electric devices, such

¹⁷Plaja *et al.* (1998); Roso *et al.* (2000)

¹⁸Baeva *et al.* (2006)

¹⁹Gordienko *et al.* (2004)

²⁰Nomura *et al.* (2009)

as photomultipliers. Although this problem has been overcome for the characterization of femtosecond laser pulses by applying optical autocorrelation or cross-correlation techniques and well sophisticated methods like SPIDER²¹ or FROG²² are commonly used in many laboratories to assess femtosecond optical laser sources, for the purpose of attosecond metrology, these methods must be adapted to cope with four critical aspects: The shorter wavelength, the wider spectrum, the shorter pulse duration, and the often much lower pulse energy.

Different methods have been developed based either on an optical cross-correlation of the XUV attosecond pulses with a second laser field or on an autocorrelation technique of the attosecond pulses without the need for another laser field. Most are counterparts of the common femtosecond metrology methods. The cross-correlation methods require the precise knowledge of the second field—usually a part of the driving IR laser—to extract information about the spectral phase $\phi(\nu)$ of the XUV pulses. Together with their power spectrum $I(\nu)$ the pulses can be calculated by Fourier synthesis.

XUV-SPIDER The well known method of *spectral phase interferometry for direct electric-field reconstruction*²³ (SPIDER) can be transferred to the XUV spectrum in different ways. One way²⁴ is to generate two XUV attosecond pulses using two IR driving pulses, which are identical except for only a small shift in frequency $\delta\nu$, but also delayed with respect to each other by a time Δt . When using a grating spectrometer, then the spectrogram $I(\nu)$ of both XUV pulses together shows fringes from which the spectral phase $\phi(\nu)$ can be retrieved. Instead of the shift Δt in time, a shift Δx of the optical axis of the XUV pulses leads to spatial fringes on a two-dimensional detector of the spectrometer which again are a measure for the spectral phase. Another method²⁵ uses photoelectron (PE) wave packets as interfering media. For that, two delayed replicas of the same attosecond pulse, ionize atoms

²¹Iaconis and Walmsley (1998)

²²Trebino and Kane (1993)

²³Iaconis and Walmsley (1998)

²⁴Cormier *et al.* (2005); Mairesse *et al.* (2005)

²⁵Quéré *et al.* (2003)

in the presence of a more slowly varying electromagnetic field. This dressing laser field \mathcal{E}_L introduces an energy shift δE^{PE} between the two delayed photoelectron wave packets, causing their interference to show fringes in the energy spectrum $S(E^{\text{PE}})$. From these photoelectron energy spectra $S(E^{\text{PE}})$ the spectral phase $\phi_{\text{XUV}}(\omega)$ of the attosecond pulse can be deduced and thus the pulse can be reconstructed. The attosecond pulse duration τ_{XUV} must be substantially shorter than the period T_L of the dressing laser field in order to minimize the distortion of the photoelectron wave packets and the photoelectron spectra introduced by the variation $\dot{\mathcal{E}}_L = \frac{\partial}{\partial t} \mathcal{E}_L$ of the dressing field. The maximum attosecond pulse duration, for which this method is applicable, is about $\tau_{\text{XUV}} \lesssim 400$ as for a dressing field with a wavelength of $\lambda = 800$ nm. Up to now it was not possible to apply XUV-SPIDER to measure attosecond pulses.

Attosecond streak camera (ASC) In a very similar setup using only one pulse instead of the two replicas, the previously mentioned distortion, caused by the variation $\dot{\mathcal{E}}_L$ of the dressing field, can be utilized to deflect or accelerate the photoelectron wave packets.²⁶ In this way the time of ionization within the attosecond pulse can be mapped to the photoelectron energy spectrum $S(E^{\text{PE}})$ or an angular distribution $S(\theta)$ of the photoelectrons making this technique a sort of *attosecond streak camera* (ASC). Still the duration of the attosecond pulse τ_{XUV} must be shorter than half the period T_L of the dressing laser field in order for the streaking to happen during one single sweep of the dressing laser's electric field $\Rightarrow \dot{\mathcal{E}}_L \neq 0$. On the other hand, the pulse must be long enough, or the dressing laser's period must be short enough, so that the streaking is significant: $1/10 T_L \lesssim \tau_{\text{XUV}} < 1/2 T_L$. This method can not distinguish between a single attosecond pulse or a set of pulses separated in time $\delta t = n/2 T_L$ by a discrete number of half laser periods.

FROG CRAB Adding a delay Δt to the dressing laser beam to change its phase ϕ_L and recording the streaked spectra $S(E^{\text{PE}})$ or $S(\theta)$ for a series of different phases ϕ_L can circumvent the restriction on the pulse duration

²⁶Drescher *et al.* (2001); Itatani *et al.* (2002)

τ_{XUV} that the XUV-SPIDER and the ASC suffer from. This method is inspired by the common technique for femtosecond pulse metrology called *frequency-resolved optical gating* (FROG).²⁷ Using the effect of the dressing laser field as a "*phase gate*" instead of the temporal gate commonly used in femtosecond FROG implementations, makes it in principle possible with an iterative numerical method to do both the *complete reconstruction of attosecond bursts*²⁸ (CRAB) and also to extract the structure of the dressing laser pulse. The laser used to produce the attosecond pulse can be the same as the laser providing the dressing field for the phase gate.

RABITT In the special case of trains of attosecond pulses, as commonly produced by HHG from many-cycle lasers, the FROG CRAB spectra degenerate to lines of discrete energies. These discrete photoelectron energies correspond to the harmonics of the orders q . For harmonics produced from HHG in gases they are the odd multiples of the driving laser's photon energy $h\nu_L$ minus the ionization energy E_I of the parent atom: $E_{\text{main}}^{\text{PE}} = qh\nu_L - E_I$. If the dressing laser is the same as the driving laser for the HHG, then additional *side bands* appear at positions $E_{\text{side}}^{\text{PE}} = (q+1)h\nu_L - E_I$ centered between the main spectral lines from the harmonics. These *side bands* oscillate in intensity as the phase ϕ_L of the dressing laser changes. The period of the *side band* oscillation is half the period T_L of the dressing laser. The phase φ_{q+1} of the *side band* oscillation provides the phase difference $\Delta\phi_{q+1} = \phi_{q+2} - \phi_q$ between the two neighboring harmonics. Although this method cannot measure the harmonics' phases directly, the individual phases ϕ_q can be inferred one by one, with the residual uncertainty of a common phase offset ϕ_0 . This offset is usually chosen arbitrarily so that the phase of one of the observed harmonics is zero. The unknown common phase offset ϕ_0 does not change the duration of the reconstructed attosecond pulses but merely the carrier-envelope phase (CEP) offset inside the attosecond pulse. Even a first order (linear) increase of the phases ϕ_q with harmonic number q results only in a shift of the attosecond burst in time.

²⁷Trebino and Kane (1993)

²⁸Mairesse and Quéré (2005)

This method, the *reconstruction of attosecond beating by interference of two-photon transitions*²⁹ (RABITT), can be reduced to a set of cross-correlation traces. These traces are the intensities of the *side band* peaks $S_{q+1}(\Delta t)$ as a function of the delay between the attosecond pulse train and the dressing laser.

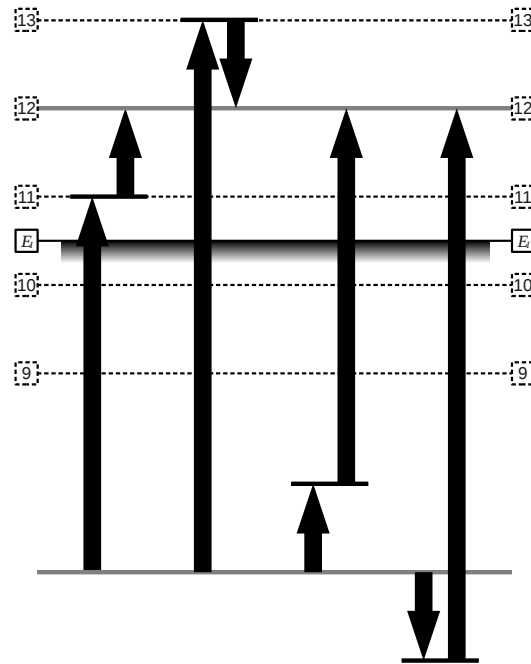


Figure 1.3: Transition diagram for RABITT

Four quantum paths lead to the emission of a photoelectron to the *side band* with energy $E_{12}^{\text{PE}} = 12h\nu_L - E_I$:

- Absorption of a harmonic γ_q and a fundamental γ_L
- Absorption of a harmonic γ_{q+2} and stimulated emission of a fundamental γ_L
- Absorption of a fundamental γ_L and a harmonic γ_q
- Stimulated emission of a fundamental γ_L and absorption of a harmonic γ_{q+2}

The numbers indicate the energy in units of $h\nu_q$. The position of the ground state is not to scale.

The underlying physical process, which gives rise to these *side band* oscillations, can be understood as a quantum interference between different two-color two-photon transitions ionizing the atoms illustrated in Figure 1.3.

²⁹Paul *et al.* (2001)

They involve both a harmonic photon γ_q and a photon from the fundamental dressing laser γ_L . There are four interfering quantum paths for each *side band*, which transfer the same energy $\Delta E_{q+1} = (q+1)h\nu_L$ from the electromagnetic field to the atom:

- a) Absorption of a harmonic photon γ_q and one of the fundamental γ_L
- b) Absorption of a harmonic photon γ_{q+2} and stimulated emission of one of the fundamental γ_L
- c) Absorption of a photon of the fundamental γ_L and one of a harmonic γ_q
- d) Stimulated emission of a photon of the fundamental γ_L and absorption of a harmonic photon γ_{q+2}

The paths a) and b) resemble the paths c) and d), respectively, except for the order of interaction, the virtual state involved and thus the transition probability. The phases of the interacting photons determine the phase of the emitted electron wave packets: For the IR+XUV quantum paths a) and c) the electron's phase is $\phi_e^+ = \phi_q + \phi_L + \phi_{\text{atom}}$ and for the IR-XUV quantum paths b) and d) it is $\phi_e^- = \phi_{q+2} - \phi_L + \phi'_{\text{atom}}$. So the *side band* photoelectron signal S_{q+1} shows interference oscillations from the two quantum paths with ϕ_e^+ and ϕ_e^- , if the phase ϕ_L of the fundamental laser field changes with respect to the harmonic radiation:

$$\begin{aligned}
 S_{q+1} &\propto S_0 + \cos(\phi_e^+ - \phi_e^-) \\
 &= S_0 + \cos(2\phi_L + \phi_q - \phi_{q+2} + \Delta\phi_{\text{atom}}) \\
 &= S_0 + \cos(2\omega_L\Delta t + \varphi_{q+1})
 \end{aligned} \tag{1.7}$$

Applying a delay Δt to the fundamental laser and thus changing the phase $\phi_L = \omega_L\Delta t$ results in oscillations of the two-color photoelectron signal with a period of $\frac{1}{2}T_L$. The cross-correlation trace $S_{q+1}(\Delta t)$ of the *side band* $q+1$ oscillates with a phase offset of $\varphi_{q+1} = \phi_q - \phi_{q+2} + \Delta\phi_{\text{atom}}$. The atomic phase difference $\Delta\phi_{\text{atom}}$ can be calculated and is usually assumed to be negligibly small, so the phase offset φ_{q+1} determines the phase difference $\Delta\phi_{q+1}$ between

the two consecutive harmonics q and $q+2$. Iterative the phases of all harmonics involved can be deduced and together with the measured intensities of the harmonics the attosecond waveform can be reconstructed. Since the phase offset φ_{q+1} is not measured in a single-shot method, the result gives the phases $\langle\phi_q\rangle$ averaged over a number of entire pulse trains and averaged over the full beam cross-section. Together with the measured harmonic intensities $\langle I_q\rangle$, which are also averaged over the entire trains and cross-section, the reconstruction gives merely a "mean" attosecond pulse shape. This may result in undesirable effects as analyzed more thoroughly later in Section 3.1.2.

The *in situ* method A quite different approach, called the *in situ*³⁰ method, aims to characterize the harmonics at the place where they are generated, which is at the focus of the driving laser inside the harmonics generating gas medium. For this to happen, a weak co-propagating second harmonic component of the driving laser ($\frac{I_2}{I_L} < 10^{-3}$) present at the harmonics generating region breaks the symmetry of the interaction and causes emission of harmonics with even order $q \in \{4, 6, 8, \dots\}$. The relative intensities of these even harmonics depend on the phase ϕ_2 of the second harmonic relative to the fundamental. Similarly to the RABITT approach, the oscillations of the even harmonics can be used to determine the emission times and thus to reconstruct the attosecond pulse.

2-IVAC All the above techniques base on a cross-correlation of the XUV attosecond pulses to be characterized with a dressing laser. These methods then somehow extract the spectral phase of the XUV radiation from the cross-correlation signal and together with the intensity spectrum the waveform gets reproduced. A more basic and more direct assessment of an ultra short light pulse is its autocorrelation (AC). A simple and very common method to record an AC trace duplicates or splits the pulse into two replicas and delays one of the pulses for a short time Δt . The two replicas are convoluted by measuring with a slow detector a signal $S_1 \propto |\mathcal{E}(t) + \mathcal{E}(t - \Delta t)|^2$ proportional

³⁰Dudovich *et al.* (2006)

to the intensity of the electromagnetic field \mathcal{E} comprising the superposition of both pulses.

$$\begin{aligned}
 S_{1AC}(\Delta t) &= \int_{-\infty}^{+\infty} S_1(t, \Delta t) dt \propto \int_{-\infty}^{+\infty} |\mathcal{E}(t) + \mathcal{E}(t - \Delta t)|^2 dt \\
 &\propto \int_{-\infty}^{+\infty} \underbrace{|\mathcal{E}(t)|^2 + |\mathcal{E}(t - \Delta t)|^2}_{\text{constant background}} + 2 \underbrace{\mathcal{E}(t)\mathcal{E}(t - \Delta t)}_{\text{1st order AC term}} dt
 \end{aligned} \tag{1.8}$$

Measuring this signal $S_{1AC}(\Delta t)$ as a function of the delay between the two replicas results in an AC trace with a constant background. The last term in Equation 1.8 is the *first-order autocorrelation* (1AC) term. It includes the cross-term of the expansion of S_1 . The other two terms of the integral are equal and do not depend on the delay Δt . They constitute the background.

The Fourier transform of the 1AC is proportional to the power spectrum $I(\nu)$ of the electromagnetic pulse and the envelope of the 1AC trace bears the coherence length of the pulse. Besides that, no further information can be obtained about the duration τ_p or the spectral phase $\phi(\nu)$ of the pulse.

The *second-order autocorrelation* (2AC) can reveal the duration of the pulse. To achieve this it is necessary to measure a signal $S_2 \propto S_1^2 \propto |[\mathcal{E}(t) + \mathcal{E}(t - \tau)]|^2|^2$ that is proportional to the intensity of the square of the superposition of the two pulses. This is usually achieved by means of a nonlinear optical element like a beta barium borate (BBO) crystal to generate the second harmonic. If the resolution of the 2AC trace is good enough, then it can reveal information on both the pulse duration τ_p and the coherence length.

In the case of attosecond pulses consisting of high harmonics from a $\lambda = 800$ nm laser, other means of beam splitting and nonlinear detection are necessary in order to match the shorter wavelengths. A mirror, cut into two symmetric halves, can provide a dispersion-free way to split the wave front and delay one part of the split beam by moving one of the halves along the beam axis. A non-resonant two-photon ionization of a suitable gas can

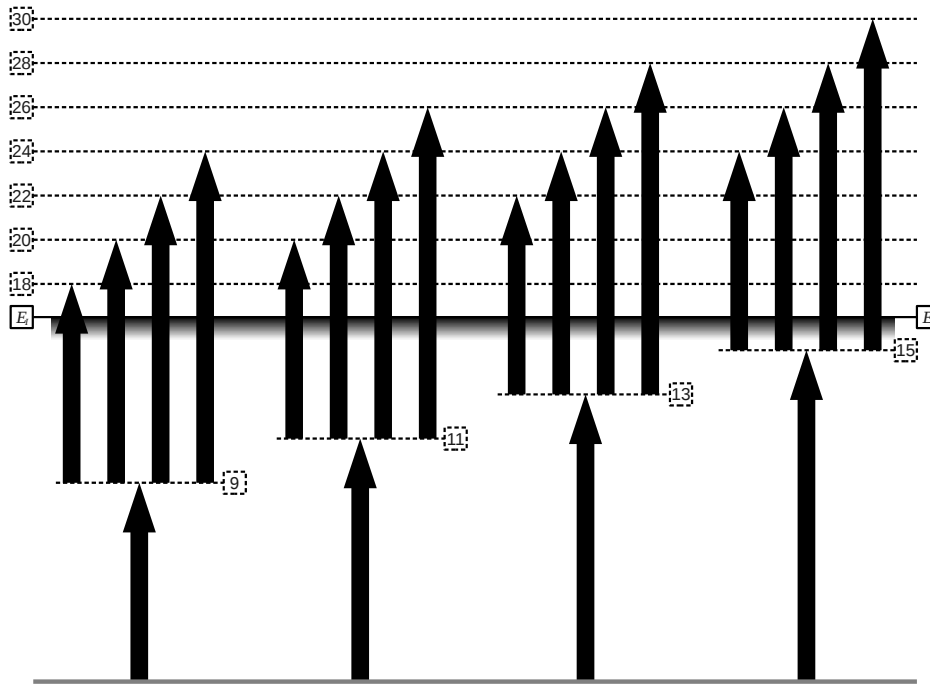


Figure 1.4: Transition diagram for a second-order volume-autocorrelation

With helium taken as an example target atom for the non-linear process, a single harmonic photon below the 16th can not ionize the atoms, but any two photons from the harmonics 11–15 can ionize helium. The numbers indicate the energy in units of $h\nu_q$.

be used as a non-linear optical process with an instantaneous response and a constant sensitivity over a wide spectral range.³¹ Bringing the two halves of the split beam together to a common focus as shown in Figure 1.5 in a volume of interaction with a suitable gas results in an ion yield that is very similar to a standard 2AC, but with a reduced peak-to-background ratio of 2.8 for a fringe resolved 2AC and 2.1 for a cycle-averaged intensity 2AC.³² Since the "detector" is actually the entire interaction volume this method is called *volume-autocorrelation* (VAC).

Both the delay and the focusing can be achieved simultaneously by one

³¹Descamps *et al.* (2001); Nikolopoulos *et al.* (2005); Tzallas *et al.* (2005); Benis *et al.* (2006)

³²Faucher *et al.* (2009) and references therein

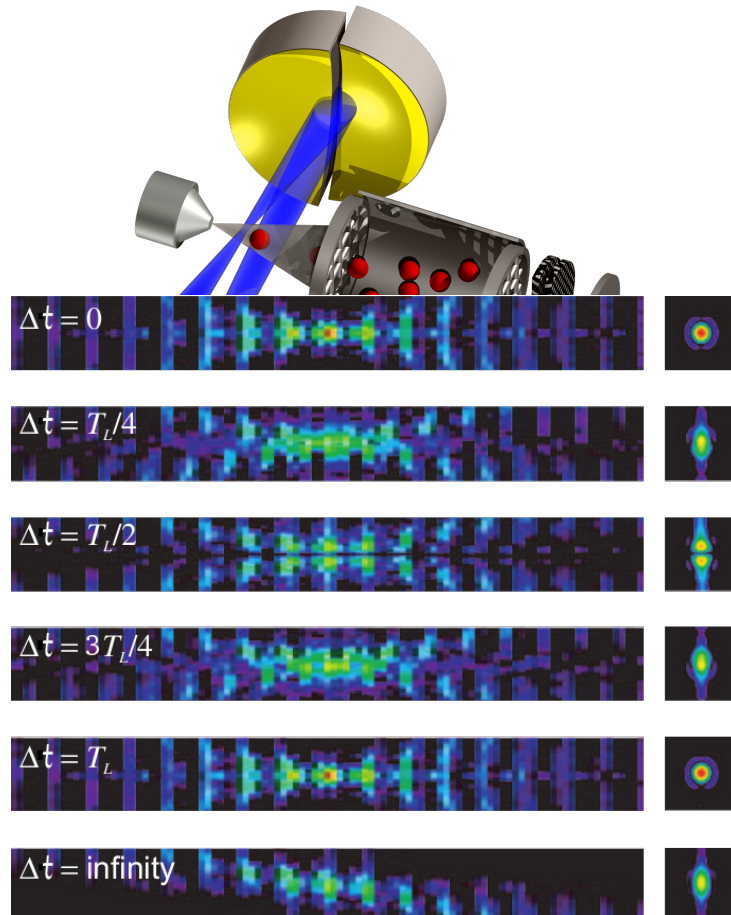


Figure 1.5: Electric field at the focus of a split mirror

The illustration at the top shows a split spherical gold mirror focusing the XUV beam (blue) inside a gas jet with a time-of-flight spectrometer (TOF) detecting the ions (red). The color plots show the calculated electric field's intensity distribution $|\mathcal{E}|^2$ at the focus of a split mirror in logarithmic scale over three decades for different delay Δt . Panels on the left show a section along the beam axis and perpendicular to the slit of the split mirror. Panels on the right show a beam cross section at the focal plane of the static half mirror. The electromagnetic field is a superposition of the four harmonics 7, 9, 11 and 13 with equal amplitudes reflected from a split spherical mirror with $f = 15$ cm focal length.

Source: Tzallas *et al.* (2005)

split spherical mirror cut into two symmetric halves. In this case the maximal displacement d_{\max} of the movable half of the split mirror should be less or similar to the Rayleigh range of the focus z_R . The reflection doubles the delay $\Delta t = 2\frac{d}{c}$ introduced by the displacement d . Since the displacement of the mirror half can be both directions, either towards the focus or away from the focus, the full range τ_{\max} is twice the maximal temporal delay per direction: $\tau_{\max} = 2 \cdot \Delta t_{\max} \lesssim \frac{4}{c} z_R$

In contrast to the conventional 2AC, where the two pulses are separated and recombined by an optical beam splitter that divides the *intensity* of the incoming beam between the two replicas, the volume-AC divides the *wave front* into two. Therefore the recombination of the beams at the detector results only in a redistribution of the pulse energy inside the interaction volume, never in a mutual cancellation of the two pulses across all of the detector. The volume-AC can therefore be normally used only for higher order processes and not for a first order autocorrelation. This restriction applies only for a detector, which is homogeneous throughout all of the detection volume. It can be seen from Figure 1.5, that at different delay values Δt different areas receive more energy. An asymmetric or spatially selective detector could therefore be used even for a first order process.

If the resolution of the system is good enough, then the trace can show interferometric oscillations which contain information about the spectrum of the pulse. Otherwise, if the VAC trace measures only a cycle average, then the intensity envelope can be deduced from the trace. The ratio of the width of such a *second-order intensity volume-autocorrelation* (2IVAC) trace τ_{2IVAC} compared to the duration of a Gaussian light pulse τ_p was found numerically³³ to be $\tau_{2IVAC} = 1.41 \tau_p$. This is the same as the factor $\frac{\tau_{2AC}}{\tau_p} = \sqrt{2}$ that can be deduced analytically for a conventional 2AC.

PANTHER Instead of detecting the ions produced by the two-photon ionization of the second-order volume-autocorrelation, it is possible to detect the photoelectrons of the two-photon transition for a method called *pho-*

³³Faucher *et al.* (2009)

*photoelectron analysis with non-resonant two-photon-ionization for harmonic electric-field reconstruction*³⁴(PANTHER). These can be energy-resolved using a magnetic-bottle time-of-flight spectrometer, so that the photoelectron spectrum $S(E^{\text{PE}})$ show peaks at the positions $E_{\text{PANTHER}}^{\text{PE}} = 2qh\nu_L - E_I$. In the case of a set Q of harmonics, there can be different modes involved in the formation of each peak. These can be from two photons of the same harmonic order ($q + q$). But also the combination of one photon from a lower order ($q' = q - n$) and another photon from a higher order ($q'' = q + n$) results in the same photoelectron energy as in the case of two photons from the same harmonic: $q' + q'' = q + q$. The delay between the two pulse replicas gives rise to interference oscillations in the two-photon photoelectron peaks from which again the phase and the relative intensity of the contributing harmonics can be deduced. This method is equivalent to the common FROG implementations used for femtosecond metrology that use a second-harmonic-generating BBO crystal.

³⁴Nabekawa *et al.* (2006)

Experimental setup

2.1 Ti:sapphire laser system

All experiments of the present thesis are using the same light source produced by Amplitude Technologies. It provides infrared laser pulses with $\lambda_L = 800$ nm central wavelength. The energy of the pulses can be up to $E_L = 170$ mJ and the duration down to $\tau_L = 40$ fs (FWHM). The cross-section of the laser beam is roughly homogeneously circular with about $d_L \approx 5$ cm diameter. The laser system providing these light pulses comprises six major parts that constitute a *chirped pulse amplification* (CPA) system:

Oscillator A mode-locked titanium-doped sapphire laser oscillator, pumped by a neodymium-doped yttrium aluminium garnet (Nd:YAG) laser made by Coherent Inc., provides the initial laser pulses of $E_{\text{OSC}} = 7$ nJ energy per pulse at $\lambda_{\text{OSC}} = 800$ nm central wavelength. The duration of these pulses is about $\tau_{\text{OSC}} \approx 30$ fs at a repetition rate of $\nu_{\text{OSC}} = 75$ MHz.

Stretcher Two optical gratings inside the stretcher add a strong chirp to the pulses in the pulse-train from the oscillator separating the spectral components in time.

Regenerative amplifier The chirped pulses are firstly amplified in a regenerative amplifier, pumped by an Nd:YAG laser made by Photonics Industries. This leads to a pulse energy of $E_{\text{REGEN}} = 6$ mJ.

Multi-pass amplifiers The first multi-pass amplifier, pumped also by an Nd:YAG from Big Sky Laser Technologies, increases the laser energy to $E_{1MP} = 24$ mJ per pulse. The second one, pumped by another Nd:YAG from Amplitude Technologies, reaches the maximal pulse energy of $E_{2MP} = 340$ mJ

Compressor Eventually another two optical gratings reverse the effect of the stretcher and re-compresses the chirped and amplified pulses down to $\tau_L = 40$ fs at the final pulse energy of $E_L = 170$ mJ.

2.2 Generation of harmonic radiation

There are two vacuum chambers, in which the generation of high harmonics can take place, one for the HHG in gases and one for the HHG from surfaces. After the laser pulses leave the compressor, a system of slidable mirrors directs them to the respective chamber.

2.2.1 Glass target

For efficient generation of harmonics from solid targets, the laser intensity at the plasma surface should be as high as possible. Figure 2.1 depicts a schematic of the experimental setup used, where a gold-coated off-axis parabolic mirror (PM1) with effective focal length of $f_{PM} \approx 8$ cm focuses the infrared laser with an initial diameter of $D_L = 5$ cm very tightly to a focal spot with a diameter of $w_0 \approx 6$ μm at the surface of a glass target (T). Pulses with $E_L = 150$ mJ energy within $\tau_L = 50$ fs focused at $A_f \approx 30$ μm^2 reach intensities above the relativistic limit of $I_L \approx 2.2 \times 10^{18}$ W/cm². Since every laser pulse creates a damage on the target's surface, rendering that spot unusable for another pulse, the target must be moved in between the pulses by the size of the damage left behind. To achieve this, the circular glass targets are mounted on a rotation stage which itself is fixed to a translation stage. Stepper motors provide the controlled movement of both stages. The combined movement of rotation and translation makes the series of damage

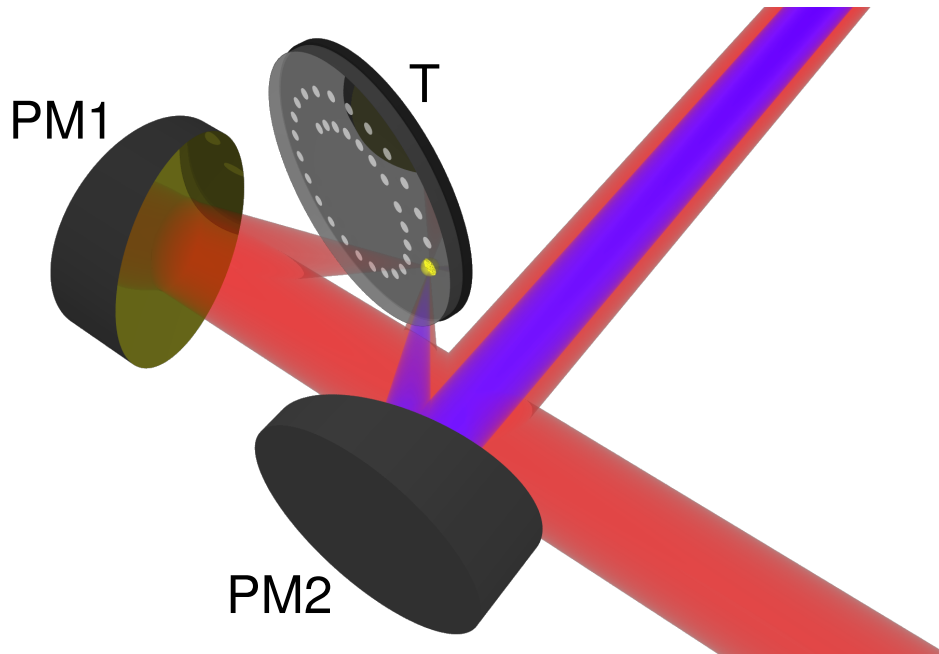


Figure 2.1: Experimental setup for harmonic generation from surfaces

An off-axis parabolic mirror (PM1) focuses the fundamental infrared laser radiation (red) onto a rotating glass target (T) to create a plasma (yellow) on the target's surface. A second off-axis parabolic mirror (PM2) collimates the reflection from the plasma including the harmonic radiation (blue beam). The gray dots on the target illustrate the damages left behind from previous laser pulses.

marks describe a spiral on the targets surface. The reflection from the target's plasma is collimated by a second off-axis parabolic gold mirror (PM2). A spherical mirror condenses the radiation at the entrance slit of a grating spectrometer equipped with a multi-channel-plate and a phosphor screen. A digital camera records the image of the spectrum on the phosphor screen.

The central wavelength of the grating spectrometer λ_{GS} was adjusted to examine different spectral regions around $\lambda_{GS} \approx 80$ nm, $\lambda_{GS} \approx 90$ nm, and $\lambda_{GS} \approx 110$ nm. The corresponding spectra are displayed in Figure 2.2. No harmonic radiation could be observed in the recorded spectra. The spectral lines visible in Figure 2.2 are emission lines from oxygen.¹ The line identification plot for neutral oxygen in the middle left panel illustrates a possible match for the observed lines. The limited resolution of the spectrometer is

¹Moore (1976), page A8 1-2

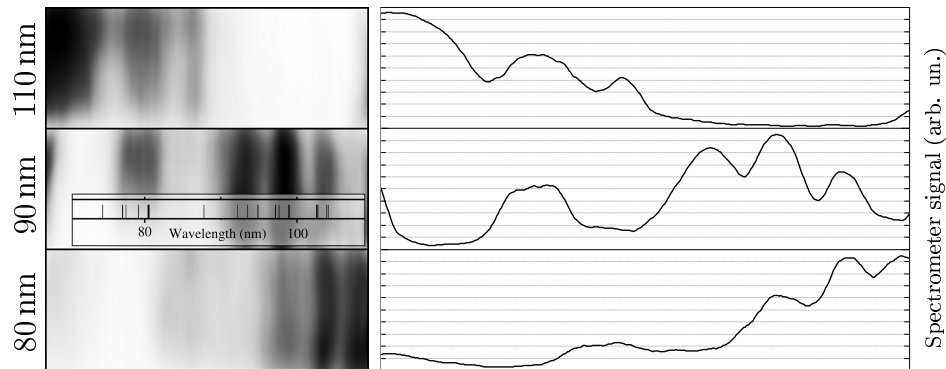


Figure 2.2: Spectrum from surface plasma

The left panel shows the phosphor screen of the spectrometer at three different central wavelengths near 80 nm, 90 nm, and 110 nm. The right panel shows the corresponding vertically averaged brightness for each position, respectively. The images have been inverted and adjusted in brightness and contrast. The inset in the middle left panel shows a line identification plot for neutral oxygen from NIST.

due to the width of the entrance slit. The positions of the spectral lines on the phosphor screen are not exactly proportional to their wavelength, so the match with the identification plot is only approximate.

The lack of harmonic radiation is due to a pre-pulse in the temporal profile of the infrared laser. The intensity trace taken with a fast photomultiplier tube (PMT) shown in Figure 2.3 reveals the pre-pulses at 9 ns and 18 ns before the main pulse. These pre-pulses have only about 0.01% of the energy of the main pulse, but because of the tight focusing geometry they are strong enough to create a rapidly expanding pre-plasma on the surface of the target. This makes the the surface unusable for high harmonic generation from the upcoming main pulse, because shortly after, at the time of arrival of the main pulse, there is no steep plasma density gradient anymore.

The distance between the two pre-pulses and the main pulse indicate, that the origin of the pre-pulses lies in the regenerative amplifier described in Section 2.1 and the imperfect switching of the pockels-cells. The 9 ns distance between the pulses are exactly the round trip through the cavity of the regenerative amplifier.

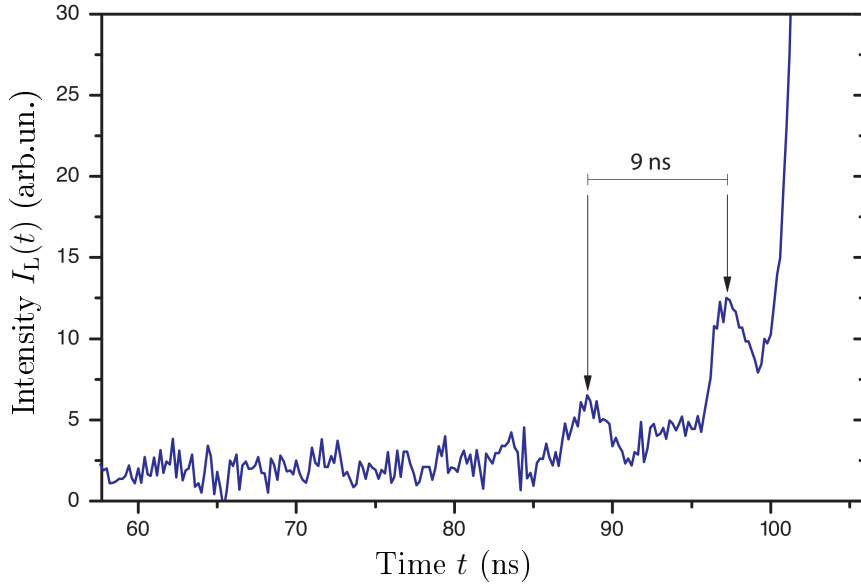


Figure 2.3: Intensity trace of the driving laser

The trace of $I_L(t)$, taken with a fast photo-multiplier tube, shows two pre-pulses at $t = -9$ ns and $t = -18$ ns with pulse energies of $\sim 10^{-4} E_L$.

Source: Robotis (2009)

2.2.2 Xenon gas jet

The setup used to produce harmonic radiation from gases is displayed in Figure 2.4. As a first step a beam shaper (BS) adjusts the diameter of the infrared laser to about $d_L \approx 2$ cm and blocks a central part of $d_{BS} \approx 8$ mm diameter giving the beam an annular shape with $E_L \approx 13$ mJ energy per pulse. In order to achieve a high conversion ratio from the fundamental infrared laser radiation into high harmonics, a lens (L) with $f_L = 3$ m focal length focuses the driving laser very loosely into a pulsed jet of xenon atoms (J1). The jet is situated in a vacuum chamber with an ambient pressure of $P_{HHGG} < 10^{-5}$ mBar during operation of the gas jet. Here the harmonics are generated and propagate together with the opening infrared driving pulse, but with smaller angular divergence. Two measures reduce the intensity of the annular infrared after this point: Firstly the reflection of the pulse from a silicon wafer (SW), placed at the Brewster's angle of the infrared, re-

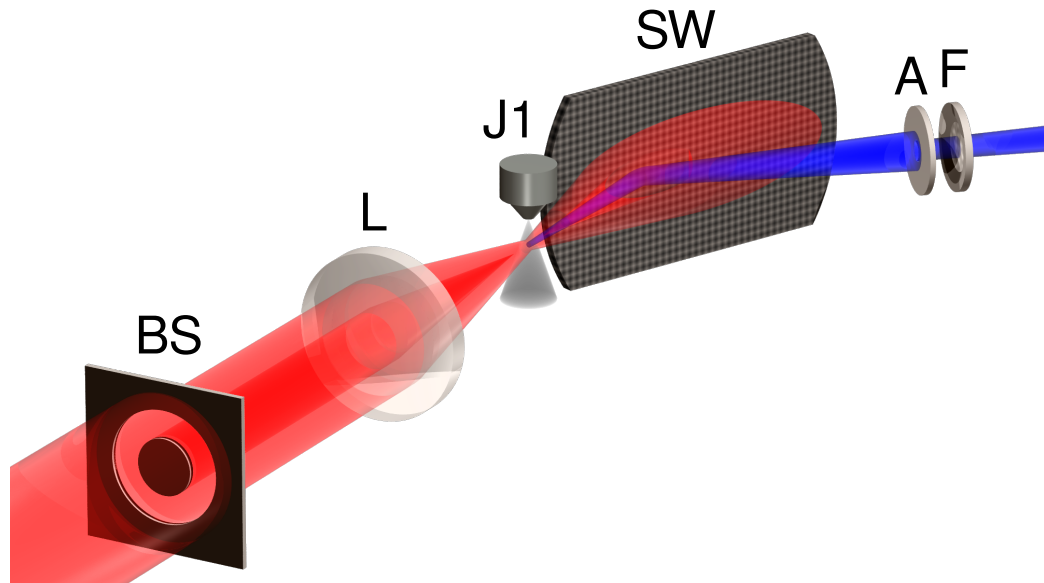


Figure 2.4: Optical setup for harmonic generation in gas targets

A beam-shaper (BS) gives the incoming infrared laser (red beam) an annular shape. A lens (L) focuses the laser at a jet (J1) of xenon atoms which generates the high harmonic XUV radiation (blue beam). A silicon wafer removes the infrared and reflects the harmonic XUV radiation. An aperture (A) blocks the residual annular part of the infrared and lets the central part of the XUV pass. A filter (F) can be inserted into the beam to select a suitable spectrum from the harmonics.

duces the intensity of the p-polarized infrared by more than 99%.² Secondly an aperture (A) lets the central harmonics pass but blocks the outer part of the beam, which contains the residual infrared from the annular beam reflected by the wafer. If necessary, an optical filter (F) can be inserted after the aperture to select a spectral region suitable for the respective experiment.

Figure 2.5 shows a measurement of the beam diameter of the harmonics using a knife-edge technique. The derivative of the photoelectron signal from the harmonics reveals a beam diameter of $d_{\text{XUV}} = 2.3 \text{ mm}$ (FWHM) at the position of the aperture, when the lens (L) is at the position to focus the driving IR at z_B before the gas jet (J1). The lens can be shifted along the optical axis in order to move the focus either before, inside or after the xenon gas jet. Photoelectron time-of-flight spectra of the harmonics focused in an

²Takahashi *et al.* (2004)

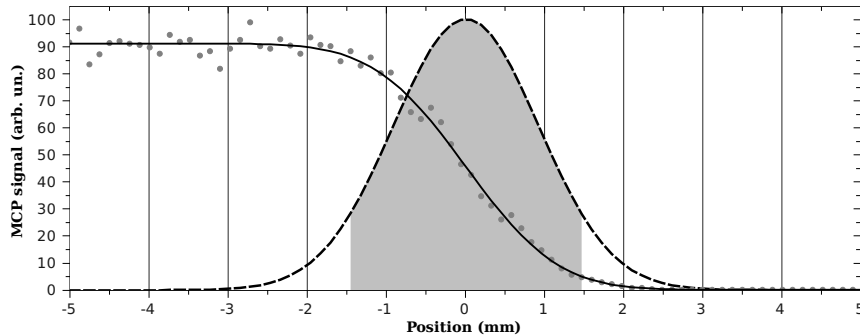


Figure 2.5: Diameter of the harmonic radiation

Inserting the edge of a knife to block a part of the XUV beam while recording the photoelectron spectra as a function of the knives position reveals the diameter d_{XUV} of the harmonics. The aperture (A) was replaced by a slit of 1.5 mm width, so that the scan is effectively across the center of the beam. The gray dots are the measured photoelectron signals. The solid line is an error function fit to the measured data. The dashed line is the derivative of the fit. The gray area illustrates an aperture of $d_{\text{A}} \approx 3$ mm.

argon gas jet were recorded while moving the lens and driving the focus through the gas medium using an aperture of $d_{\text{A}} = 3$ mm and no filter (F). The signal of the photoelectron peaks from the harmonics 11, 13, 15, and 17 are shown in Figure 2.6 in dependence of the focus position z_{f} . The three arrows indicate the focus positions before (z_{B}), inside (z_{I}), and after (z_{A}) the gas jet, which were used for the attosecond pulse metrology measurements described in Section 3.1.

2.3 Characterization and application system

After the XUV radiation is separated from the driving laser by the silicon wafer and the aperture, different filters (F) can be used to select the part of the harmonic spectrum suitable for the respective experiment. Autocorrelation, cross-correlation, and *pump-probe* measurements can be performed in the detection area of the vacuum chamber, which is separated from the HHGG chamber by differential pumping. As illustrated in Figure 2.7, it is equipped with a split spherical mirror (SM) used as a wave-front splitter, an interaction gas jet (J2), and a time-of-flight spectrometer (TOF).

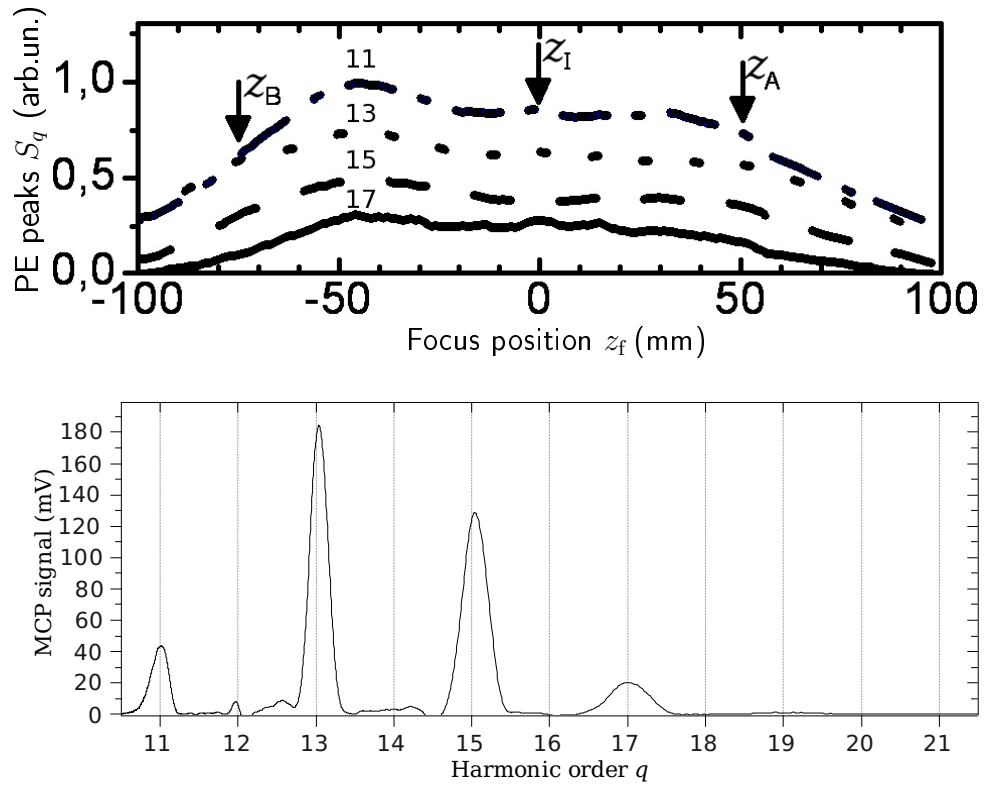


Figure 2.6: Harmonic generation at different focus positions

The intensities of the individual harmonics depend on the position of the focus relative to the xenon gas jet. The top panel shows the photoelectron (PE) signals S_q as a function of the focus position z_f for the harmonics 11, 13, 15, and 17 by the dash-dotted, the dotted, the dashed, and the solid line, respectively. The bottom panel shows a recorded photoelectron-energy spectrum with re-scaled abscissa showing the peaks from the harmonic orders 11, 13, 15, 17, and 19. The spectra were recorded with an aperture of $d_A = 3$ mm

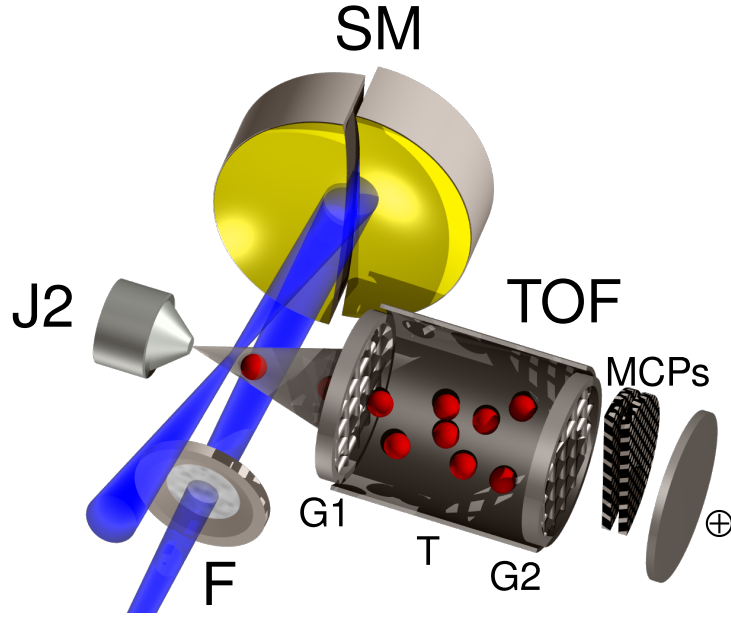


Figure 2.7: Schematic of the characterization and application system

The vacuum chamber containing the detectors is equipped with a place to insert a filter (F), with a split mirror (SM), and with a time-of-flight spectrometer (TOF) composed of two grids (G1,G2), a field-free drift tube (T), two microchannel plates (MCPs), and an the anode (\oplus).

2.3.1 Wave front splitting device

The dispersion-free wave-front splitter consists of a gold-coated spherical mirror (SM), which is cut into two symmetric halves. Each of the two half mirrors is mounted on a piezoelectric actuator. One side is fixed to a coarse $\vartheta/\varphi/\Delta z_c$ tilting-translation stage, which can be shifted along the beam axis and tilted horizontally and vertically in order to overlap the two foci of both mirror halves. The other half can be shifted along the beam axis by a fine Δz_f nanometer-resolution piezoelectric feedback-controlled translation stage to introduce a small controllable delay $\Delta t = \frac{2}{c} \Delta z_f$ between the two replicas of the XUV pulse. A calculation of the intensity at the focus of the split mirror³ is shown in Figure 2.8. It is based on the spatial and temporal distribution of the electromagnetic field at the focus over a volume of 20 times the focal

³Faucher *et al.* (2009)

spot diameter w_0 in width and height and 26 times the Rayleigh range z_R in length of the 5th harmonic assuming a Gaussian pulse.

A gas jet J2, placed at the focus of the split mirror, serves as detection medium. The gas atoms are ionized by the electromagnetic field composed from the superposition of the two foci.

Resolution of the delay stage

High resolution autocorrelation or cross-correlations measurements of attosecond pulses require a very fine scan of the delay Δt between the two overlapping beams by small displacement steps δz of a few nanometers. The stability of both halves of the split mirror — the coarse alignment half and the fine precision half — is critical, since both halves are needed to overlap the two replicas in space and time. The feedback control of the coarse $\vartheta/\varphi/\Delta z_c$ tilting-translation stage lacks the necessary accuracy to stay within a small fraction of a wavelength of the driving laser. For this reason the feedback for the coarse control is disabled and the piezoelectric crystals are given enough time to relax towards their final position, typically a few hours or over night. According to the specifications of the actuator from *piezosystem jena* GmbH, the feedback controlled fine precision delay stage can reach a maximum resolution of $\delta z_f = 1.5$ nm. The actual resolution of the system is further limited by vibrations and other inaccuracies. AC traces of different orders and of radiation with different wavelengths were taken to evaluate the achievable precision of the delay.

IR autocorrelation A series of high-order autocorrelations of the IR driving laser pulse gave a first quick evaluation of the stability and hysteresis of the delay stage. With the first gas jet (J1) closed and the beam shaper (BS) removed, the silicon wafer (SW) reflects a small fraction of the infrared laser beam towards the split mirror (SM), which focuses the residual IR into the second gas jet (J2) of argon. The condensed infrared at the focus of the split mirror causes a multi-photon ionization of the argon atoms. A repulsion voltage of $U_{\text{rep}} = 4$ kV on the case of the argon jet's nozzle accelerates

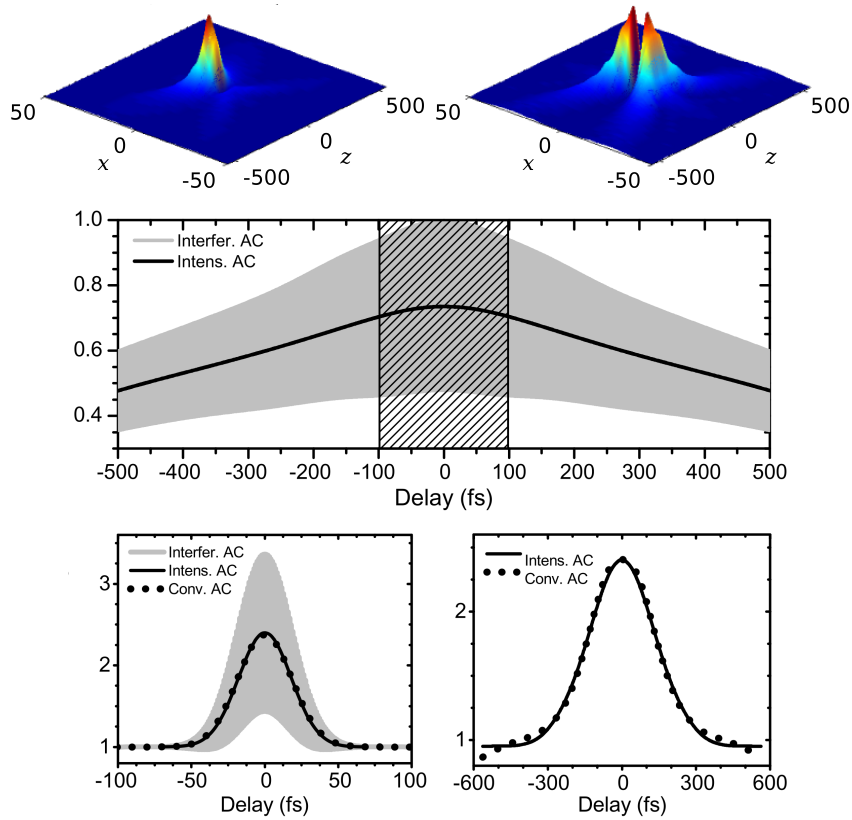


Figure 2.8: Simulation of the second-order volume-autocorrelation

The 3D-color plots show the calculated intensity distribution at the focus of the split mirror for different delay values Δt . The top left plot shows the two overlapped foci with a mirror displacement of $\Delta z = \lambda/8$, which corresponds to a temporal delay of $\Delta t = 1/4 T_L$. The top right plot shows the two overlapped foci with a mirror displacement of $\Delta z = \lambda/4$, which corresponds to a temporal delay of $\Delta t = 1/2 T_L$. The z -direction is along the optical axis, the x -axis is perpendicular to the slit of the split mirror.

The middle panel shows the calculated signal for a second-order intensity autocorrelation (solid line) and for a fringe-resolved interferometric autocorrelation (gray area) as a function of the delay Δt for a constant-wave laser. The decrease at higher delay values is due to the displacement Δz of the two foci. The hatched area around $\Delta t = \pm 100$ fs corresponds to the negligible deviation of less than 5%.

The bottom panels show two sets of calculated second-order autocorrelation traces to compare the conventional co-linear autocorrelation (black dots) to the volume-autocorrelation (solid line and gray area) for a 30 fs pulse in the left bottom panel and for a 200 fs pulse in the right bottom panel. The peak-to-baseline ratio was adjusted to overlap the two curves.

Source: Faucher *et al.* (2009)

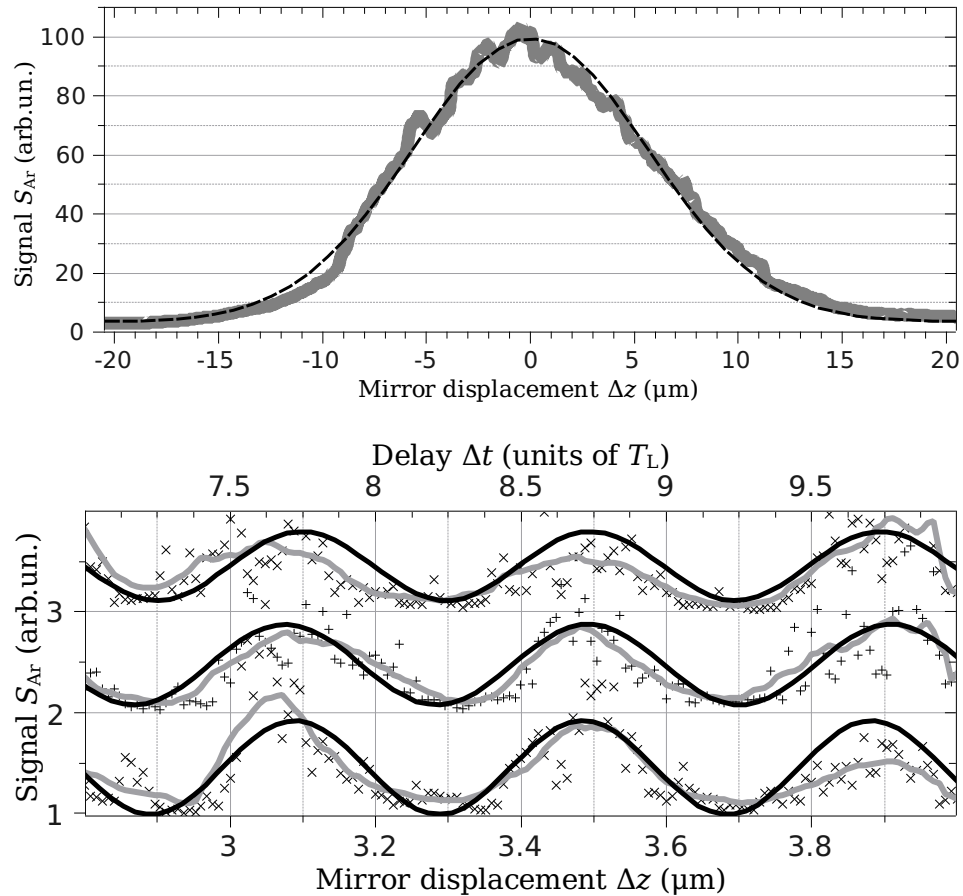


Figure 2.9: High-order autocorrelation of the infrared

The top panel shows a high-order interferometric volume-autocorrelation of the infrared laser pulse using the split mirror as delay stage and the multi-photon ionization of argon as non-linear detector. The thick gray line is a running average over 10 cycles. The dashed black line is a Gaussian fit to the measured data.

The bottom panel shows three consecutive AC high-resolution traces of a small part scanning the delay in both directions back and forth. A vertical offset was added to the single traces for clarity. The crosses are the direct single-pulse data points without averaging. The diagonal crosses are from the reverse traces. The thick gray lines are running averages over 15 data points. The thin black lines are sinusoidal fits to the single-pulse raw data.

the ions towards the time-of-flight spectrometer (TOF), where they are detected. Figure 2.9 shows a cycle-averaged high-order interferometric volume-autocorrelation (HiVAC) of the entire driving laser pulse and a set of five consecutive fringe-resolved HiVAC traces of a small region, with the delay being scanned in both directions back and forth. The interference fringes can be clearly resolved and the five consecutive traces show no significant hysteresis between the two scanning directions.

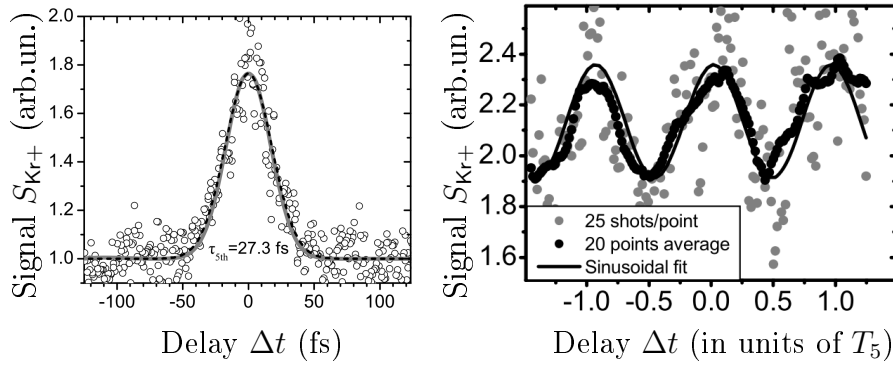


Figure 2.10: Interferometric autocorrelation of the fifth harmonic

The gray dots show the integral over the argon peak from the TOF-spectra. The left panel corresponds to the coarse scan and reveals the duration of the fifth harmonic emission. The fine scan of the autocorrelation in the right panel shows the interferometric oscillations of the fifth harmonic.

1.87 PHz autocorrelation The system's resolution must be much better than the infrared wavelength, in order to take a 2IVAC with the necessary precision to resolve attosecond pulses. The fifth harmonic of the laser has a wavelength of $\lambda_5 = 160$ nm and a period of $T_5 = 534$ as. Figure 2.10 shows both the 2IVAC measuring the intensity envelope of the fifth harmonic radiation pulse and the fine-resolution second-order interferometric volume-autocorrelation (2iVAC) scan revealing the interference of the two replicas. The measurements was taken under the same conditions as described in Section 3.3. The 2IVAC envelope verifies a pulse duration of $\tau_5 = 27 \pm 2$ fs and the 2iVAC fine scan shows the oscillations with the period of the fifth harmonic ensuring a detector resolution in the attosecond time scale. In order to resolve these oscillations with at least four samples, the delay step reso-

lution $\delta t = \frac{2}{c} \delta z_f$ must be less than a quarter of the period $\frac{1}{4}T_5 = 133$ as. This corresponds to an effective resolution of the split-mirror displacement of at least as good as $\delta z_f < 20$ nm.

2.3.2 Time-of-flight spectrometer

Both ionization products, either electrons or ions, can be detected by the Mu-metal-shielded time-of-flight spectrometer (TOF) shown in Figure 2.7. It can be used as an electron-energy spectrometer or, by applying an electric repulsion potential U_{rep} , as an ion-mass spectrometer. Particles passing the first grid (G1) drift through the field-free tube (T) until they reach the second grid (G2) from where they are accelerated towards the micro-channel plates (MCPs). The output electrons from the first MCP enter a second plate for further amplification and its output electrons eventually hit the anode (\oplus) to produce the signal detected by a digital phosphor oscilloscope displayed in Figure 2.11. The orientation of the two MCPs is opposite, since one is rotated by 180° with respect to the other around their surface normal, in order to prevent any particles from passing both MCPs without hitting a micro-channel's wall.

In order to measure either electron-energy spectra or ion-mass spectra as shown in Figure 2.11, the grids (G1, G2) and the tube (T) are grounded and the anode (\oplus) is at a high positive voltage. The voltage drop across the MCPs can be adjusted to a value of up to 1.2 kV each. A capacitor decouples the steady high voltage potential of the anode (\oplus) from the fast low voltage pulses generated by the MCP's electrons, so they can be detected by a TektronixTM digital phosphor oscilloscope. The signal from a single electron or ion entering the detector is a peak of typically about one millivolt on the oscilloscope.

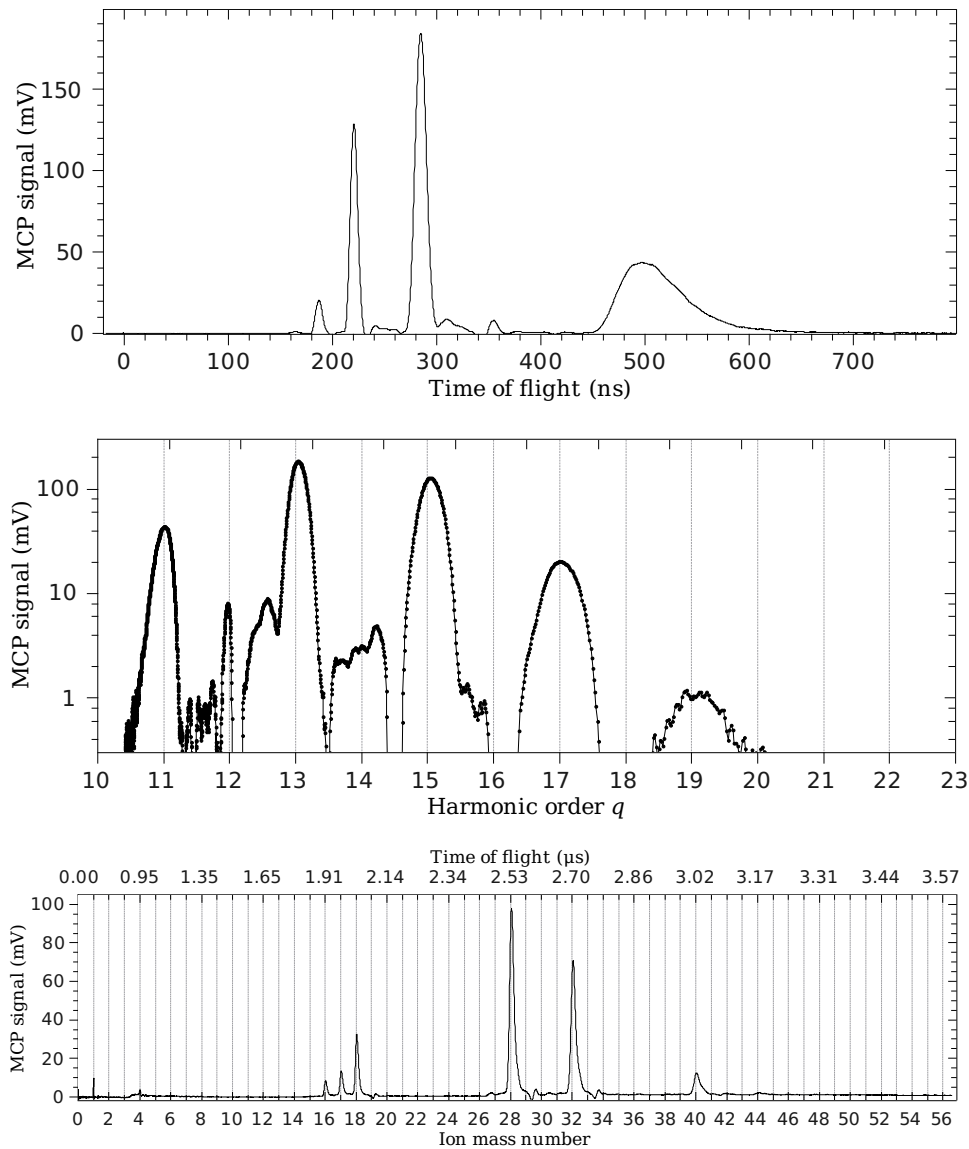


Figure 2.11: Time-of-flight spectra

The top two panels show a photoelectron-energy spectrum from argon ionized by the harmonics generated by the IR laser in the first gas jet. The photoelectrons from the harmonic orders 11, 13, 15, 17, and 19 are clearly visible at positions 474 ns, 273 ns, 211 ns, 178 ns, and 157 ns, respectively. Here the signal from the 13th and 15th harmonic are saturated on the oscilloscope in order to resolve the weaker 19th. The bottom panel shows a typical ion-mass spectrum. The ionized background gases oxygen (O_2^+), nitrogen (N_2^+), argon (Ar^+), water (H_2O^+), and its fragments (HO^+ , H^+ and O^+) are visible together with a small peak from helium (He^+). The middle and bottom panels have their time-of-flight axes scaled for equidistant energy and mass, respectively.

Chapter 3

Results

Two of the most common attosecond pulse metrology methods were applied and compared in the course of this thesis: *reconstruction of attosecond beating by interference of two-photon transitions* (RABITT) as an example of a cross-correlation technique with the *second-order intensity volume-autocorrelation* (2IVAC). Section 3.1 presents the experimental findings, their interpretation, and their implications on the applicability and reliability of these and other metrology methods.

Related to that, the next Section 3.2 investigates the interplay of the two electron trajectories relevant for the generation of high harmonic generation in gases (HHGG). The observations reveal the fallacy of a general assumption about the phase-matching conditions for attosecond pulse trains from HHGG, which has crucial impact on cross-correlation-based attosecond metrology methods as well as on atomic-molecular tomography and precision measurements with extreme ultraviolet (XUV) frequency combs.

The last Section 3.3 provides an example for the applicability of the wave-front-splitting setup for time-resolved measurements of molecular dynamics. Examining the photo-dissociation of ethylene and oxygen reveals the characteristic times involved in the process.

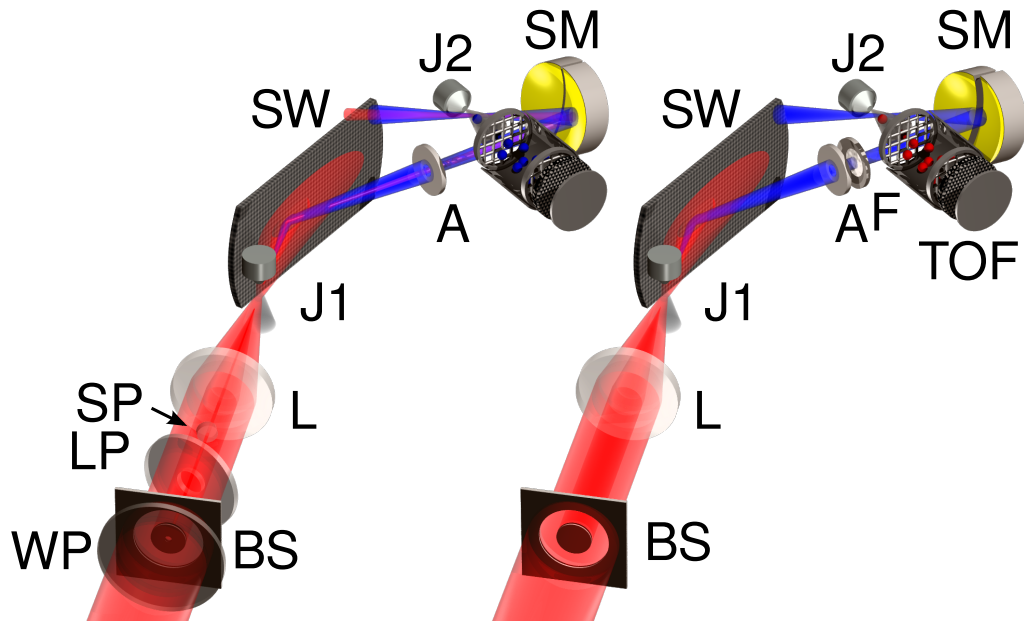


Figure 3.1: Schematic of the two setups used for the attosecond metrology measurements

The left side illustrates the setup used for the RABITT measurements and the right side shows the setup used for the 2IVAC. A half-wave plate (WP) can be inserted to rotate the polarization of the laser (red beam) by a small angle. The beam-shaper (BS) gives the laser an annular shape, in the case of the RABITT setup it has a hole in the center for the dressing beam. A small glass plate (SP) and a large one (LP) with a hole in the center can be used to add a delay between the central dressing beam and the annular part. The lens (L) focuses the laser at the first gas jet (J1) where the harmonics (blue beam) are produced. The silicon wafer (SW) suppresses the infrared (IR) and reflects the XUV. The aperture (A) of $d_A = 3$ mm diameter blocks the residual IR and lets the central XUV pass together with the dressing beam if it exists. A filter (F) can be inserted to select a specific spectrum. The split spherical mirror (SM) focuses the beam into a second gas jet (J2). The time-of-flight spectrometer (TOF) can detect either ions (red balls) or electrons (blue balls).

3.1 Comparison of attosecond metrology methods

As introduced in the overview Chapter 1, a number of different attosecond metrology tools have been developed and some have been applied up to now.

These methods are mostly either based on a cross-correlation of the XUV attosecond pulses with an infrared (IR) dressing laser field, or based on an autocorrelation (AC) of the XUV radiation alone. The cross-correlation approach is more favorable for moderate intensity XUV radiation, since the AC approach depends on high-intensity XUV radiation in order to observe the two-photon ionization, which serves as the non-linear process. Two of the most widely applied methods, one of each approach, are compared here: The RABITT, as shown in Section 1.3, is exemplary for the basic principle of cross-correlation methods, that is the extraction of phase information from the photoelectron wave packets generated by the XUV and IR radiation together. The 2IVAC is the autocorrelation method which also the *photoelectron analysis with non-resonant two-photon-ionization for harmonic electric-field reconstruction* (PANTHER) is based on. 2IVAC and RABITT are the two methods underlying most of the established characterization techniques for attosecond pulses. Nevertheless, a direct comparison between them has been missing. The central task of this thesis is to fill this gap and examine closely the capabilities and limitations of these two methods.

3.1.1 Second-order intensity volume-autocorrelation

A 2IVAC of the harmonics generated in the xenon gas jet as described in Section 2.2.2 was taken with the setup depicted in Figure 3.1 with helium ions as a nonlinear detector. An indium foil (F) of 150 nm thickness selects the harmonics 9–15 and suppresses the 17th and higher harmonics in order to avoid a single-photon ionization of the helium atoms. The normalized relative amplitudes of the harmonics 9, 11, 13, and 15 were measured to be 100%, 40% ,30% , and 25%, respectively, after reflection from the split spherical gold mirror.

Three autocorrelation traces were taken at the three different positions of the focusing lens (L) indicated in Figure 2.6. One with the focus at position $z_B = -0.86z_R$ before the xenon gas jet (J1), one with the focus at position $z_I = 0$ inside the jet, and one at position $z_A = +0.56z_R$ focusing after the gas jet. The length of the Rayleigh range of the focus is $z_R = 88 \pm 5$ mm.

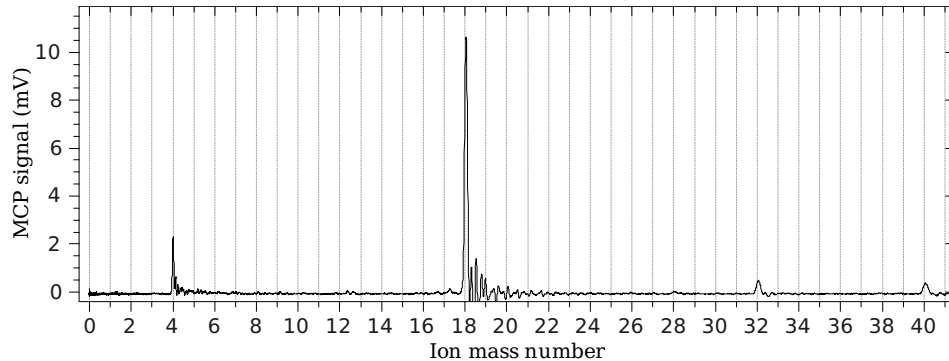


Figure 3.2: Helium ion-mass spectrum

The recorded ion-mass spectrum shows peaks from the singly ionized target gas helium (He^+) at position 4, as well as a strong peak from the background gas water (H_2O^+) at position 18 and small peaks from other background gases like nitrogen (N_2^+), oxygen (O_2^+) and argon (Ar^+) at positions 28, 32, and 40, respectively.

Only if the focus of the driving laser is before the harmonics generating gas jet at z_B , then the 2IVAC trace in Figure 3.1.1 shows clear and regular oscillations with peaks twice per laser period T_L . The solid line in the top panel of Figure 3.3 shows a best fit to the data for a series of Gaussian peaks with a fixed spacing of half a laser period and a peak-to-baseline ratio of 1.6. The width of the fit Gaussians determines the average pulse duration of the pulses inside the train to $\tau_{\text{XUV}} = 660 \pm 50$ as. The traces recorded with the IR driving laser focused inside or after the gas jet show merely random fluctuations and no regular structure.

This is the expected behavior.¹ Theory predicts that the phase-matching inside the production gas medium favors the emission of harmonics from the *short* electron trajectory if the harmonic production in the gas medium happens almost a Rayleigh length z_R after the focus of the driving laser. In this case the contribution of the *long* trajectory is supposed to be negligible. In the other cases, when focusing inside or after the gas jet, the phase-matching conditions for the *short* trajectory are predicted to be worse and

¹Antoine *et al.* (1996); Gaarde and Schafer (2002)

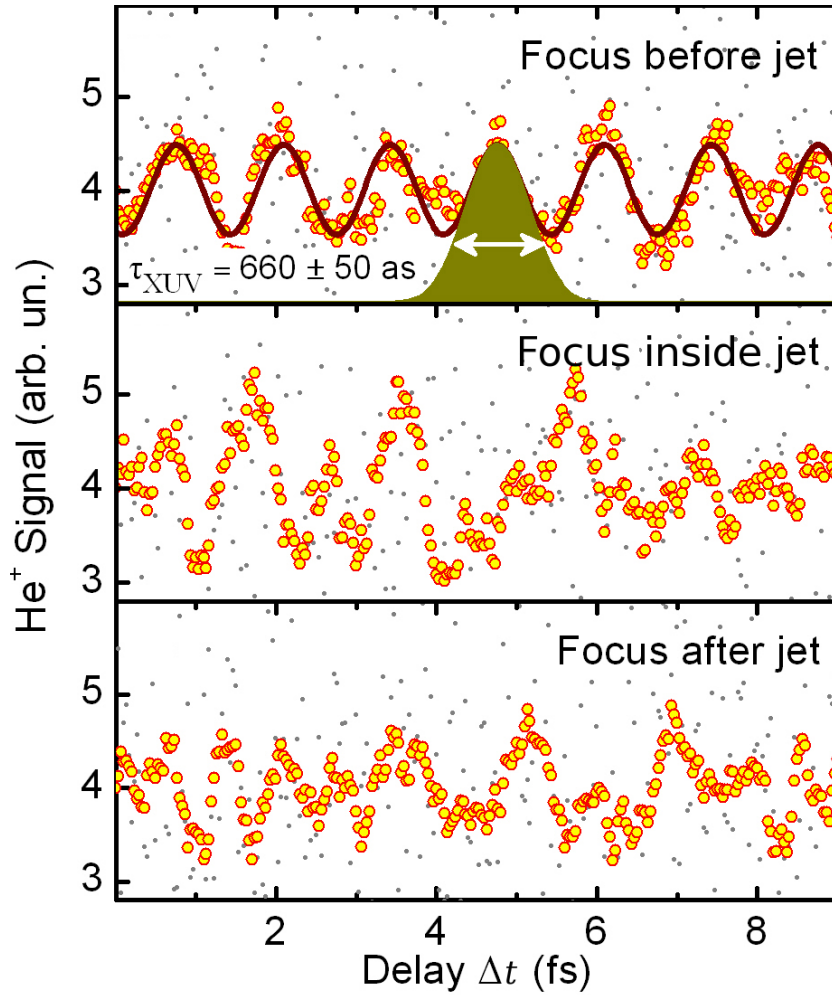


Figure 3.3: Measured 2IVAC traces

Recording the time-of-flight spectrometer (TOF) signal $S_{\text{He}^+}(\Delta t)$ of the helium ions as a function of the delay between the two replicas results in the displayed 2IVAC traces. The top panel shows the attosecond beating obtained when focusing before the harmonics generating gas jet (z_B), the center panel when focusing inside (z_I), and the bottom panel when focusing after the jet (z_A). The gray dots correspond to the measured data points. The yellow-filled red circles are a running average over 10 data points. The purple line is the sum of 12 Gaussian pulses fit to the raw data points. The green area corresponds to one of the fit Gaussian pulses.

emission from the *long* trajectory comes into play. Then the attosecond pulses from the superposition of harmonics are not well confined, since the phases ϕ_q^ℓ of the emitted harmonics from the *long* trajectory are more sensitive to the intensity variations $\dot{I}_L(t, r, z)$ of the driving laser field. Another drawback is that the harmonics from the *long* trajectory are emitted at different times t_e^ℓ compared to those t_e^s from the *short*, which leads to additional phase mismatch in the superposition, if both trajectories contribute.

3.1.2 Reconstruction of attosecond beating by interference of two-photon transitions

Probably the most striking results presented in this thesis are the RABITT traces obtained at the three different focusing positions before z_B , inside z_I , and after z_A the first gas jet (J1), as defined in Figure 2.6. For the cross-correlation between the infrared and the harmonic radiation, a setup very similar to the one applied by Paul *et al.* (2001) is used with the beam shaper (BS) shown in Figure 3.1 having a hole in the center to form the small central dressing beam. The intensity of the IR dressing beam can be adjusted by rotating a $\lambda/2$ half-wave plate (WP) placed before the beam shaper (BS) by a small angle. Two plates provide the delay Δt between the central IR dressing beam and the XUV. One large plate (LP) with a hole in the center delays the annular IR driving laser field and one small plate (SP) delays the central dressing beam. Rotating the central plate (SP) by a small angle changes the delay between the central and the annular part of the IR and thus the delay Δt between the dressing IR and the XUV produced from the annular beam.

Figure 3.4 shows the set of photoelectron-energy spectra of argon ionized by the superposition of the dressing IR beam and the harmonics taken while scanning the delay Δt to obtain the RABITT traces. The results of the RABITT measurements shown in Figure 3.5 imply almost Fourier-transform limited (FTL) attosecond pulses of $\tau_{XUV} \approx 390$ as, even when focusing the IR beam inside the harmonics generating gas jet. Adjusting the phases ϕ_q of the harmonics extracted from the RABITT measurement according to the

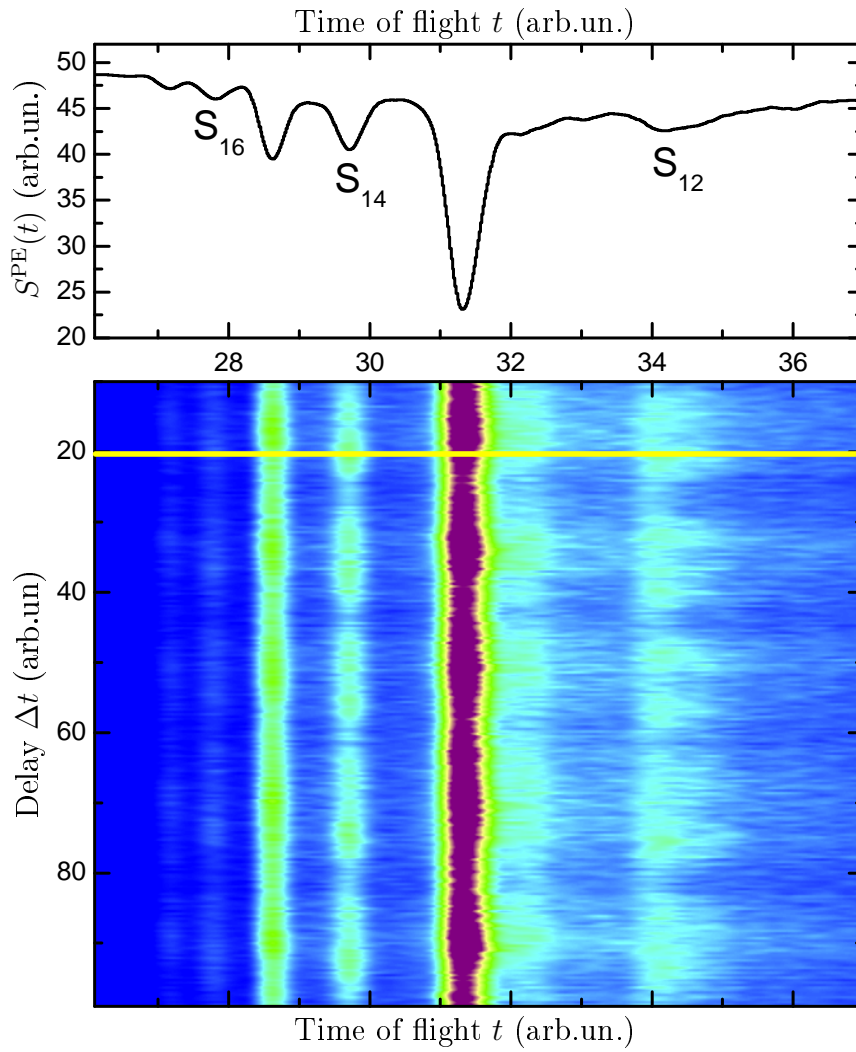


Figure 3.4: Measured time-of-flight photoelectron spectra with side bands

The photoelectron energy-spectra $S^{\text{PE}}(t)$ of argon ionized in the presence of both the XUV harmonics and the fundamental IR show the *side bands* S_{12} , S_{16} , and S_{18} , appearing centered between the odd harmonics. The color-plot in the bottom panel shows the time-of-flight spectra $S^{\text{PE}}(t)$ as a function of the delay Δt . The top panel shows the time-of-flight spectrum at the position of the yellow line.

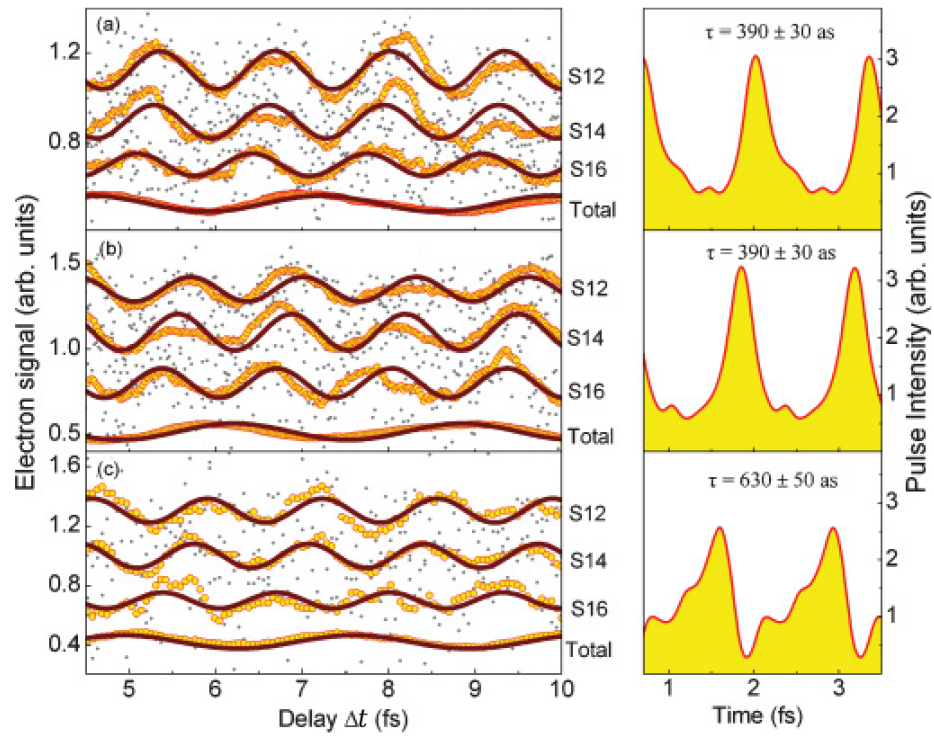


Figure 3.5: Measured RABITT traces and reconstructed attosecond beating

The left panels show the measured photoelectron signal for the *side bands* S_{12} , S_{14} , and S_{16} as a function of the delay Δt between the XUV and the IR taken with the focus at the three positions z_B before the gas jet (a), z_I inside (b), and z_A after the gas jet (c). The gray dots are the measured data points normalized to the corresponding total signal and offset for clarity. The yellow-filled red circles are a running average over 15 data points of each *side band* and over 40 points of the total signal. The purple lines are sinusoidal fits to the data points over 13 oscillations of the *side band* traces and over 6 laser oscillations of the total. The right panels show the attosecond beating reconstructed from the measured intensities I_q and phases ϕ_q of the odd harmonics 9–15 for the respective focus positions.

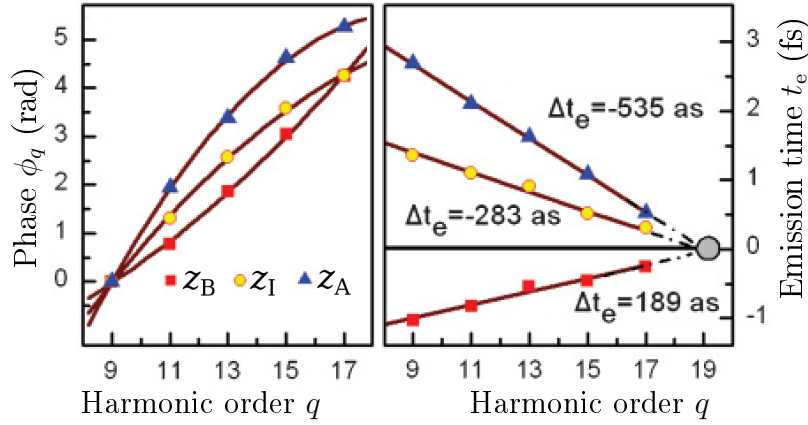


Figure 3.6: Phases of the odd harmonics 9–17 measured with RABITT

The left panel shows the measured phases extracted from the oscillations of the *side bands* S_{12} , S_{14} , and S_{16} at the three focus positions z_B before the gas jet (red squares), z_I inside (yellow circles), and z_A after the gas jet (blue triangles). The right panel shows the corresponding emission times t_e found for the odd harmonics 9–17 assuming that the harmonic 19 is at the *cut-off* (gray circle). It can be seen that the measured chirp of the harmonics changes sign as the focus moves to different positions.

dispersion² of the 150 nm thick indium filter used in the 2IVAC measurement and using the same relative amplitudes for a direct comparison results in the durations τ_{XUV} of the reconstructed pulses of 350 as, 600 as, and 1020 as for the focus positions z_B before, z_I inside, and z_A after the xenon gas jet, respectively.

This is in contradiction to both theoretical predictions and the 2IVAC results shown above, where attosecond confinement was observed only for the focus position before the jet. An explanation for this behavior is the presence of both electron trajectories, the *long* as well as the *short* trajectory, producing the harmonic radiation. As verified also later in Section 3.2, the long trajectory is not fully eliminated despite the inserted aperture with diameter of $d_A = 3$ mm, which selects only the central harmonic beam as shown in Figure 2.5. The problem is that RABITT measures an average phase—actually an average phase difference $\langle \Delta\phi_{q+1} \rangle$ between pairs of harmonics.

²Hunter (1964); Koyama *et al.* (1973); Lemonnier *et al.* (1975); Henke *et al.* (1993); López-Martens *et al.* (2005)

This averaging is manifold:

The spatial profile The *short* trajectory emission may be prevalent in the center and *long* trajectory emission prevalent at bigger divergence. Generally, the trajectories may contribute differently at different portions of the beam. The phases ϕ_q^ℓ and ϕ_q^s of all of these contributions are averaged in the final RABITT measurement.

The whole pulse duration The intensity $I_L(t)$ of the infrared driving laser follows its temporal pulse profile. The phases $\phi_q(I_L)$ of the harmonics depend on that intensity. Thus, the phases of the emitted harmonics $\phi_q(t)$ vary throughout the time of harmonic generation. This can be partly mitigated through phase-matching in the medium, but perfect phase-matching can not be achieved in reality. RABITT measures the average phase difference throughout the entire pulse train.

Shot to shot variation No laser source is perfectly stable. The intensity and possibly the focusability of the laser pulse may change from one pulse to another. Hence, the harmonic emission and the respective phases may vary from shot to shot. Since RABITT is not a single shot method and the entire trace is used to extract the phase information, this also plays a role.

In this case, the phases of the harmonics ϕ_q can not be straightforwardly extracted from the phase offsets φ_{q+1} of the *side bands* as given in Equation 1.7. Instead a more complex formalism, including the calculation of the emission times t_e^ℓ and t_e^s of the harmonics, can reveal some information about the relative contributions of the two electron trajectories.

Figure 3.7 shows some calculated RABITT traces. The *side band* signals S_{q+1} are constructed according to Equation 3.1 using the phases of the

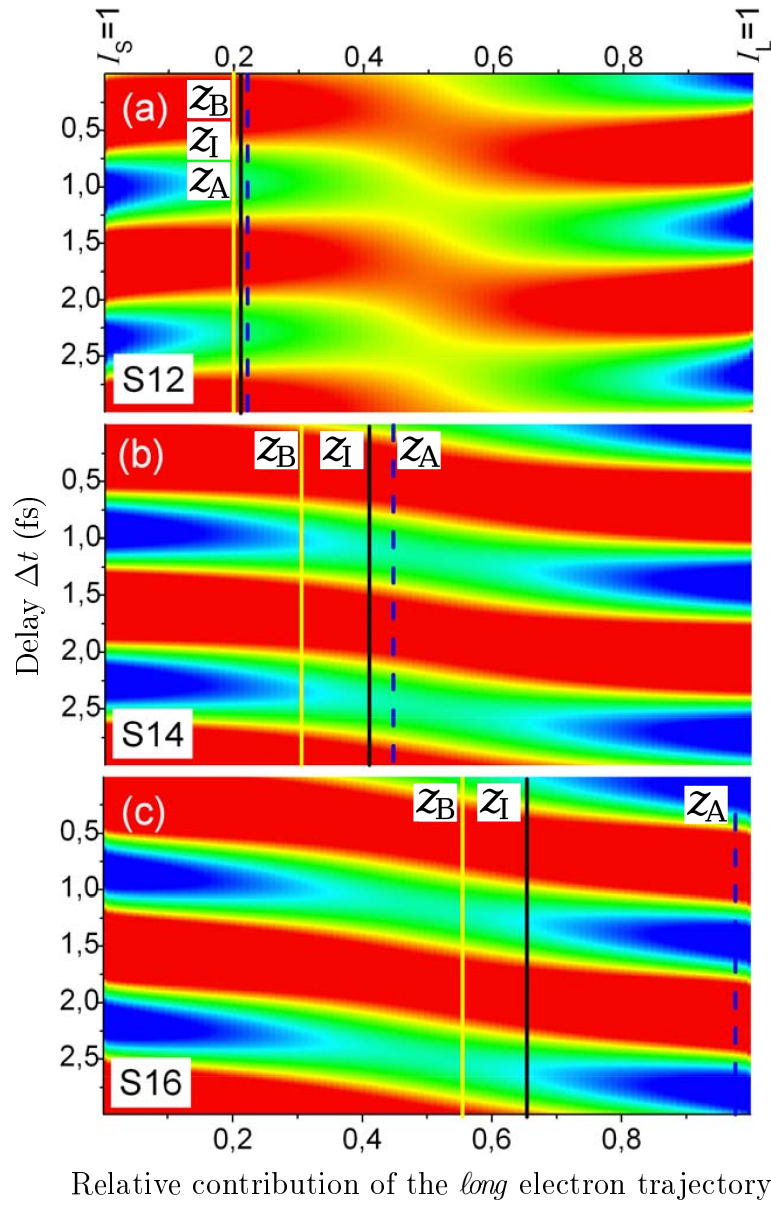


Figure 3.7: Calculated RABITT traces

The color plots show the calculated photoelectron yield as a function of the delay Δt between the XUV and the IR (vertical axis) and depending on the relative contribution of the *long* electron trajectory (horizontal axis). The top, middle, and bottom panels show the signals from the *side bands* S_{12} , S_{14} , and S_{16} , respectively.

harmonics ϕ_q^ℓ and ϕ_q^s calculated using the quantum mechanical model:³

$$\begin{aligned}
S_{q+1}(\Delta t) \propto & \sqrt{I_q^s I_{q+2}^s} \cos(2\omega_L \Delta t + \varphi_{q+1}^s) \\
& + \sqrt{I_q^\ell I_{q+2}^\ell} \cos(2\omega_L \Delta t + \varphi_{q+1}^\ell) \\
& + A_{q+1} \sqrt{\sqrt{I_q^s I_{q+2}^s} \sqrt{I_q^\ell I_{q+2}^\ell}} \cos(2\omega_L \Delta t + \frac{\varphi_{q+1}^s + \varphi_{q+1}^\ell}{2})
\end{aligned} \tag{3.1}$$

Neglecting the very small atomic phase shift $\Delta\phi_{\text{atom}}$ simplifies the phase offset for the *short* trajectory to $\varphi_{q+1}^s = \phi_q^s - \phi_{q+2}^s$ and accordingly to $\varphi_{q+1}^\ell = \phi_q^\ell - \phi_{q+2}^\ell$ for the *long*. The cross-term, which includes the interference between the two trajectories, has an additional amplitude modulation $A_{q+1} = 2 \cos(\frac{1}{2}(\phi_q^s - \phi_q^\ell) + \frac{1}{2}(\phi_{q+2}^s - \phi_{q+2}^\ell))$. It depends on the phase difference between the *long* and the *short* trajectory of the two neighboring harmonics. The intensities of the harmonics generated from the two trajectories are normalized: $I_q^\ell + I_q^s = 1$

Focus position	S_{12}	S_{14}	S_{16}
before z_B	23%	33%	55%
inside z_1	23%	40%	65%
after z_A	23%	45%	95%

Table 3.1: Contribution of the *long* trajectory

Matching the experimental results to calculations reveals the relative *long* electron trajectory contribution for the *side bands* between the harmonic orders 11 to 17. Here the values are to be understood as "mean" values between two neighboring harmonics assuming a smooth variation along the spectrum: $I_q^\ell \sim I_{q+1}^\ell \sim I_{q+2}^\ell$

Matching the measured RABITT traces of all three positions to the calculated data in Figure 3.7 (vertical lines) reveals, that the *short* trajectory prevails when focusing before the gas jet at position z_B . As expected from theory, the *long* trajectory gains importance as the focus shifts downstream. The extracted ratios for the *long* trajectory are displayed in Table 3.1. These values are sensitive to the driving laser intensity used for the calculations. The accuracy of the ratios depend on the accuracy at which the intensity of the driving laser is known.

³Lewenstein *et al.* (1994)

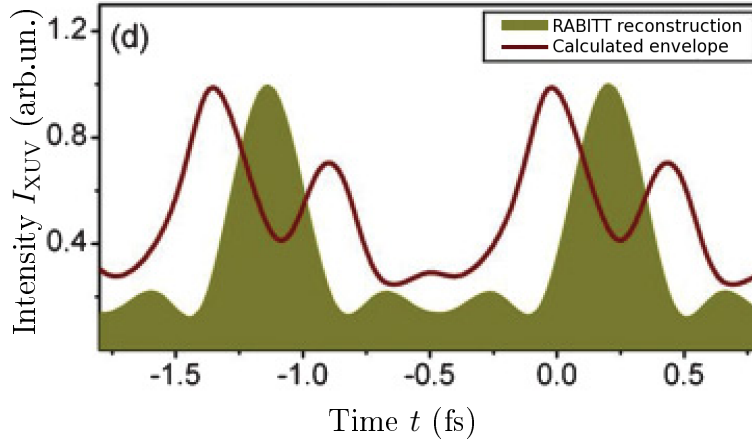


Figure 3.8: Comparing a RABITT reconstruction to an averaged pulse train
 The line shows the averaged calculated wave form of a superposition of the odd harmonics 9–17 with equal amplitudes, for driving laser intensities varying 15% around $6 \times 10^{13} \text{ W/cm}^2$ with equal contributions of both electron trajectories. The filled area shows the wave form reconstructed from what RABITT would measure for the same averaged superposition.

Figure 3.8 illustrates the effect of measuring with RABITT the average phase differences $\langle \Delta \phi_{q+1} \rangle$. The line shows two "wagons" of a calculated attosecond pulse train. It is a superposition of the odd harmonics 9–17 with equal amplitudes and with phases ϕ_q^ℓ and ϕ_q^s according to the quantum mechanical model, assuming equal contributions from both electron trajectories ($I_q^\ell = I_q^s$). The laser intensity I_L at the generation focus was varied $\pm 7.5\%$ around $6 \times 10^{13} \text{ W/cm}^2$ and the resulting wave forms were averaged to simulate the pulse-to-pulse and spatio-temporal variations. The filled area of Figure 3.8 corresponds to the reconstruction, which RABITT would result in for the same averaged superposition. The difference between the two wave forms is striking. It is clear, that in this case RABITT leads to an entirely incorrect wave form and thus can not reveal the correct pulse duration.

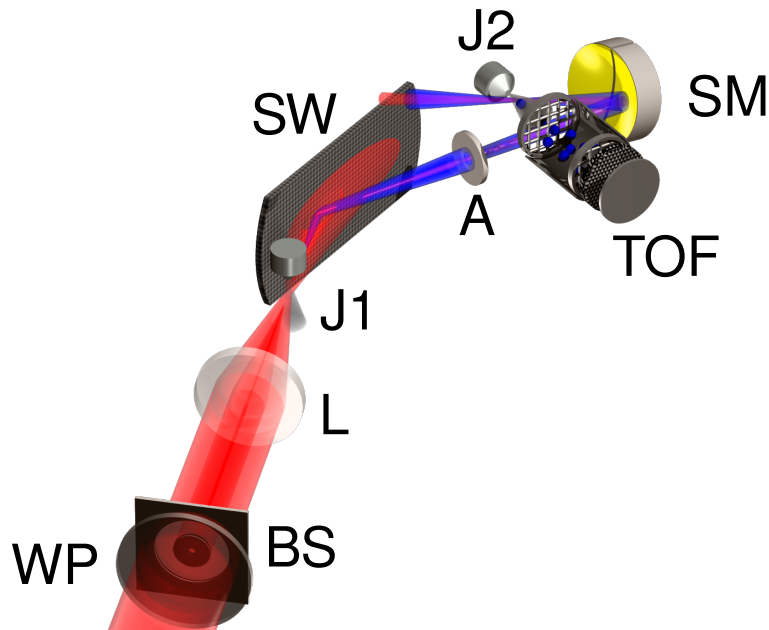


Figure 3.9: Schematic of the setup for the measurement of the quantum-interference between the electron trajectories

The half-wave plate (WP) rotates the polarization of the laser (red beam) by a small angle. The beam shaper (BS) with a hole in the middle gives the IR beam an annular shape with a small additional dressing beam in the center. A lens (L) focuses the laser at the xenon gas jet (J1). The silicon wafer (SW) suppresses the fundamental IR and reflects the XUV harmonics (blue beam). A very small aperture (A) of $d_A = 2$ mm diameter blocks the residual annular IR and lets only the most central part of the harmonic radiation and the IR dressing beam pass. One side of the split mirror (SM) focuses the harmonics together with the dressing beam into the second gas jet (J2) of argon. The time-of-flight spectrometer (TOF) records the photoelectron spectrum.

3.2 Quantum-interference between the *short* and the *long* electron trajectory

In the quantum mechanical process of high harmonic generation it is not actually being measured, which trajectory the electron wave packet follows. Therefore, the probability for an electron to recollide with the parent ion and to emit the harmonic radiation is the coherent superposition of the amplitudes of all possible electron wave packets recolliding with their parent ion.

In the saddle point approximation, only two of these play a significant role: The electron tunnels away from the atom, follows either the *short* trajectory and recollides or it follows the *long* trajectory and recollides. The phase ϕ_e of the electron, accumulated during the excursion of the electron separated from the parent ion, is not generally the same for the two trajectories. Both ϕ_e^s and ϕ_e^ℓ depend on the intensity I_L of the driving laser, but the dependencies are different:

$$\frac{\partial \phi_e^s}{\partial I_L} \neq \frac{\partial \phi_e^\ell}{\partial I_L}$$

This may result in a situation, where the electrons following either trajectory, end up with the same phase and interfere constructively $\phi_e^s = \phi_e^\ell$ or in another case with opposite phase, in which case their wave functions interfere destructively. Eventually, the phase difference between the two trajectories is approximately proportional to the laser intensity multiplied with the difference in flight times (see also Equation 1.5):

$$\Delta\phi_e(I_L) = \phi_e^\ell(I_L) - \phi_e^s(I_L) \sim I_L \cdot (\tau_\ell - \tau_s) = I_L \cdot \Delta\tau \quad (3.2)$$

As can be seen in Figure 3.10, the slope $\frac{\partial}{\partial I_L} \Delta\phi_e$ of the phase difference increases with intensity I_L and is higher for lower harmonic orders q .

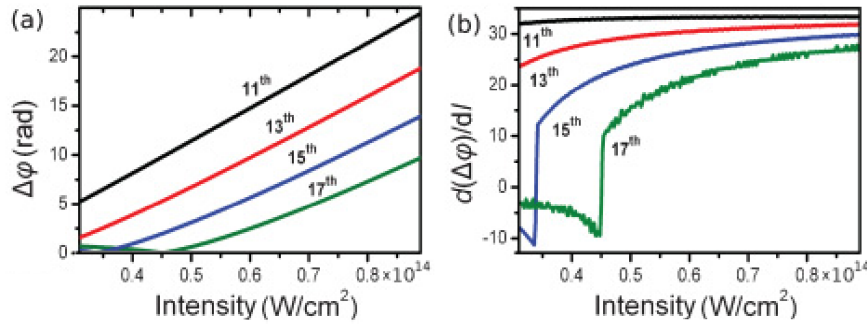


Figure 3.10: Calculated phase difference between the two electron trajectories

The phase difference $\Delta\phi_e(I_L)$ between the *short* and the *long* electron trajectory shown in the left panel depends on the intensity I_L of the driving laser field and it is different for each harmonic q . The right panel shows the derivative $\frac{\partial}{\partial I_L} \Delta\phi_e$ of the phase difference with intensity.

The probability $\mathcal{P} = |\Psi_{\text{emit}}|^2$ of recollision and emission of harmonic radiation

emerges from a coherent superposition of both quantum states $\Psi_s = \psi_s e^{i\phi_e^s}$ and $\Psi_\ell = \psi_\ell e^{i\phi_e^\ell}$. It is therefore an oscillating function of the driving laser intensity I_L .

$$\begin{aligned} |\Psi_{\text{emit}}(I_L)|^2 &\propto \left(\psi_s e^{i\phi_e^s} + \psi_\ell e^{i\phi_e^\ell} \right) \times (\text{complex conjugate}) \\ &\propto \underbrace{\psi_s^2 + \psi_\ell^2}_{\text{steady increase}} + \underbrace{2\psi_s \psi_\ell \cos \Delta\phi_e(I_L)}_{\text{oscillating term}} \end{aligned} \quad (3.3)$$

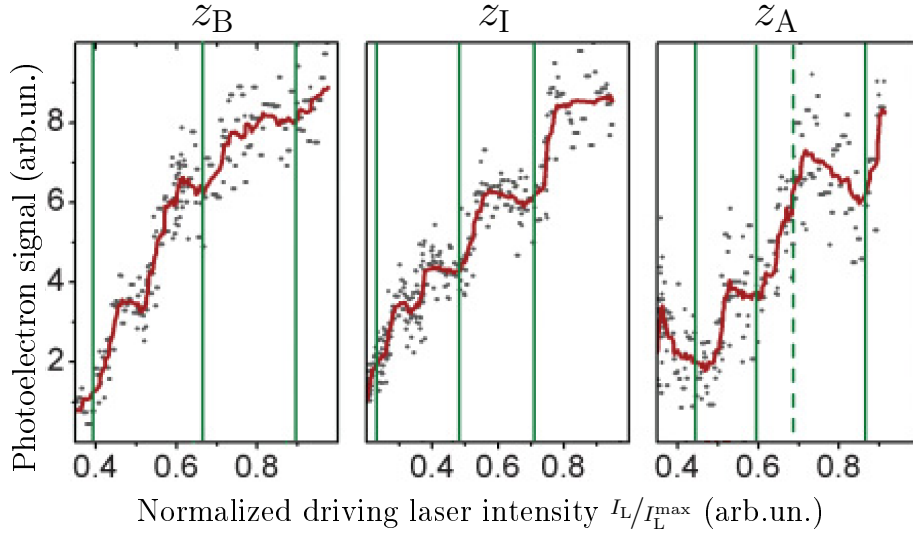


Figure 3.11: Interference between the two electron trajectories

The photoelectron signal S_{13} from argon ionized by the 13th harmonic in dependence of the driving laser intensity I_L shows the interference pattern observed as oscillations on top of the *steady increase* of the harmonic yield.

This was measured by observing the photoelectron signal of the harmonics $S_q(E_L)$ in dependence of the pulse energy E_L of the driving laser with a setup illustrated in Figure 3.9. The intensity I_L of the driving laser at the interaction region was scanned around $4 \times 10^{13} \text{ W/cm}^2 \lesssim I_L \lesssim 1 \times 10^{14} \text{ W/cm}^2$. Since the driving laser pulse has a spatio-temporal envelope, the interference cannot be expected to be of maximum contrast. This is because the laser intensity I_L varies with the distance from the optical axis (r) and along the focus (z) and so the phase difference $\Delta\phi_e(I_L)$ varies in the different regions of the argon gas jet (AJ). This means partially constructive and partially destructive interfer-

ence in different parts of the interaction volume, but the phase-matching in the dominant part results in the interference pattern shown in Figure 3.11. As the driving laser intensity I_L rises, the probability of harmonic emission increases for both possible electron trajectories and on top this *steady increase* of Equation 3.3 are the oscillations from the quantum-interfering electron trajectories (QIET). These oscillations of $S_q(E_L)$ reveal, that the *short* and the *long* electron trajectory are both present at all three phase-matching conditions, which are focusing before the harmonics generating gas jet (z_B), inside (z_I) and after the jet (z_A).

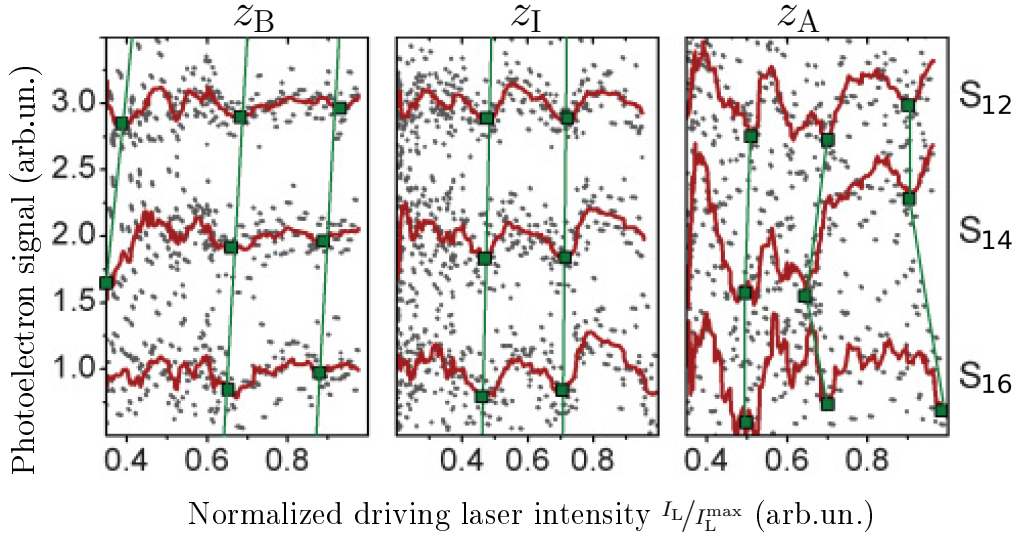


Figure 3.12: XUV±IR interference between the two electron trajectories
The two-photon (XUV±IR) photoelectron signals of the *side bands* S_{12} , S_{14} , and S_{16} from argon ionized by the harmonics together with the IR in dependence of the driving laser intensity I_L . The *steady increase* was removed from the data.

$$\begin{aligned}
S_{q+1} \propto & \cos(2\omega_L \Delta t + \varphi_{q+1}^s) + \cos(2\omega_L \Delta t + \varphi_{q+1}^\ell) \\
& + \cos\left(2\omega_L \Delta t + \frac{\varphi_{q+1}^s + \varphi_{q+1}^\ell}{2}\right) \cdot 2 \cos\left(\frac{\varphi_q^s + \varphi_q^\ell}{2} + \frac{\varphi_{q+2}^s + \varphi_{q+2}^\ell}{2}\right) \\
& + \cos(\varphi_q^s - \varphi_q^\ell) + \cos(\varphi_q^s - \varphi_q^\ell)
\end{aligned} \tag{3.4}$$

Also the *side bands* $S_{12}(E_L)$, $S_{14}(E_L)$, and $S_{16}(E_L)$ could be observed as a function of the driving laser pulse energy, because of the RABITT-like setup used with the small central IR dressing beam. Taking a closer look at their oscillations shown in Figure 3.12 and also at the main peaks' oscillations after removal of the *steady increase* reveals some interesting features. They conform to the expected behavior found by the calculations shown in Figure 3.13, which are based Equation 3.4 with the phases calculated by the numerical simulation of the single-atom response with equal contribution of both electron trajectories. The *steady increase* was not included in the calculation.

- a) The signals show a characteristic structure with double-peak interference maxima spaced apart by about $0.23 \times I_L^{\max}$, which is in good agreement with the previously reported value⁴ of $0.3 \times 10^{14} \text{ W/cm}^2$.
- b) The distance between the interference minima (green lines in Figures 3.11 and 3.12) becomes smaller for higher laser intensity. This is in accordance to the increase of the derivative $\frac{\partial}{\partial I_L} \Delta\phi_e$ as shown in Figure 3.10. This behavior could not be clearly observed when focusing after the gas jet at z_A , where the double-minima structure is not clearly visible.
- c) The fringe contrast of the observed oscillations increases from about 10% when focusing before the gas jet at z_B to about 25% when focusing after the gas jet at z_A . This can be explained by the increased contribution of the *long* electron trajectory when focusing later downstream, as mentioned earlier in Table 3.1 in the previous section. The calculations base on an equal contribution of both trajectories.
- d) The positions of the interference minima shift to lower laser intensities as the order of the *side band* increases. This is illustrated by the slanted green lines in Figure 3.12 and by the blue lines in Figure 3.13.
- e) Even the *side band* involving harmonics close to the *cut-off* shows oscillations. This is in agreement with the simulations of the single atom

⁴Zair *et al.* (2008); Auguste *et al.* (2009)

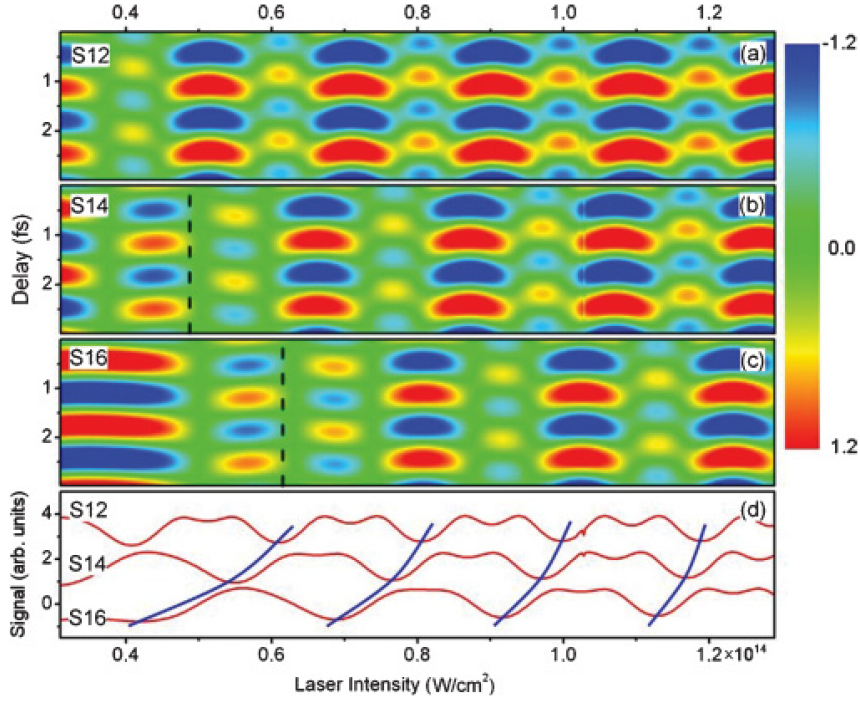


Figure 3.13: Calculated *side band* signal in dependence on the laser intensity
The calculated two-photon (XUV \pm IR) photoelectron signals of the *side band* based on the phases ϕ_q^s and ϕ_q^ℓ of the harmonics deduced from the simulation of the single atom response. The color plots (a, b, and c) in the top panel show the *side band* signal as a function of the laser intensity I_L and the delay Δt between the harmonics and the IR for the *side bands* S_{12} , S_{14} , and S_{16} , respectively. The bottom panel (d) shows a line out for all three *side bands* corresponding to zero delay.

response, where both trajectories contribute to the emission. Merely the difference in flight time $\Delta\tau = \tau_\ell - \tau_s$ is shorter when the harmonics are in the *cut-off* region, which results in a more slowly varying phase difference $\Delta\phi_e \sim I_L \Delta\tau$ as shown in Equation 3.2 and in the longer oscillation periods visible in Figure 3.13 for highest *side bands* and the lowest laser intensities.

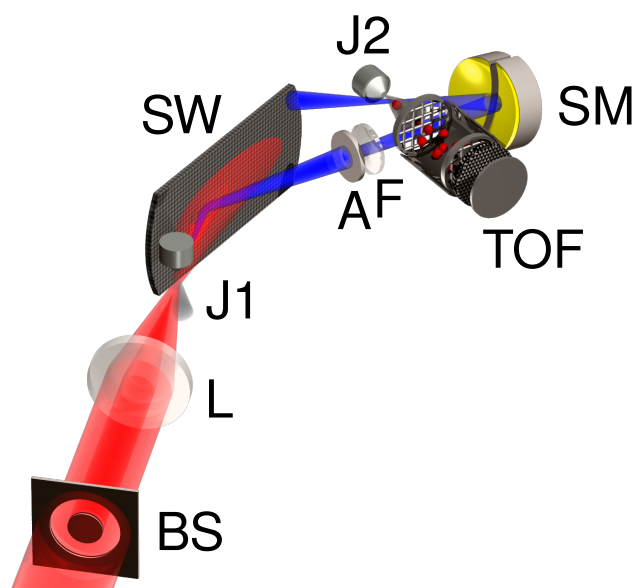


Figure 3.14: Schematic of the setup to study molecular dynamics

The beam-shaper (BS) gives the IR laser (red beam) an annular shape. The lens (L) focuses the laser at the first gas jet (J1) where the harmonics (blue beam) are produced. The silicon wafer (SW) suppresses the IR and reflects the harmonics. The aperture (A) blocks the residual annular IR and lets the central harmonics pass. An MgF_2 filter (F) selects the 5th harmonic and suppresses higher orders. The split spherical mirror (SM) focuses the beam into a second gas jet (J2) with a mixture of gases. The time-of-flight spectrometer (TOF) detects the ions (red balls).

3.3 Molecular dissociation dynamics

This section demonstrates the feasibility of studying molecular dynamics by using the wave front splitting device introduced in Section 2.3.1 to conduct time-resolved vacuum ultraviolet (VUV) two-photon ionization measurements. With a time-resolved technique, it is possible to trace the sequence of quantum states, which an excited molecule passes through on the way to the ground state. All the relevant times of the decay can be extracted from the measured ionization signals. This presents an opportunity for application of the emerging intense XUV attosecond laser sources in all the fields of study, from atoms and molecules to condensed matter.

Many materials strongly absorb vacuum ultraviolet radiation, hence the name, as it propagates in vacuum only. A VUV photon can excite a rapidly

evolving quantum state of various atoms, molecules, or matter. The dynamics of such a quantum state can be probed with a second VUV photon by the interaction of the photon with the molecule shortly after the excitation by the first. Thus, ultra-short femtosecond or even attosecond pulses provide an ideal tool to study these quickly altering quantum states. If used in a *pump-probe* manner, that is applying two pulses with adjustable delay, the second pulse can take a snapshot of the evolving system at a given time defined by the delay. Most of the recent investigations of ultra-fast evolving quantum systems⁵ have used infrared radiation as the time delayed probe. Such an asymmetric pump-probe setup at often substantially high IR intensities may lead to a perturbation of the system. This can introduce intermediate quantum states which may complicate the interpretation of the measured data. The recent progress in the research fields of intense VUV and XUV pulsed laser sources with few-femtosecond or even sub-femtosecond pulse duration⁶ has rendered single-color time-resolved solutions possible even at ultra-short pulse duration.

For the presented time-resolved measurements a 5 mm thick magnesium fluoride MgF_2 plate, placed at the position of the filter (F) as shown in Figure 3.3, selects the fifth harmonic and blocks higher orders in order to avoid single-photon ionization from the ground state of the gases used in the second jet (J2). The dispersion of the MgF_2 filter made it necessary to add a considerable chirp to the harmonics generating laser pulse in order to achieve the shortest possible duration τ_5 for the fifth harmonic after the filter (see also Figure 2.10). The second gas jet (J2) in the detection area consists of a mixture of gases, either ethylene and krypton or oxygen and krypton. Since the two VUV pulses are identical, the recorded ion signals as a function of the delay Δt between the two pulses are symmetric: $S(\Delta t) = S(-\Delta t)$. In the case of a non-resonant direct two-photon ionization, the trace of the ion signal $S(\Delta t)$ becomes a second-order volume-autocorrelation as described in Section 1.3. If the spatio-temporal resolution is good enough to allow for an

⁵Drescher *et al.* (2002); Cavalieri *et al.* (2007); Uiberacker *et al.* (2007)

⁶Charalambidis *et al.* (2008); Nomura *et al.* (2009); Skantzakis *et al.* (2010); Tzallas *et al.* (2011)

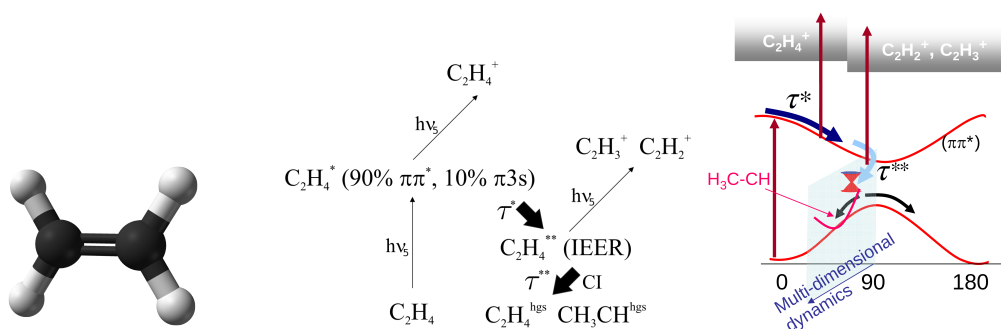


Figure 3.15: Ethylene molecular structure and photo-reaction path

The molecular configuration of ethylene in the ground state is shown on the left. The diagrams in the middle and on the right illustrate the sequence of states, which the ethylene molecule passes through.

interferometric autocorrelation, then the trace can disclose the dynamics of the driven wave packet.⁷ In the case of a resonant or near-resonant intermediate state, information on the temporal dynamics of the intermediate state can be extracted from the trace even if the resolution is not good enough to resolve the interference pattern. In principle, the deconvolution of the measured trace reveals both the laser pulse duration and the characteristic times of the investigated system. Anyhow, an independently measured pulse duration yields more accurate results.

3.3.1 Ethylene

The simple structure of the C_2H_4 ethylene molecule displayed in Figure 3.15 makes it a suitable target for studying the central $C=C$ carbon double bond. There has been much research⁸ on the photo-chemical behavior of ethylene for some time, but still many questions remain open regarding processes in the VUV.

A fifth harmonic photon γ_5 with an energy of $E^\gamma = 7.75\text{ eV}$ excites the ethylene molecule to a superposition of the $\pi\pi^*$ valence state and the $\pi 3s$ Rydberg state. The population of the $\pi 3s$ is only about 10%, so its influ-

⁷Peralta Conde *et al.* (2009b)

⁸Foo and Innes (1974); Peralta Conde *et al.* (2009a) and references therein

ence on the dissociation is neglected here and the further evolution of the $\pi\pi^*$ state can be understood according to a model similar to the one described by Kosma *et al.* (2008). Absorption of a second photon γ_5 by the excited C_2H_4^* leads to ionization (C_2H_4^+). If left to evolve, the excited molecule undergoes an elongation and torsion of the central carbon bond. A torsion angle close to 90° leads to an intermediate electronically excited region (IEER) governed by multidimensional quantum dynamics. The $\text{C}_2\text{H}_4^{**}$ in the IEER is of lower energy⁹ and from here the absorption of a second photon γ_5 leads to fragmentation of the molecule, so that only CH_2^+ and CH_3^+ are observed. From this IEER the molecule can go through a conical intersection (CI) to reach a hot ground state of either $\text{H}_2\text{C}=\text{CH}_2^{\text{hgs}}$ ethylene or the $\text{HC}:-\text{CH}_3^{\text{hgs}}$ ethylidene radical. From this point onwards the characteristic times are of the order of picoseconds. In this context two characteristic times shall be investigated:

τ^* The time while the excited molecule C_2H_4^* resides in the Franck-Condon region before it reaches the IEER.

τ^{**} The duration that the molecule $\text{C}_2\text{H}_4^{**}$ in the IEER needs to reach the CI to a hot ground state.

All time-of-flight spectrometer (TOF) signals shown in Figure 3.16 were recorded simultaneously: The signal of ethylene ions $S_{\text{C}_2\text{H}_4^+}(\Delta t)$ and the ionized fragments $S_{\text{C}_2\text{H}_3^+}(\Delta t)$ and $S_{\text{C}_2\text{H}_2^+}(\Delta t)$ as well as the signal of krypton ions $S_{\text{Kr}^+}(\Delta t)$. A simulation¹⁰ of the 2IVAC, fit to the measured trace of krypton ions, results in a pulse duration of $\tau_5 = 31 \pm 2$ fs. The simulation of the 2IVAC is based on the spatio-temporal distribution of the electromagnetic field at the focus over a volume of 20 times the beam waist diameter w_0 in width and height and over 26 times the Rayleigh range z_R in length assuming a Gaussian pulse of the 5th harmonic.

The characteristic times τ^* and τ^{**} can be inferred from the ion signals of ethylene and its fragments, by integrating the Liouville equation for a three-level system¹¹ spatially and temporally and calculating for each delay step

⁹Foo and Innes (1974)

¹⁰Faucher *et al.* (2009)

¹¹Mestdagh *et al.* (2000); Stert *et al.* (2004)

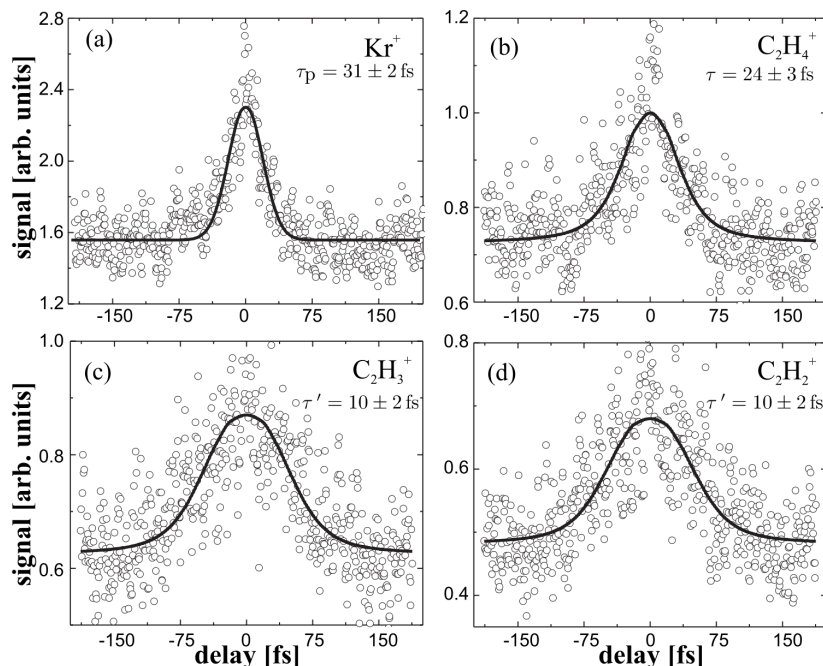


Figure 3.16: TOF ion signals of krypton, ethylene and its fragments

The top left panel (a) shows the signal of singly ionized krypton Kr^+ from the ion-mass spectrometer, the top right panel (b) shows that of singly ionized Ethylene C_2H_4^+ . The bottom panels (c) and (d) show the ions signals of the fragments C_2H_3^+ and C_2H_2^+ , respectively. Circles show the measured data points. The solid lines are the numerical simulation of the three-level system with the characteristic times adjusted to fit the measured data.

Δt the population probabilities of the different levels at every place in the interaction volume. The solid lines in Figure 3.16 are the calculated cycle-averaged ionization probabilities of the excited states by a photon of the 5th harmonic, approximated by the Golden Rule. Depletion of the populations was not taken into account.

Adjusting the characteristic times of the system in the simulation to fit the measured ion signals results in $\tau^* = 24 \pm 3$ fs for the flow out of the Frank-Condon region towards the IEER and in $\tau^{**} = 10 \pm 2$ fs for the time needed to reach the hot ground state through the CI. The width of the traces from the two fragment ions $S_{\text{C}_2\text{H}_3^+}(\Delta t)$ and $S_{\text{C}_2\text{H}_2^+}(\Delta t)$ are the same, since they originate from the same source.

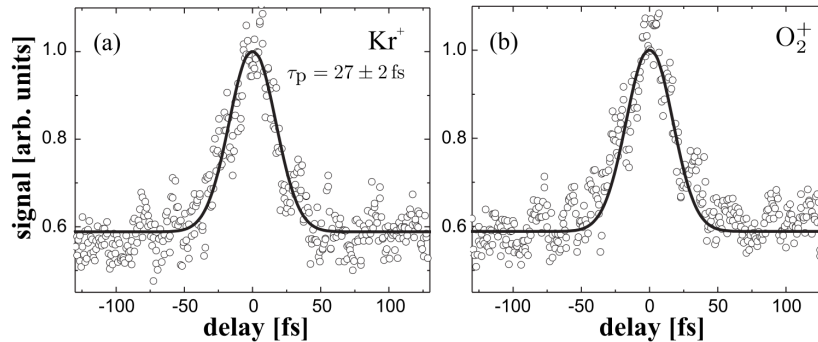


Figure 3.17: TOF ion signals of krypton and oxygen

The left panel (a) shows the signal of singly ionized krypton Kr^+ from the ion-mass spectrometer and the right panel (b) shows that of singly ionized oxygen O^+ . Circles show the measured data points. The solid lines are the simulation of the second-order intensity volume-autocorrelation with the pulse duration adjusted to fit the measured data.

3.3.2 Oxygen

The absorption of the oxygen molecule O_2 in the UV–VUV region at photon energies of $h\nu = 7.0\text{--}9.8$ eV, which is called the Schumann-Runge continuum, is of central importance to environmental issues. It plays a dominant role in the formation of the ozone layer in the stratosphere. O_3 and O_2 are responsible for nearly all of the UV-absorption within the earth’s atmosphere, which is necessary for the life on the earth’s surface.

An absorption of a γ_5 photon of the 5th harmonic excites the oxygen molecule to the $\text{B } ^3\Sigma_u^-$ electronic state.¹² From this state the molecule dissociates into two separate atoms $\text{O} + \text{O}$. Absorption of another γ_5 photon by the electronically excited oxygen $\text{O}_2(\text{B } ^3\Sigma_u^-)$ leads to photo-ionization.

A measurement similar to the one described in the previous section should reveal the characteristic time of the dissociation of the oxygen molecule. Here the second gas jet (J2) is a mixture of krypton and oxygen. The measured ion signals $S_{\text{Kr}^+}(\Delta t)$ and $S_{\text{O}_2^+}(\Delta t)$ are displayed in Figure 3.17. The duration of the 5th harmonic pulse was measured to be $\tau_5 = 27 \pm 2$ fs. The oxygen trace does not show a significant difference in width compared to the krypton

¹²Lin *et al.* (1998)

trace, hence the characteristic time of the dissociation can not be quantified but can be limited to be less than $\tau_{B^3\Sigma_u^-} \lesssim 5$ fs. This divergence from earlier experimental results¹³ may be due to the different probe wavelength used. This affects the time window available for the ionization of the excited oxygen molecule and that actually defines the characteristic time.

¹³Farmanara *et al.* (1999)

Conclusions

The most important results of the presented experiments are reviewed here and their impact on *attoscience* and other fields of study elaborated.

The Section 4.1 will sum up the main points that have emerged from the experimental findings. This includes the attosecond metrology assessment, the investigation on the contributions of different quantum-paths involved in the high harmonic generation (HHG), and also the results from the application of high harmonic radiation to study molecular dynamics utilizing the wave-front-splitter setup.

Finally Section 4.2 dares a look ahead to see what could be coming up on the attosecond frontier. Required future investigations are proposed and possible improvements and refinements as well as new methods are presented and discussed.

4.1 Summary

A volume-autocorrelator was assembled and tested. The second-order interferometric volume-autocorrelation (2iVAC) of the fifth harmonic pulse — generated in a xenon gas jet by an infrared (IR) laser with $\lambda_L = 800$ nm wavelength and $\tau_L = 50$ fs pulse duration — was measured with the wave-front splitter in combination with a krypton gas jet and a time-of-flight spectrometer (TOF). The resolution of the fringing pattern of the 1.87 PHz radiation

indicates a resolution of the volume-autocorrelator of better than $\delta t < 133$ as. This validates the fitness of the split-mirror setup for the following autocorrelation and cross-correlation measurements of attosecond pulses as well as for time-resolved studies of molecular dynamics down to sub-femtosecond time scales.

The comparative study between the two attosecond metrology methods, which are the *reconstruction of attosecond beating by interference of two-photon transitions* (RABITT) and the *second-order intensity volume-autocorrelation* (2IVAC) lead to some important insight concerning their applicability and the general interpretation of their results. A RABITT measurement is always averaged over the entire pulse train, over a number of driving laser pulses needed to record the entire trace at different delay values Δt and usually also over a considerable part of the beam diameter. Due to the nature of the RABITT measurement, which is to measure the phase difference $\langle \Delta\phi \rangle$ between two neighboring odd harmonics, a variation of the laser intensity in time or in space has detrimental consequences for the accuracy of the reconstructed pulse if both electron trajectories contribute to the harmonic emission. This effect is illustrated in Figure 3.8.

The relative weight of the *long* or the *short* electron trajectory depends on the phase-matching conditions in the harmonics generating gas medium. In a real experiment these conditions are not *a priori* known. The interpretation of the data measured by the RABITT method relies therefore on assumptions and simulations of the phase-matching conditions and on the propagation effects in the gas medium. Even if the RABITT measurement indicates a constant phase difference between the contributing consecutive harmonics, this alone does not provide for Fourier-transform limited (FTL) pulses in the attosecond pulse train. Since RABITT measures the harmonics' phases $\langle \phi_q \rangle$ spatio-temporally averaged over a large number of entire pulse trains, it may well be that a positive chirp at one place or time and a negative chirp at another place or time neutralize each other in the final RABITT measurement. Yet they might not compensate for each other in a real application, where both parts of the radiation, the one with positive chirp and the one with negative chirp, lead to undesirable results. This situation naturally

arises if both electron trajectories contribute to the emission of the harmonic radiation, since they do have opposite chirp, as predicted by the numerical simulations based on the quantum-mechanical description of the *three-step model* and as found in the results of the RABITT measurements at different focus positions shown in Figure 3.6.

Also the 2IVAC measures the pulse duration $\langle\tau\rangle$ averaged over the entire pulse train, over a number of driving laser pulses and over the chosen beam cross-section. This however cannot result in an underestimation of the attosecond pulse duration, since that method does not measure phases but directly the impact of the radiation on the atoms. Here the situation is opposite. The absence of a beating pattern in the 2IVAC trace does not necessarily guarantee the absence of attosecond pulses but may be due to a lack of spatial coherence. Theoretically, well confined attosecond bursts in one region and other well confined attosecond bursts in another region of the beam cross-section but with different timing may distort the 2IVAC trace so that no regular beating can be observed. Only temporally well confined and spatially coherent attosecond bursts can result in the measured regular 2IVAC beating as displayed in Figure 3.3. Hence a 2IVAC measurement assesses those beam qualities that are mostly needed for application of the attosecond pulses.

The concurrent presence of both electron trajectories was proven to be the case for a set of three different phase-matching conditions. In all three cases the harmonic yield oscillates with changing laser intensity, which is an indicator for the interference of the *long* and the *short* electron trajectory. This causes severe problems for cross-correlation-based metrology methods, which extract an average phase $\langle\phi_{\text{XUV}}(\omega)\rangle$, such as RABITT. Also other techniques, like atomic-molecular tomography and precision measurements that use extreme ultraviolet (XUV) frequency combs produced by high harmonic generation in gases (HHGG) are effected by the presence of emission from of both trajectories.

The application of high-order harmonic radiation to study the photodissociation of ethylene and oxygen showed the applicability of the split-mirror arrangement for time-resolved measurements on the few-femtosecond

time scale. All the characteristic times throughout the decay of the excited ethylene molecule down to a hot ground state could be extracted from the measured ionization signals. By using a polarization-gating technique¹ to produce isolated attosecond pulses, even sub-femtosecond resolution can be achieved.²

4.2 Outlook

A better understanding and a more reliable predictability and endorsement of the phase-matching and propagation effects under realistic experimental conditions would dramatically improve the value of cross-correlation-like phase-retrieval metrology methods. A real-time combined measurement of different metrology methods can be a suitable way to point out the uncertainty factors and manifest the capabilities of the techniques. This could be for example the *in situ* method and the photoelectron analysis with non-resonant two-photon ionization for harmonic electric-field reconstruction (PANTHER). Another level of insight can also be gained from phase-retrieval metrology of single attosecond pulses if they can be spatially well resolved across the beam cross-section in the far field. Also a single-shot metrology method would help to assess the stability of the attosecond pulse generation and to estimate the impact of averaging.

Table-top titanium-sapphire pulsed laser systems with ever increasing peak intensities are slowly crossing the petawatt border.³ Using these light sources in ultra-loose focusing conditions with focal spot sizes close to a millimeter⁴ is one direction to increase the intensity of the harmonic radiation generated in gas media. Multi-gas-jet or multi-gas-cell HHG setups⁵ present another way to increase the conversion efficiency on the way to stronger XUV radiation. Polarization-gating techniques⁶ can be used to limit the XUV

¹Tzallas *et al.* (2011)

²Skantzakis *et al.* (2010)

³Kiriyama *et al.* (2006)

⁴Hergott *et al.* (2002)

⁵Pirri *et al.* (2008)

⁶Tzallas *et al.* (2011)

emission to a single burst of radiation leading to isolated attosecond pulses. Besides that, the most promising technique for high-efficiency conversion into harmonic radiation is the high harmonic generation from surfaces (HHGS) with tight focusing to reach intensities triggering the relativistic oscillating mirror (ROM) effect. Since there is no saturation expected, but even higher conversion ratios,⁷ this method can most effectively take advantage of the highest laser intensities available.

Having access to stronger harmonic radiation makes autocorrelation approaches more viable especially for polarization-gating techniques where only a fraction of the incident radiation inside the gate is used for the generation of the XUV.

⁷Baeva *et al.* (2006); Nomura *et al.* (2009)

Appendix **A**

A.1 Technical details

Some of the devices used in connection with the different setups described in Chapter 2 were built in-house. The following sections give a short summary on some of the software and hardware designed and developed for the experiments conducted in the course of this thesis.

A.1.1 Control and data acquisition software

In order to control some of the apparatus used in the experiments, I developed a number of software programs written in the graphical programming language National InstrumentsTM LabVIEW[®]. Figure A.1 shows an excerpt of the program to facilitate recording the autocorrelation, cross-correlation, or pump-probe measurements with the split-mirror setup shown in Section 2.3.1. The program connects via a GBIP communication interface to the Tektronix[®] digital phosphor oscilloscope and also via an RS-232 serial port to the *piezosystem jena* controller box, which drives the piezoelectric tilting and translation stages of the split spherical mirror (SM).

The position z_f of the fine translation stage can be adjusted in between the instances of the laser pulses. This way the data acquisition can be synchronized to the 10 Hz repetition rate of the laser system. The recorded time-of-flight spectra can be displayed live on the computer monitor together with five graphs for five different temporal gates defined in the user interface

shown in Figure A.1 While the measurement is running the spectra and the integrals defined by the gates are also saved to the computer's hard drive in real-time into a set of log files. These further allow for the data to be viewed with graphical analysis tools such as Origin[®] or other custom made programs.

A.1.2 Electronics

The experiment control and data acquisition was supported by a number of electronic devices, which I built for the purpose of the presented experiments and for those which will follow. They include a fast high-voltage (HV) switch to control the repulsion voltage U_{rep} in the detection area of the time-of-flight spectrometer (TOF) in order to detect both electrons and ions simultaneously for each laser pulse. Furthermore I built a driver for solenoid pulse valves. The electronic circuits of both are displayed in Figure A.2. For the grating spectrometer used in the setup for high harmonic generation from surfaces (HHGS) I built a spatially resolved photon-detector utilizing two micro-channel plates (MCP) and a phosphor screen. For the same setup I assembled a stepper motor driver to be used with a National Instruments[™] digital input/output (I/O) card, which in turn could be easily controlled by a self-made LabVIEW software.

A.1.3 Piezoelectric pulsed gas-jet valves

For both gas jets—the one employed in the high harmonic generation in gases (HHGG) and the one in the detection area—piezoelectric valves as illustrated in Figure A.3 were employed. They consist of a metal casing loaded with the appropriate gas through an elastic pipe, an adjustable nozzle and a rubber poppet actuated by a disk-shaped piezoelectric crystal.

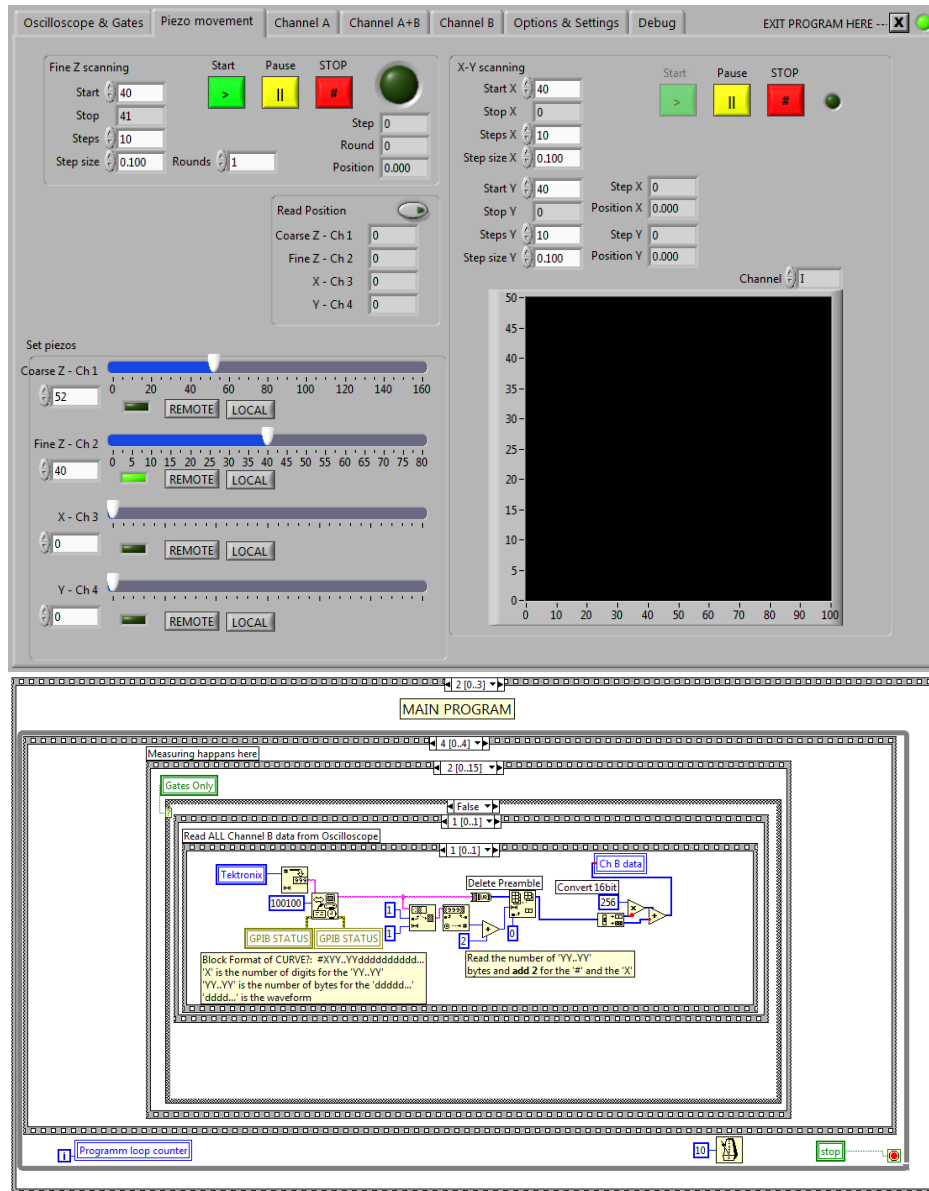


Figure A.1: Control and data acquisition software program

The top panel shows a screen-shot of the user interface displaying the control screen to set the parameters for the scanning of the piezoelectric tilting and translation stages. The bottom panel shows an excerpt of the graphical "code" of the same program.

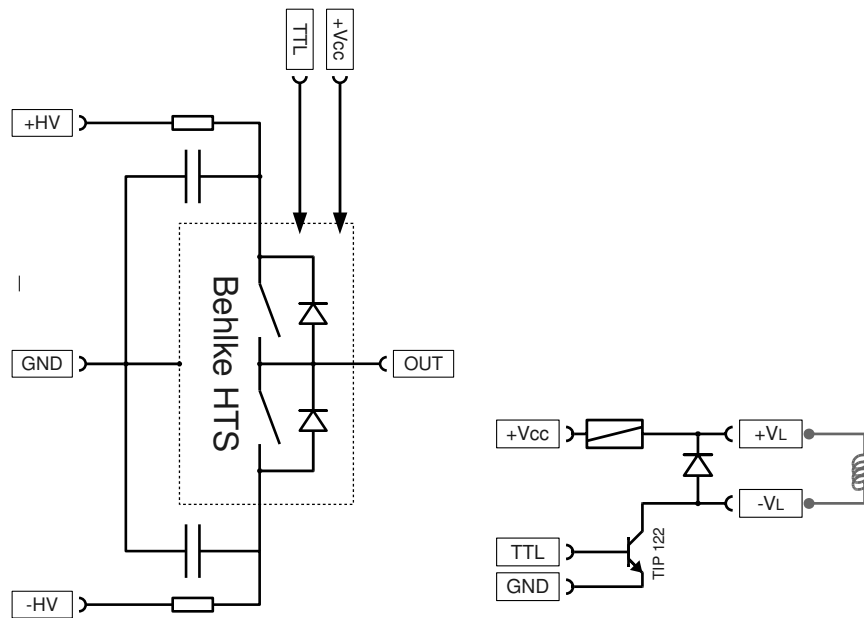


Figure A.2: Schematics of the electronic circuits for the fast high-voltage switch (left) and the solenoid valve driver (right)

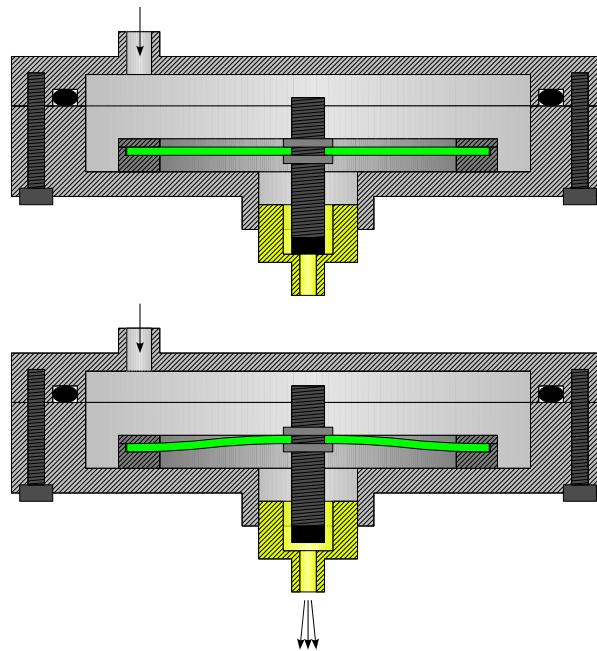


Figure A.3: Schematic of a piezoelectric pulsed gas-jet valve (not to scale)

The panels show a schematic cross-section along the axis of the circular valve. The steel case of the jet (light gray) is loaded with the appropriate gas through the opening at the top. Top panel: The rubber poppet (black) in the center pushes against the opening in the brass nozzle (yellow). It is connected to the piezoelectric crystal (green) through a screw (dark gray). Bottom panel: The crystal deforms if a voltage is applied and consequently moves the poppet away from the opening in the nozzle to let the gas flow.

A.2 Acknowledgments

I would like to gratefully mention Emmanouil Skantzakis, who made the calculations with Mathematica[®] to provide the presented high harmonic generation spectra and the spectral phases of the harmonics as well as the simulated *side band* signals. These calculations have helped to gain an important degree of insight to the consequences of the two quantum paths contributing to the high harmonic generation process.

I would also like to acknowledge the work of Prof. Olivier Faucher, who made the numerical simulations with MATLAB[®] of the second-order intensity volume-autocorrelation and of the time-resolved studies presented in the respective figures. This deepened the understanding of the volume-interaction of the split-mirror setup and successfully helped the data analysis of the time-resolved studies.

A.2.1 Marie Curie Fellowship

This work has been supported by the European Union as part of the Framework Programme 6 (FP6) of the European Commission. It was integrated in the Marie Curie Research Training Network with contract number MRTN-CT-2003-5051389 (XTRA).

A.2.2 Special thanks

There are a number of people, who have been very kind and helpful to me during these previous years of my stay here on Crete. It was not easy for me to establish myself in this country that is quite different from where I grew up and lived before. I want to send my sincerest thanks to all of you, who have made my life here on Crete possible, pleasant, fun and successful! The following people have been there for me more than I could have expected. Thank you very much!

Δημήτρης Χαραλαμπίδης (Prof. Dimítris Charalambídís)

First of all I want to thank my supervisor, who gave me the great

opportunity to come here to the beautiful island of Crete in the first place. He welcomed me here very warmheartedly and integrated me kindly into his research group at the Institute of Electronic Structure and Laser as well as into the international community of researchers at the conferences, which I had the chance to take part in. On top of that, I always learn many things from the fruitful discussions, which he is ready to have any time.

Πάρης Τζάλλας (Páris Tzállas)

Always available for discussion and support he is a priceless source of ideas when it comes to solve a problem. Throughout all the years he has put a continuous effort to supervise me and support this thesis spending thousands of hours together with me in the lab. His guidance and help during my doctorate as well as his specialist improvements and maintenance of our laser system made it possible to achieve these results. Thanks a lot for so many fun and very successful hours in and out of the lab.

Μανόλης Σκαντζάκης (Manólis Skantzákis)

Besides for the most valuable calculations mentioned above, which he contributed to this thesis, I would like to thank my office mate for many lively discussions, for all the help to get along here in this country, and for all the fun and pleasant after-work hours in the city of Heraklion.

Μανόλης Μπενής (Manólis Benís)

Coming from the rather distant research field of semiconductors, I needed a considerable amount of training in the optics laboratory at the beginning. I would like to express my sincerest thanks for being an excellent teacher and also a fine and motivating colleague as long as he was here on Crete during my first years. I wish all the best with the new laboratory at the University of Ioannina.

Γρηγόρης Μαραβέλιος (Grigóris Maravélias)

Many thanks also for the invaluable service of our laser technician for preparing the heart of the laboratory and getting the laser started for

the experiments. Beyond that, he is one of the people that helped me a lot to get along and settle down here in my new home on Crete.

University of Hamburg

I have not forgotten where I came from and I wish to convey my best regards to the Department of Physics and the rest of the University of Hamburg that provided me with the scientific knowledge. I want to especially thank my former supervisor Prof. Ulrich Merkt as well as my colleagues Guido Meier and René Eiselt for the encouraging and helpful guidance. Thanks also to Christian Pels, Marcus Steiner, Mark Ebel and the rest of the group for the pleasant cooperation and the friendly atmosphere at the nanostructure group.

The members of the committee

My most sincere thanks go also to all the members of the examination committee, who were available at such short notice to attend the presentation for the defense of my dissertation.

My family

It is impossible to find the right words to express my thanks to my family for the continuous support and trust throughout all the years. You know it.

A.3 Glossary

1AC	first-order autocorrelation, 30
2AC	second-order autocorrelation, 30, 33
2IVAC	second-order intensity volume-autocorrelation, 11, 33, 47, 51–53, 56, 59, 73, 78, 79
2iVAC	second-order interferometric volume-autocorrelation, 47, 77
AC	autocorrelation, 10, 11, 29, 30, 33, 44, 52
ASC	attosecond streak camera, 25
BBO	beta barium borate, 30, 33
CEP	carrier-envelope phase, 26
CI	conical intersection, 72–74
CPA	chirped pulse amplification, 35
CRAB	frequency-resolved optical gating for complete reconstruction of attosecond bursts, 25
CWE	coherent wake emission, 17, 18, 23
FROG	frequency-resolved optical gating, 25, 33
FROG CRAB	frequency-resolved optical gating for complete reconstruction of attosecond bursts, 26
FTL	Fourier-transform limit, 19, 56, 78
FWHM	full width over half maximum, 13, 35, 40
HHG	high harmonic generation, 12, 14, 18, 19, 26, 36, 77, 80
HHGG	high harmonic generation in gases, 9–11, 14, 16, 18, 21, 51, 79, 84

HHGS	high harmonic generation from surfaces, 9, 14, 18, 80, 84
HiVAC	high-order interferometric volume-autocorrelation, 44
HV	high voltage, 84
IEER	intermediate electronically excited region, 72–74
IR	infrared, 10, 18, 19, 24, 40, 44, 48, 51–53, 56, 60, 63, 67, 69, 70, 77
MCP	micro-channel plate, 48, 84
Nd:YAG	neodymium-doped yttrium aluminium garnet, 35
PANTHER	photoelectron analysis with non-resonant two-photon-ionization for harmonic electric-field reconstruction, 33, 52, 80
PE	photoelectron, 24
PMT	photo-multiplier tube, 38
QIET	quantum-interfering electron trajectories, 66
RABITT	reconstruction of attosecond beating by interference of two-photon transitions, 10, 11, 26, 29, 51, 52, 56, 59, 60, 62, 67, 78, 79
ROM	relativistic oscillating mirror, 17, 18, 80
SPIDER	spectral phase interferometry for direct electric-field reconstruction, 24

TOF	time-of-flight spectrometer, 31, 41, 48, 51, 53, 63, 69, 73, 77, 84
UV	ultraviolet, 9, 74
VAC	volume-autocorrelation, 30, 33
VUV	vacuum ultraviolet, 12, 69–72, 74
XUV	extreme ultraviolet, 1, 10, 11, 16, 24, 29, 31, 40, 41, 51, 52, 56, 60, 63, 67, 69, 70, 79–81
XUV-SPIDER	extreme ultraviolet spectral phase interferometry for direct electric-field reconstruction, 24, 25

A.4 Index

- amplifier, 36
- angular divergence, 15, 39
- angular spread, 15, 39
- atomic phase, 28, 62
- atomic phase shift, 28, 62
- attosecond metrology, 24
- autocorrelation, 24, 29

- bandwidth, 13, 14
- beam diameter, 35, 40

- chirp, 21, 22
- coherent wake emission, 17
- compressor, 36
- conversion efficiency, 16
- cross-correlation, 24
- cut-off, 14, 15

- delay stage, 43, 56
- detection medium, 44
- detection volume, 33
- divergence, 15, 39
- Doppler effect, 17

- efficiency of conversion, 16
- electron trajectories, 20
- emission time, 15

- first-order autocorrelation, 30
- focus position, 40, 41, 53
- Fourier synthesis, 19
- Fourier-transform limit, 19
- frequency comb, 14

- glass target, 36

- grating spectrometer, 37

- harmonic chirp, 21
- harmonic radiation, 14
- harmonics, 14
- Heisenberg's uncertainty principle, 13
- high harmonic generation, 14, 36
- high harmonic generation from surfaces, 16, 36
- high harmonic generation in gases, 14, 39
- high-order autocorrelation, 44
- hysteresis, 47

- inter-harmonic chirp, 21, 22
- interferometric autocorrelation, 47

- laser beam diameter, 35
- laser oscillator, 35
- laser system, 35
- lens position, 40, 41

- minimum pulse duration, 14, 19, 71
- multi-pass amplifier, 36

- odd harmonics, 14
- optical gating, 26
- oscillating mirror model, 17
- oscillator, 35

- parabolic mirror, 36
- phase difference, 26, 60
- phase-locking, 19, 21, 22
- phase-matching, 16, 20, 22

phosphor screen, 37
photo-multiplier tube, 38
photoelectrons, 25
piezoelectric actuator, 43
plasma frequency, 18
plateau, 14, 15
ponderomotive energy, 20
pre-pulse, 38
pulse duration, 9, 13–15, 35, 47, 54,
59, 73, 75, 77

quantum interference, 28
quantum paths, 28

recollision time, 15
regenerative amplifier, 35
relativistic limit, 18, 36
relativistic oscillating mirror, 17
repulsion voltage, 47
resolution, 44
return time, 15

saturation intensity, 16
second-order autocorrelation, 30
side band, 26
silicon wafer, 40
spectrogram, 24
split mirror, 33
stretcher, 35

target, 36
temporal resolution, 44
three-step model, 15
total angular spread, 15, 39
translation stage, 43

tunneling time, 15
uncertainty principle, 13
volume autocorrelation, 31
wave-front splitter, 33
XUV beam diameter, 40

A.5 Bibliography

- Agostini, Pierre, and Louis F. DiMauro. “The physics of attosecond light pulses.” *Reports on Progress in Physics* **67**, 6: (2004) 813–855. [dx.doi.org/10.1088/0034-4885/67/6/R01](https://doi.org/10.1088/0034-4885/67/6/R01).
- Antoine, Philippe, Anne L’Huillier, and Maciej Lewenstein. “Attosecond Pulse Trains Using High-Order Harmonics.” *Physical Review Letters* **77**, 7: (1996) 1234–1237. [dx.doi.org/10.1103/PhysRevLett.77.1234](https://doi.org/10.1103/PhysRevLett.77.1234).
- Auguste, Thierry, Pascal Salières, Adam S. Wyatt, Antoine Monmayrant, Ian A. Walmsley, Eric Cormier, Amelle Zaïr, Mirko Holler, Annalisa Gualdini, Florian Schapper, Jens Biegert, Lukas Gallmann, and Ursula Keller. “Theoretical and experimental analysis of quantum path interferences in high-order harmonic generation.” *Physical Review A* **80**, 3: (2009) 033817. [dx.doi.org/10.1103/PhysRevA.80.033817](https://doi.org/10.1103/PhysRevA.80.033817).
- Baeva, Teodora, Sergei N. Gordienko, and Alexander Pukhov. “Theory of high-order harmonic generation in relativistic laser interaction with overdense plasma.” *Physical Review E* **74**, 4: (2006) 113905. [dx.doi.org/10.1103/PhysRevE.74.046404](https://doi.org/10.1103/PhysRevE.74.046404).
- Benis, Emmanouil P., Dimitris Charalambidis, T. N. Kitsopoulos, George D. Tsakiris, and Paris Tzallas. “Two-photon double ionization of rare gases by a superposition of harmonics.” *Physical Review A* **74**, 5: (2006) 051402. [dx.doi.org/10.1103/PhysRevA.74.051402](https://doi.org/10.1103/PhysRevA.74.051402).
- Bolte, Markus, Marcus Steiner, Christian Pels, Miriam Barthelmeß, Jann Eike Kruse, Ulrich Merkt, Guido Meier, Matthias Holz, and Daniela Pfannkuche. “Magnetotransport through magnetic domain patterns in permalloy rectangles.” *Physical Review B* **72**, 22: (2005) 224436. [dx.doi.org/10.1103/PhysRevB.72.224436](https://doi.org/10.1103/PhysRevB.72.224436).
- Burnett, Neal H., H. A. Baldis, M. C. Richardson, and Gary D. Enright. “Harmonic generation in CO₂ laser target interaction.” *Applied Physics Letters* **31**, 3: (1977) 172–174. [dx.doi.org/10.1063/1.89628](https://doi.org/10.1063/1.89628).

- Carman, Robert L., David W. Forslund, and Joseph M. Kindel. “Visible Harmonic Emission as a Way of Measuring Profile Steepening.” *Physical Review Letters* **46**, 1: (1981) 29–32. [dx.doi.org/10.1103/PhysRevLett.46.29](https://doi.org/10.1103/PhysRevLett.46.29).
- Cavalieri, Adrian L., Norbert Müller, Thorsten Uphues, Vladislav S. Yakovlev, Andrius Baltuška, Balint Horvath, Bernhard Schmidt, L. Blümel, Ronald Holzwarth, Stefan Hendel, Markus Drescher, Ulf Kleineberg, Pedro Miguel Echenique, Reinhard Kienberger, Ferenc Krausz, and Ulrich Heinzmann. “Attosecond spectroscopy in condensed matter.” *Nature* **449**, 7165: (2007) 1029–1032. [dx.doi.org/10.1038/nature06229](https://doi.org/10.1038/nature06229).
- Charalambidis, Dimitris, Paris Tzallas, Emmanouil P. Benis, Emmanouil Skantzakis, Grigoris Maravelias, L. A. A. Nikolopoulos, Álvaro Peralta Conde, and George D. Tsakiris. “Exploring intense attosecond pulses.” *New Journal of Physics* **10**, 2: (2008) 025018. [dx.doi.org/10.1088/1367-2630/10/2/025018](https://doi.org/10.1088/1367-2630/10/2/025018).
- Corkum, Paul B. “Plasma Perspective on Strong-Field Multiphoton Ionization.” *Physical Review Letters* **71**, 13: (1993) 1994–1997. [dx.doi.org/10.1103/PhysRevLett.71.1994](https://doi.org/10.1103/PhysRevLett.71.1994).
- Cormier, Eric, Ian A. Walmsley, Ellen M. Kosik, Adam S. Wyatt, Laura Corner, and Louis F. DiMauro. “Self-Referencing, Spectrally, or Spatially Encoded Spectral Interferometry for the Complete Characterization of Attosecond Electromagnetic Pulses.” *Physical Review Letters* **94**, 3: (2005) 033905. [dx.doi.org/10.1103/PhysRevLett.94.033905](https://doi.org/10.1103/PhysRevLett.94.033905).
- Descamps, Dominique, Lena Roos, Christian Delfin, Anne L’Huillier, and Claes-Göran Wahlström. “Two- and three-photon ionization of rare gases using femtosecond harmonic pulses generated in a gas medium.” *Physical Review A* **64**, 3: (2001) 031404(R). [dx.doi.org/10.1103/PhysRevA.64.031404](https://doi.org/10.1103/PhysRevA.64.031404).

- Drescher, Markus, Michael Hentschel, Reinhard Kienberger, Gabriel Tempea, Christian Spielmann, Georg A. Reider, Paul B. Corkum, and Ferenc Krausz. “X-ray Pulses Approaching the Attosecond Frontier.” *Science* **291**, 5510: (2001) 1923–1927. [dx.doi.org/10.1126/science.1058561](https://doi.org/10.1126/science.1058561).
- Drescher, Markus, Michael Hentschel, Reinhard Kienberger, Matthias Uiberacker, Vladislav Yakovlev, Armin Scrinzi, Thomas Westerwalbesloh, Ulf Kleineberg, Ulrich Heinzmann, and Ferenc Krausz. “Time-resolved atomic inner-shell spectroscopy.” *Nature* **419**: (2002) 803–807. [dx.doi.org/10.1038/nature01143](https://doi.org/10.1038/nature01143).
- Dromey, Brendan, Satyabrata Kar, Claudio Bellei, David C. Carroll, Rob J. Clarke, J. S. Green, Stefan Kneip, Keith Markey, Sabrina Roswitha Nagel, P. T. Simpson, Louise Willingale, Paul McKenna, David Neely, Zulfikar Najmudin, Karl Krushelnick, Peter A. Norreys, and Matthew Zepf. “Bright Multi-keV Harmonic Generation from Relativistically Oscillating Plasma Surfaces.” *Physical Review Letters* **99**, 8: (2007) 085001. [dx.doi.org/10.1103/PhysRevLett.99.085001](https://doi.org/10.1103/PhysRevLett.99.085001).
- Dudovich, Nirit, Olga Smirnova, Jérôme Levesque, Yann Mairesse, Misha Yu Ivanov, David M. Villeneuve, and Paul B. Corkum. “Measuring and controlling the birth of attosecond XUV pulses.” *Nature Physics* **2**, 11: (2006) 781–786. [dx.doi.org/10.1038/nphys434](https://doi.org/10.1038/nphys434).
- Farkas, Gyula, and Csaba Tóth. “Proposal for attosecond light pulse generation using laser induced multiple-harmonic conversion processes in rare gases.” *Physics Letters A* **168**, 5–6: (1992) 447–450. [dx.doi.org/10.1016/0375-9601\(92\)90534-S](https://doi.org/10.1016/0375-9601(92)90534-S).
- Farmanara, Parviz, Oliver Steinkellner, Manfred T. Wick, Michael Wittmann, Georg Korn, Volker Stert, and Wolfgang Radloff. “Ultrafast internal conversion and photodissociation of molecules excited by femtosecond 155 nm laser pulses.” *The Journal of Chemical Physics* **111**, 14: (1999) 6264–6270. [dx.doi.org/10.1063/1.479932](https://doi.org/10.1063/1.479932).

- Faucher, Olivier, Paris Tzallas, Emmanouil P. Benis, Jann Eike Kruse, Álvaro Peralta Conde, Costas Kalpouzos, and Dimitris Charalambidis. “Four-dimensional investigation of the 2nd order volume autocorrelation technique.” *Applied Physics B: Lasers and Optics* **97**, 2: (2009) 505–510. [dx.doi.org/10.1007/s00340-009-3559-z](https://doi.org/10.1007/s00340-009-3559-z).
- Ferray, M., Anne L’Huillier, X. F. Li, Louis-André Lompré, Gérard Mainfray, and Claude Manus. “Multiple-harmonic conversion of 1064 nm radiation in rare gases.” *Journal of Physics B* **21**, 3: (1988) L31–L35. [dx.doi.org/10.1088/0953-4075/21/3/001](https://doi.org/10.1088/0953-4075/21/3/001).
- Foo, P. D., and K. K. Innes. “New experimental tests of existing interpretations of electronic transitions of ethylene.” *The Journal of Chemical Physics* **60**, 11: (1974) 4582–4589. [dx.doi.org/10.1063/1.1680942](https://doi.org/10.1063/1.1680942).
- Gaarde, Mette B., and Kenneth J. Schafer. “Space-Time Considerations in the Phase Locking of High Harmonics.” *Physical Review Letters* **89**, 21: (2002) 213901. [dx.doi.org/10.1103/PhysRevLett.89.213901](https://doi.org/10.1103/PhysRevLett.89.213901).
- Gordienko, Sergei N., Alexander Pukhov, Oleg Shorokhov, and Teodora Baeva. “Relativistic Doppler Effect: Universal Spectra and Zeptosecond Pulses.” *Physical Review Letters* **93**, 11: (2004) 115002. [dx.doi.org/10.1103/PhysRevLett.93.115002](https://doi.org/10.1103/PhysRevLett.93.115002).
- Goulielmakis, Eleftherios, Matthias Uiberacker, Reinhard Kienberger, Andrius Baltuška, Vladislav Yakovlev, Armin Scrinzi, Thomas Westerwalbesloh, Ulf Kleineberg, Ulrich Heinzmann, Markus Drescher, and Ferenc Krausz. “Direct Measurement of Light Waves.” *Science* **305**, 5688: (2004) 1267–1269. [dx.doi.org/10.1126/science.1100866](https://doi.org/10.1126/science.1100866).
- Hänsch, Theodor W. “A proposed sub-femtosecond pulse synthesizer using separate phase-locked laser oscillators.” *Optics Communications* **80**, 1: (1990) 71–75. [dx.doi.org/10.1016/0030-4018\(90\)90509-R](https://doi.org/10.1016/0030-4018(90)90509-R).
- Henke, Burt L., Eric M. Gullikson, and Jeffrey C. Davis. “X-ray interactions: photoabsorption, scattering, transmission, and reflection at E=50–30000

- eV, $Z=1-9$." *Atomic Data and Nuclear Data Tables* **54**, 2: (1993) 181–342. [dx.doi.org/10.1006/adnd.1993.1013](https://doi.org/10.1006/adnd.1993.1013).
- Hentschel, Michael, Reinhard Kienberger, Christian Spielmann, Georg A. Reider, Nenad Milosevic, Thomas Brabec, Paul B. Corkum, Ulrich Heinzmann, Markus Drescher, and Ferenc Krausz. "Attosecond metrology." *Nature* **414**: (2001) 509–513. [dx.doi.org/10.1038/35107000](https://doi.org/10.1038/35107000).
- Hergott, Jean-François, Milutin Kovačev, Hamed Merdji, C. Hubert, Yann Mairesse, E. Jean, Pierre Breger, Pierre Agostini, Bertrand Carré, and Pascal Salières. "Extreme-ultraviolet high-order harmonic pulses in the microjoule range." *Physical Review A* **66**, 2: (2002) 021801. [dx.doi.org/10.1103/PhysRevA.66.021801](https://doi.org/10.1103/PhysRevA.66.021801).
- Holland, Steffen, Yongsheng Gui, Jann Eike Kruse, Detlef Heitmann, Can-Ming Hu, Yifang Chen, Zheng Cui, and G. Pan. "Hybrid devices with high-density nanometallic and nanomagnet dots embedded in the semiconductor." *Applied Physics Letters* **89**, 5: 052106. [dx.doi.org/10.1063/1.2245295](https://doi.org/10.1063/1.2245295).
- Hunter, W. R. "On the optical constants of metals at wavelengths shorter than their critical wavelengths." *Journal de Physique* **25**, 1–2: (1964) 154–160. [dx.doi.org/10.1051/jphys:01964002501-2015400](https://doi.org/10.1051/jphys:01964002501-2015400).
- Iaconis, Chris, and Ian A. Walmsley. "Spectral phase interferometry for direct electric-field reconstruction of ultrashort optical pulses." *Optics Letters* **23**, 10: (1998) 792–794. [dx.doi.org/10.1364/OL.23.000792](https://doi.org/10.1364/OL.23.000792).
- Itatani, Jiro, Fabien Quéré, Gennady L. Yudin, Misha Yu Ivanov, Ferenc Krausz, and Paul B. Corkum. "Attosecond Streak Camera." *Physical Review Letters* **88**, 17: (2002) 173903. [dx.doi.org/10.1103/PhysRevLett.88.173903](https://doi.org/10.1103/PhysRevLett.88.173903).
- Kazamias, Sophie, and Philippe Balcou. "Intrinsic chirp of attosecond pulses: Single-atom model versus experiment." *Physical Review A* **69**, 6: (2004) 063416. [dx.doi.org/10.1103/PhysRevA.69.063416](https://doi.org/10.1103/PhysRevA.69.063416).

- Kienberger, Reinhard, Eleftherios Goulielmakis, Matthias Uiberacker, Andrius Baltuška, Vladislav Yakovlev, Ferdinand Bammer, Armin Scrinzi, Thomas Westerwalbesloh, Ulf Kleineberg, Ulrich Heinzmann, Markus Drescher, and Ferenc Krausz. “Atomic transient recorder.” *Nature* **427**, 6977: (2004) 817–821. [dx.doi.org/10.1038/nature02277](https://doi.org/10.1038/nature02277).
- Kiryama, Hiromitsu, Norihiro Inoue, Yutaka Akahane, and Koichi Yamakawa. “Prepulse-free, multi-terawatt, sub-30-fs laser system.” *Opt. Express* **14**, 1: (2006) 438–445. [dx.doi.org/10.1364/OPEX.14.000438](https://doi.org/10.1364/OPEX.14.000438).
- Kosma, Kyriaki, Sergei A. Trushin, Werner Fuß, and Wolfram E. Schmid. “Ultrafast Dynamics and Coherent Oscillations in Ethylene and Ethylene-D₄ Excited at 162 nm.” *The Journal of Physical Chemistry A* **112**, 33: (2008) 7514–7529. [dx.doi.org/10.1021/jp803548c](https://doi.org/10.1021/jp803548c).
- Koyama, R. Y., N. V. Smith, and W. E. Spicer. “Optical Properties of Indium.” *Physical Review B* **8**, 6: (1973) 2426–2432. [dx.doi.org/10.1103/PhysRevB.8.2426](https://doi.org/10.1103/PhysRevB.8.2426).
- Kruse, Jann Eike, Paris Tzallas, Emmanouil Skantzakis, and Dimitris Charalambidis. “Persistent quantum interfering electron trajectories.” *Physical Review A* **82**, 3: (2010a) 033438. [dx.doi.org/10.1103/PhysRevA.82.033438](https://doi.org/10.1103/PhysRevA.82.033438).
- Kruse, Jann Eike, Paris Tzallas, Emmanouil Skantzakis, Costas Kalpouzos, George D. Tsakiris, and Dimitris Charalambidis. “Inconsistencies between two attosecond pulse metrology methods: A comparative study.” *Physical Review A* **82**, 2: (2010b) 021402. [dx.doi.org/10.1103/PhysRevA.82.021402](https://doi.org/10.1103/PhysRevA.82.021402).
- Kulander, Kenneth C., Kenneth J. Schafer, and Jeffrey L. Krause. “Dynamics of Short-Pulse Excitation, Ionization and Harmonic Conversion.” In *NATO ASIB Proceedings 316: 3rd workshop on Super-Intense Laser-Atom Physics*, edited by B. Piraux, A. L’Huillier, and K. Rzazewski. 1993, 95. www.osti.gov/bridge/product.biblio.jsp?osti_id=10169672.

- Lemonnier, J. C., G. Jezequel, and J. Thomas. “Optical properties in the far uv and electronic structure of indium films.” *Journal of Physics C* **8**, 17: (1975) 2812–2818. [dx.doi.org/10.1088/0022-3719/8/17/021](https://doi.org/10.1088/0022-3719/8/17/021).
- Lewenstein, Maciej, Philippe Balcou, Misha Yu Ivanov, Anne L’Huillier, and Paul B. Corkum. “Theory of high-order harmonic generation by low-frequency laser fields.” *Physical Review A* **49**, 3: (1994) 2117–2132. [dx.doi.org/10.1103/PhysRevA.49.2117](https://doi.org/10.1103/PhysRevA.49.2117).
- Lin, Jim J., Dennis W. Hwang, Yuan T. Lee, and Xueming Yang. “Photodissociation of O₂ at 157 nm: Experimental observation of anisotropy mixing in the O₂+hν → O(³P)+O(³P) channel.” *The Journal of Chemical Physics* **109**, 5: (1998) 1758–1762. [dx.doi.org/10.1063/1.476751](https://doi.org/10.1063/1.476751).
- López-Martens, Rodrigo, Katalin Varjú, Per Johnsson, Johan Mauritsson, Yann Mairesse, Pascal Salières, Mette B. Gaarde, Kenneth J. Schafer, Anders Persson, Sune Svanberg, Claes-Göran Wahlström, and Anne L’Huillier. “Amplitude and Phase Control of Attosecond Light Pulses.” *Physical Review Letters* **94**, 3: (2005) 033001. [dx.doi.org/10.1103/PhysRevLett.94.033001](https://doi.org/10.1103/PhysRevLett.94.033001).
- Mairesse, Y., and F. Quéré. “Frequency-resolved optical gating for complete reconstruction of attosecond bursts.” *Physical Review A* **71**, 1: (2005) 011401. [dx.doi.org/10.1103/PhysRevA.71.011401](https://doi.org/10.1103/PhysRevA.71.011401).
- Mairesse, Yann, O. Gobert, Pierre Breger, Hamed Merdji, P. Meynadier, P. Monchicourt, M. Perdrix, Pascal Salières, and Bertrand Carré. “High Harmonic XUV Spectral Phase Interferometry for Direct Electric-Field Reconstruction.” *Physical Review Letters* **94**, 17: (2005) 173903. [dx.doi.org/10.1103/PhysRevLett.94.173903](https://doi.org/10.1103/PhysRevLett.94.173903).
- McPherson, Armon, G. Gibson, H. Jara, Ulrich Johann, Ting Shah Luk, Iain A. McIntyre, Keith Boyer, and Charles K. Rhodes. “Studies of multiphoton production of vacuum-ultraviolet radiation in the rare gases.” *Journal of the Optical Society of America B* **4**, 4: (1987) 595–601. [dx.doi.org/10.1364/JOSAB.4.000595](https://doi.org/10.1364/JOSAB.4.000595).

- Mestdagh, Jean-Michel, Jean-Paul Visticot, Mohammed Elhanine, and Benoît Soep. “Prereactive evolution of monoalkenes excited in the 6 eV region.” *The Journal of Chemical Physics* **113**, 1: (2000) 237–248. [dx.doi.org/10.1063/1.481790](https://doi.org/10.1063/1.481790).
- Moore, Charlotte Emma. *Selected Tables of Atomic Spectra*, volume 3, section 7 of *National Standard Reference Data Series*. National Bureau of Standards, 1976, 2 edition. www.nist.gov/data/nsrds/NSRDS-NBS3-7.pdf.
- Muller, Harm Geert. “Reconstruction of attosecond harmonic beating by interference of two-photon transitions.” *Applied Physics B: Lasers and Optics* **74**: (2002) S17–S21. [dx.doi.org/10.1007/s00340-002-0894-8](https://doi.org/10.1007/s00340-002-0894-8).
- Nabekawa, Yasuo, Toshihiko Shimizu, Tomoya Okino, Kentaro Furusawa, Hirokazu Hasegawa, Kaoru Yamanouchi, and Katsumi Midorikawa. “Conclusive Evidence of an Attosecond Pulse Train Observed with the Mode-Resolved Autocorrelation Technique.” *Physical Review Letters* **96**, 8: (2006) 083901. [dx.doi.org/10.1103/PhysRevLett.96.083901](https://doi.org/10.1103/PhysRevLett.96.083901).
- Nikolopoulos, L. A. A., Emmanouil P. Benis, Paris Tzallas, Dimitris Charalambidis, Klaus Witte, and George D. Tsakiris. “Second Order Autocorrelation of an XUV Attosecond Pulse Train.” *Physical Review Letters* **94**, 11: (2005) 113905. [dx.doi.org/10.1103/PhysRevLett.94.113905](https://doi.org/10.1103/PhysRevLett.94.113905).
- Nomura, Yutaka, Rainer Hörlein, Paris Tzallas, Brendan Dromey, Sergey G. Rykovanov, Zsuzsanna Major, Jens Osterhoff, Stefan Karsch, Laszlo Veisz, Matthew Zepf, Dimitris Charalambidis, Ferenc Krausz, and George D. Tsakiris. “Attosecond phase locking of harmonics emitted from laser-produced plasmas.” *Nature Physics* **5**, 2: (2009) 124–128. [dx.doi.org/10.1038/nphys1155](https://doi.org/10.1038/nphys1155).
- Papadogiannis, Nektarios A., Bernd Witzel, Costas Kalpouzos, and Dimitris Charalambidis. “Observation of Attosecond Light Localization in Higher Order Harmonic Generation.” *Physical Review Letters* **83**, 21: (1999) 4289–4292. [dx.doi.org/10.1103/PhysRevLett.83.4289](https://doi.org/10.1103/PhysRevLett.83.4289).

- Paul, Pierre-Marie, Elena-Simona Toma, Pierre Breger, Geneviève Mullet, Frédérique Augé-Rochereau, Philippe Balcou, Harm Geert Muller, and Pierre Agostini. “Observation of a Train of Attosecond Pulses from High Harmonic Generation.” *Science* **292**, 5522: (2001) 1689–1692. [dx.doi.org/10.1126/science.1059413](https://doi.org/10.1126/science.1059413).
- Peralta Conde, Álvaro, Jann Eike Kruse, Olivier Faucher, Paris Tzallas, Emmanouil P. Benis, and Dimitris Charalambidis. “Realization of time-resolved two-vacuum-ultraviolet-photon ionization.” *Physical Review A* **79**, 6: (2009a) 061405. [dx.doi.org/10.1103/PhysRevA.79.061405](https://doi.org/10.1103/PhysRevA.79.061405).
- Peralta Conde, Álvaro, Paris Tzallas, and Dimitris Charalambidis. “On the population dynamics induced by an attosecond train interacting coherently with an atomic system within the electric dipole approximation.” *The European Physical Journal D* **51**, 2: (2009b) 289–294. [dx.doi.org/10.1140/epjd/e2009-00018-8](https://doi.org/10.1140/epjd/e2009-00018-8).
- Pirri, Angela, Chiara Corsi, and Marco Bellini. “Enhancing the yield of high-order harmonics with an array of gas jets.” *Physical Review A* **78**, 1: (2008) 011801. [dx.doi.org/10.1103/PhysRevA.78.011801](https://doi.org/10.1103/PhysRevA.78.011801).
- Plaja, Luis, Luis Roso, Kazimierz Rzazewski, and Maciej Lewenstein. “Generation of attosecond pulse trains during the reflection of a very intense laser on a solid surface.” *Journal of the Optical Society of America B* **15**, 7: (1998) 1904–1911. [dx.doi.org/10.1364/JOSAB.15.001904](https://doi.org/10.1364/JOSAB.15.001904).
- Protopapas, M, Christoph H. Keitel, and Peter L. Knight. “Atomic physics with super-high intensity lasers.” *Reports on Progress in Physics* **60**, 4: (1997) 389. [dx.doi.org/10.1088/0034-4885/60/4/001](https://doi.org/10.1088/0034-4885/60/4/001).
- Quéré, Fabien, Jiro Itatani, Gennady L. Yudin, and Paul B. Corkum. “Attosecond Spectral Shearing Interferometry.” *Physical Review Letters* **90**, 7: (2003) 073902. [dx.doi.org/10.1103/PhysRevLett.90.073902](https://doi.org/10.1103/PhysRevLett.90.073902).
- Quéré, Fabien, Cédric Thaury, Pascal Monot, Sandrine Dobosz, Philippe Martin, Jean-Paul Geindre, and Patrick Audebert. “Coherent Wake Emission of High-Order Harmonics from Overdense Plasmas.” *Physical Review*

- Letters* **96**, 12: (2006) 125004. [dx.doi.org/10.1103/PhysRevLett.96.125004](https://doi.org/10.1103/PhysRevLett.96.125004).
- Robotis, Dimitris. Bachelor's Thesis, *University of Crete, Department of Physics*, Heraklion – Greece, 2009.
- Roso, Luis, Luis Plaja, Kazimierz Rzazewski, and Dietrich von der Linde. “Beyond the moving mirror model: Attosecond pulses from a relativistically moving plasma.” *Laser and Particle Beams* **18**, 03: (2000) 467–475. [dx.doi.org/10.1017/S0263034600183168](https://doi.org/10.1017/S0263034600183168).
- Rykovanov, Sergey G., Michael Geissler, Jürgen Meyer ter Vehn, and George D. Tsakiris. “Intense single attosecond pulses from surface harmonics using the polarization gating technique¹⁰.” *New Journal of Physics* **10**: (2008) 025025. [dx.doi.org/10.1007/s00340-009-3559-z](https://doi.org/10.1007/s00340-009-3559-z).
- Salières, Pascal, Bertrand Carré, Laurent Le Déroff, Felix Grasbon, Gerhard G. Paulus, Herbert Walther, Richard Kopold, Wilhelm Becker, Dejan B. Milošević, Anna Sanpera, and Maciej Lewenstein. “Feynman's Path-Integral Approach for Intense-Laser-Atom Interactions.” *Science* **292**, 5518: (2001) 902–905. [dx.doi.org/10.1126/science.108836](https://doi.org/10.1126/science.108836).
- Schafer, Kenneth J., Baorui Yang, Louis F. DiMauro, and Kenneth C. Kulander. “Above threshold ionization beyond the high harmonic cutoff.” *Physical Review Letters* **70**, 11: (1993) 1599–1602. [dx.doi.org/10.1103/PhysRevLett.70.1599](https://doi.org/10.1103/PhysRevLett.70.1599).
- Skantzakis, Emmanouil, Paris Tzallas, Jann Eike Kruse, Costas Kalpouzos, and Dimitris Charalambidis. “Coherent continuum extreme ultraviolet radiation in the sub-100-nJ range generated by a high-power many-cycle laser field.” *Optics Letters* **34**, 11: (2009) 1732–1734. [dx.doi.org/10.1364/OL.34.001732](https://doi.org/10.1364/OL.34.001732).
- Skantzakis, Emmanouil, Paris Tzallas, Jann Eike Kruse, Costas Kalpouzos, Olivier Faucher, George D. Tsakiris, and Dimitris Charalambidis. “Tracking Autoionizing-Wave-Packet Dynamics at the 1-fs Temporal Scale.”

Physical Review Letters **105**, 4: (2010) 043902. [dx.doi.org/10.1103/PhysRevLett.105.043902](https://doi.org/10.1103/PhysRevLett.105.043902).

Stert, Volker, Helmut Lippert, Hans-Hermann Ritze, and Wolfgang Radloff. “Femtosecond time-resolved dynamics of the electronically excited ethylene molecule.” *Chemical Physics Letters* **388**, 1-3: (2004) 144–149. [dx.doi.org/10.1016/j.cplett.2004.02.077](https://doi.org/10.1016/j.cplett.2004.02.077).

Takahashi, Eiji J., Hirokazu Hasegawa, Yasuo Nabekawa, and Katsumi Midorikawa. “High-throughput, high-damage-threshold broadband beam splitter for high-order harmonics in the extreme-ultraviolet region.” *Optics Letters* **292**, 5: (2004) 507–509. [dx.doi.org/10.1364/OL.29.000507](https://doi.org/10.1364/OL.29.000507).

Takahashi, Eiji J., Yasuo Nabekawa, Tatsuya Otsuka, Minoru Obara, and Katsumi Midorikawa. “Generation of highly coherent submicrojoule soft x rays by high-order harmonics.” *Physical Review A* **66**, 2: (2002) 021802. [dx.doi.org/10.1103/PhysRevA.66.021802](https://doi.org/10.1103/PhysRevA.66.021802).

Tarasevitch, Alexander, Konstantin Lobov, Clemens Wünsche, and Dietrich von der Linde. “Transition to the Relativistic Regime in High Order Harmonic Generation.” *Physical Review Letters* **98**, 10: (2007) 103902. [dx.doi.org/10.1103/PhysRevLett.98.103902](https://doi.org/10.1103/PhysRevLett.98.103902).

Tarasevitch, Alexander, Andreas Orisch, Dietrich von der Linde, Philippe Balcou, Gilles Rey, Jean-Paul Chambaret, Ulrich Teubner, Diethard Klöpfel, and Wolfgang Theobald. “Generation of high-order spatially coherent harmonics from solid targets by femtosecond laser pulses.” *Physical Review A* **62**, 2: (2000) 023816. [dx.doi.org/10.1103/PhysRevA.62.023816](https://doi.org/10.1103/PhysRevA.62.023816).

Teubner, Ulrich, Klaus Eidmann, Ulrich Wagner, Ulrich Andiel, Francesca Pisani, George D. Tsakiris, Klaus Witte, Jürgen Meyer ter Vehn, Theodor Schlegel, and Eckhart Förster. “Harmonic Emission from the Rear Side of Thin Overdense Foils Irradiated with Intense Ultrashort Laser Pulses.” *Physical Review Letters* **92**, 18: (2004) 185001. [dx.doi.org/10.1103/PhysRevLett.92.185001](https://doi.org/10.1103/PhysRevLett.92.185001).

Trebino, Rick, and Daniel J. Kane. “Using phase retrieval to measure the intensity and phase of ultrashort pulses: frequency-resolved optical gating.” *Journal of the Optical Society of America A* **10**, 5: (1993) 1101–1111. [dx.doi.org/10.1364/JOSAA.10.001101](https://doi.org/10.1364/JOSAA.10.001101).

Tzallas, Paris, Dimitris Charalambidis, Nektarios A. Papadogiannis, Klaus Witte, and George D. Tsakiris. “Direct observation of attosecond light bunching.” *Nature* **426**: (2003) 267–271. [dx.doi.org/10.1038/nature02091](https://doi.org/10.1038/nature02091).

———. “Second-order autocorrelation measurements of attosecond XUV pulse trains.” *Journal of Modern Optics* **52**, 2: (2005) 321–338. [dx.doi.org/10.1080/09500340412331301533](https://doi.org/10.1080/09500340412331301533).

Tzallas, Paris, Emmanouil Skantzakis, Jann Eike Kruse, and Dimitris Charalambidis. *Progress in Ultrafast Intense Laser Science*, Luxemburg, Berlin: Springer, 2011, volume 100 of *Springer Series in Chemical Physics*, chapter 5: “On the generation of intense isolated attosecond pulses by many-cycle laser fields.” www.springer.com/978-3-642-18326-3.

Uiberacker, Matthias, Thorsten Uphues, Martin Schultze, Aart J. Verhoef, Vladislav S. Yakovlev, Matthias F. Kling, Jens Rauschenberger, Nicolai M. Kabachnik, Hartmut Schröder, Matthias Lezius, Karl-Ludwig Kompa, Harm Geert Muller, Marc J. J. Vrakking, Stefan Hendel, Ulf Kleineberg, Ulrich Heinzmann, Markus Drescher, and Ferenc Krausz. “Attosecond real-time observation of electron tunnelling in atoms.” *Nature* **446**, 7136: (2007) 627–632. [dx.doi.org/10.1038/nature05648](https://doi.org/10.1038/nature05648).

Varjú, Katalin, Yann Mairesse, Bertrand Carré, Mette B. Gaarde, Per Johnsson, Sophie Kazamias, Rodrigo López-Martens, Johan Mauritsson, Kenneth J. Schafer, Philippe Balcou, Anne L’Huillier, and Pascal Salières. “Frequency chirp of harmonic and attosecond pulses.” *Journal of Modern Optics* **52**, 2: (2005) 379–394. [dx.doi.org/10.1080/09500340412331301542](https://doi.org/10.1080/09500340412331301542).

Zaïr, Amelle, Mirko Holler, Annalisa Guandalini, Florian Schapper, Jens Biegert, Lukas Gallmann, Ursula Keller, Adam S. Wyatt, Antoine Monmayrant, Ian A. Walmsley, Eric Cormier, Thierry Auguste, Jean-Pascal Caumes, and Pascal Salières. “Quantum Path Interferences in High-Order Harmonic Generation.” *Physical Review Letters* **100**, 14: (2008) 143902. [dx.doi.org/10.1103/PhysRevLett.100.143902](https://doi.org/10.1103/PhysRevLett.100.143902).

List of publications to which I actively contributed

1. Bolte, Steiner, Pels, Barthelmeß, Kruse, Merkt, Meier, Holz, and Pfannkuche (2005)
2. Holland, Gui, Kruse, Heitmann, Hu, Chen, Cui, and Pan (2006)
3. Peralta Conde, Kruse, Faucher, Tzallas, Benis, and Charalambidis (2009a)
4. Faucher, Tzallas, Benis, Kruse, Peralta Conde, Kalpouzos, and Charalambidis (2009)
5. Skantzakis, Tzallas, Kruse, Kalpouzos, and Charalambidis (2009)
6. Skantzakis, Tzallas, Kruse, Kalpouzos, Faucher, Tsakiris, and Charalambidis (2010)
7. Tzallas, Skantzakis, Kruse, and Charalambidis (2011)
8. Kruse, Tzallas, Skantzakis, Kalpouzos, Tsakiris, and Charalambidis (2010b)
9. Kruse, Tzallas, Skantzakis, and Charalambidis (2010a)